Sulfur Poisoning and Regeneration of Aftertreatment Oxidation Catalysts

---

A Dissertation
Presented to
The Faculty of the School of Engineering and Applied Science
University of Virginia

In Partial Fulfillment
Of The Requirements for the Degree

Doctor of Philosophy

By

Natalia Diaz Montenegro

May 2024

APPROVAL SHEET

This
Dissertation
is submitted in partial fulfillment of the requirements
for the degree of
Doctor of Philosophy

Author: Natalia Diaz Montenegro

This Dissertation has been read and approved by the examing committee:

Advisor: William S. Epling

Advisor:

Committee Member: Christopher Paolucci

Committee Member: Robert J. Davis

Committee Member: Jason Bates

Committee Member: Sen Zhang

Committee Member:

Committee Member:

Accepted for the School of Engineering and Applied Science:

Jennifer L. West, School of Engineering and Applied Science

May 2024

Abstract

Catalytic converters are the current technology for emission control from internal combustion engines. Depending on the operating mode of the engine and the composition of the pollutants present in the exhaust gas, the aftertreatment system components may vary. Nevertheless, an oxidation catalyst is always present, or a component of the catalyst has oxidation function, regardless of the engine type. It is responsible for mitigating emissions of unburned hydrocarbons, CO, and other pollutants. However, small amounts of sulfur originating from both fuel and lubricating oils are the cause of chemical degradation of oxidation catalysts due to the strong chemisorption of sulfur on the catalyst surface. Exposure to sulfur forms numerous sulfur species that inhibit the active material in these catalysts from carrying out oxidation reactions. In this work, we assessed the effects of sulfur poisoning of new formulations of oxidation catalysts, enhanced regeneration strategies to recover catalytic activity, and further investigated the particle size effects on sulfur speciation after aftertreatment catalyst aging protocols.

We assessed the effects of sulfur poisoning and regeneration on a new methane oxidation catalyst formulation that integrates a spinel oxide layer as the oxygen storage material for natural gas exhaust applications. We studied the methane oxidation performance under periodic conditions and the oxygen storage capacity of a bilayer Pt-Pd/Al_2O_3 + $Mn_{0.5}Fe_{2.5}O_4$ catalyst before and after SO_2 exposure, and after simulated regeneration conditions. Prior to SO_2 exposure, under both simple feed and more complex simulated exhaust conditions, CH_4 conversion at low temperatures was improved under periodic conditions compared to steady-state conditions. Methane

oxidation activity and oxygen storage capacity of the spinel-based oxygen storage material were affected after SO_2 exposure. Common literature regeneration protocols were applied, and while all regeneration protocols did improve CH_4 oxidation activity, the utilization of regeneration methods under periodic conditions induced greater sulfur species desorption from the catalyst surface, ultimately resulting in a higher recovery of oxidation activity. Key parameters of this enhanced regeneration protocol under periodic conditions – temperature, feed composition, modulation amplitude and frequency – could be optimized to improve regenerability after sulfur poisoning.

The development of sulfur-resistant materials presents another avenue to alleviate the effects of sulfur poisoning of oxidation catalysts. The performance of a bimetallic Pd-Cu diesel oxidation catalyst in the presence of competitive adsorbates and its response to sulfur poisoning was studied The addition of Cu to Pd-based diesel oxidation catalysts (DOCs) does offer some resistance to SO_2 poisoning based on the lower amount of SO_2 adsorbed during the SO_2 exposure, compared to the SO_2 adsorbed on the monometallic Pd sample. Plus, after sulfur exposure at 100 °C, the regeneration protocol under reducing conditions can reverse the effects of SO_2 poisoning for both CO oxidation and CO+NO co-oxidation conditions.

As an extension of understanding sulfur poisoning, we investigated the influence of precious metal particle size effects on sulfur speciation after aftertreatment catalyst aging protocols. To avoid particle size heterogeneity, we synthesized uniform Pd nanoparticles with two particle sizes (3.4 nm and 13.1 nm) and deposited them onto supports relevant to aftertreatment applications, Al_2O_3 and CeO_2. The gas composition of aging protocols (hydrothermal vs. thermal) and particle size influence sulfur speciation for both Al_2O_3-supported catalysts. In the case of CeO_2-supported catalysts, particle size does not lead to changes in sulfur speciation. CO pulse injection measurements were used to evaluate the changes in particle size that occurred during aging and show that catalysts with a smaller particle size are more susceptible to sintering compared to catalysts with a larger particle size. Even though aging does affect CO oxidation activity for catalysts with a smaller particle size, they exhibit higher resistance to sulfur poisoning. Conversely, the catalysts with a larger particle size experience the opposite effect.

Acknowledgments

First, I would like to thank the people at the University of Florida that encouraged and helped me pursue a graduate career: my undergraduate mentor Dr. Sindia M. Rivera-Jiménez, my research mentor Dr. Anuj Chauhan, and my friend Dr. Liliana Bello Fernandez.

I would like to express my deepest gratitude to my advisor, Dr. William S. Epling, for your guidance and mentorship for the past 5+ years. I appreciate your expertise, your patience, and your unwavering commitment to my academic and professional growth. Above all, thank you for pushing me outside of my comfort zone to become a better researcher, presenter, and writer. I would also like to give my deepest appreciation to the catalysis graduate students and professors, Dr. Robert J. Davis, Dr. Christopher Paolucci, and Dr. Jason Bates for all the feedback and catalysis lessons shared during our weekly group meetings. I would also like to acknowledge Dr. Wei Li, Dr. Kevin Gu, and the Catalysts and Interfacial Chemistry team at General Motors for providing me with the opportunity to apply and further my research skills. I would like to acknowledge past and current members of the Epling Lab. A special note of gratitude to Dr. Poonam Rani, Dr. Zhuoran Gan, and my undergraduate students CJ Hall and Zexian He for making life more enjoyable in the basement.

Many thanks to my support systems both within and beyond UVA: my therapist Liz Ramirez-Weaver, my fellow cohort members, the UVA ChE Colombian crew, my Lambda Theta Alpha sorority sisters, my running friends in Charlottesville and Detroit, Stevie Wonder, and my insiders friends. I am also extremely grateful for my partner Dr. Ryan Zelinsky “because I came here with a load, and it feels so much lighter since I met you.”

Finally, for the ones I left behind to go on this PhD journey… I would like to thank my family, Francisco Diaz Rozo, Ligia Montenegro Gordillo, and Julian David Diaz Montenegro, for their endless support, love, and guidance. I am also very grateful for all the encouragement from my extended family in the US and in Colombia. Los quiero mucho ♥

"Friends and neighbors will say, What happened to that Esperanza?

Where did she go with all those books and paper? Why did she march so far away?

They will not know I have gone away to come back.

For the ones I left behind. For the ones who cannot out"

– Excerpt from The House on Mango Street by Sandra Cisneros [1].

Table of Contents

List of Figures

List of Tables

1. Introduction

1.1 Background of Emission Control

By the early 1950s, vehicular exhaust had been widely recognized as a source of air pollution and smog formation. Early quantification studies of tailpipe emissions showed that depending on the operating mode, a vehicle could emit between 470 to 17,000 ppm of unburned hydrocarbons (HCs), 8,800 to 20,000 ppm of carbon monoxide (CO) and 20 to 1,000 ppm of nitrogen oxides (NO_x) [2]. As a result of the photochemical reaction of these pollutants with sunlight, the combination of the produced ground-level ozone and fine particulate matter resulted in smog formation [3], [4]. Short-term effects of ozone exposure include asthma, pulmonary inflammation, decreased cardiac function, among others [5]. Because of the effects of poor air quality on human health and the environment, the passage of the Clean Air Act of 1970 required a 90% reduction of vehicular emissions from new automobiles by 1975. The Environmental Protection Agency (EPA) was also established and is the main regulatory agency for fuel and vehicular emission standards for HCs, CO, and NO_x. The development of catalytic aftertreatment systems became the solution to meet these emission standards [6], [7].

The most recent emission standards adopted by the EPA are the Tier 3 Standards starting with 2017 and 2018 model years for light-duty vehicles with a gross vehicle weight rating (GVWR) over 6,000 lbs. Based on the Federal Test Procedure, the EPA established an emission standard for non-methane organic gases and NOx (NMOG+NO_x) of 30 mg/mile by 2025 and a limit of particulate matter (PM) emissions of 3 mg/mile by 2022. Tier 3 Standards also apply to gasoline- and diesel-powered heavy-duty vehicle categories in Class 2b (GVWR range between 8,501-10,000 lbs) and Class 3 (GVWR range between 10,001-14,000 lbs). The EPA mandated NMOG+NO_x standards of 178 mg/mile and 247 mg/mile by 2022 for Class 2b and Class 3 heavy-duty vehicles, respectively. Additionally, a PM emission limit of 8 mg/mile and 10 mg/mile for Class 2b and Class 3 heavy-duty vehicle categories were established. These regulations must be met over a useful life of 150,000 miles or 15 years whichever occurs first. In terms of fuel standards, the EPA also mandated a decrease in the gasoline sulfur content from 30 parts per million (ppm) to 10 ppm due to the detrimental impact of sulfur on the performance of the aftertreatment system [8]. As future emission standards become more stringent, the drive to develop more robust aftertreatment systems has increased.

The impact of the implementation of catalytic aftertreatment systems for vehicular emission control has led to the significant improvement of air quality in the United States. Since the 1980s, the concentrations of CO, NO_x and PM have substantially decreased and are well below regulated air quality standards [9]. Additionally, according to the EPA, the effects of Tier 3 Standards on vehicular emissions are projected to result in a reduction of 260,000 tons of NOx emissions and nearly 3.5 million tons of CO emissions. They also project that by 2030, the reduction in vehicular emissions will avert 660-1,500 premature deaths linked to particulate matter and 110-550 premature deaths associated with exposure to ground-level ozone [8].

1.2 Current Aftertreatment Systems

Catalytic converters are the current technology for emission control from internal combustion engines. The aftertreatment system components vary depending on the operating mode of the engine and are influenced by the composition of pollutants present in the exhaust gas. Typically, these components are designed with a ceramic honeycomb structure made of cordierite ($2MgO-5SiO_2-2Al_2O_3$), onto which the active components and support materials are washcoated [10], [11]. For stoichiometric-burn gasoline and natural gas engines, the main aftertreatment is the three-way catalyst (TWC) that simultaneously converts HC, CO and NO_x emissions into CO_2, H_2O and N_2 [12]–[16]. For lean-burn diesel engines, the aftertreatment system is more complex and requires additional components to meet emission standards. It is composed of the diesel oxidation catalyst (DOC), diesel particulate filter (DPF), and selective catalytic reduction (SCR) and ammonia slip catalysts (ASC) [17], [18]. The structure and chemistry of the TWC and DOC only will be discussed in this introduction.

1.2.1 Three-Way Catalysts

Three-way catalysts (TWCs) are the aftertreatment technology that simultaneously converts HC, CO and NOx emissions in engines that operate at the stoichiometric air-to-fuel ratio (AFR). Despite their high cost and low availability, precious metals (Pt, Pd, Rh) remain the active centers for the conversion of pollutants in aftertreatment systems [19]–[22]. Both Pt and Pd are used to oxidize unburned hydrocarbons and CO (Eq. 1.1 and 1.2), while Rh is utilized for NO_x reduction (Eq. 1.3 and 1.4). To maintain their stability and activity, the combination of these precious metals is deposited onto high surface supports, such as Al_2O_3 [23], with the addition of CeO_2-based oxygen storage materials and thermal stabilizers.

Hydrocarbon and CO oxidation reactions:

$$C_mH_n + O_2 \rightarrow CO_2(CO) + H_2O \tag{1.1}$$

$$CO + {}^{1}\!/_{2}\, O_2 \rightarrow CO_2 \tag{1.2}$$

NO reduction reactions:

$$C_mH_n + NO \rightarrow N_2\,(N_2O, NH_3) + CO_2 + H_2O \tag{1.3}$$

$$CO + NO \rightarrow N_2\,(N_2O, NH_3) + CO_2 \tag{1.4}$$

As shown in Figure 1-1, the TWC performance depends on the AFR and can achieve full conversion of all pollutants at the stoichiometric point ($\lambda = 1$). The term λ is a dimensionless quantity defined as the ratio of the actual AFR to the stoichiometric AFR for complete combustion, by weight. Under fuel rich conditions ($\lambda < 1$), insufficient oxygen in the exhaust causes the incomplete conversion of HC and CO emissions, while NOx emissions can be fully converted. Under fuel lean conditions ($\lambda > 1$), excess oxygen in the exhaust favors complete oxidation of HC and CO emissions, while the conversion of NOx decreases.

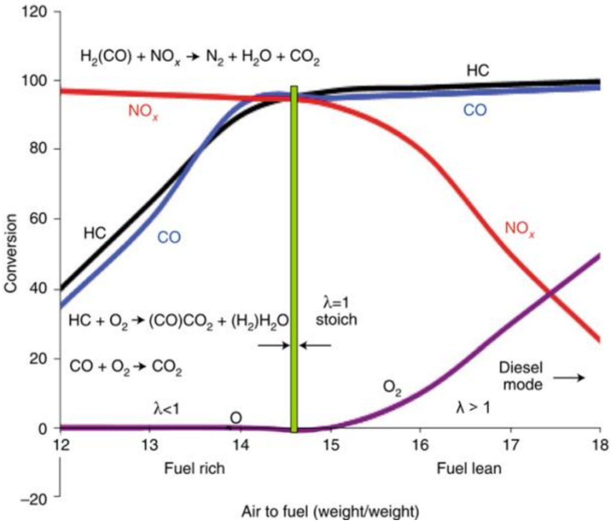

Figure 1-1 Performance of oxidation catalyst as a function of the air-to-fuel ratio [13]

Speed and power variations during the driving cycle cause AFR changes that directly affect TWC performance. To alleviate these effects, CeO_2 as an oxygen storage material was selected as an additive to TWC formulations due to its facile $Ce^{4+} \leftrightarrow Ce^{3+}$

interconversion and minimal structural rearrangement during the redox mechanism (Eq. 1.5) [13], [24]–[28].

$$CeO_2 \leftrightarrow CeO_{2-x} + \frac{x}{2} O_2 \tag{1.5}$$

In oxygen-deficient environments, CeO_2 reduces to CeO_{2-x}, where the released O is used in the reactions described above (Eqs. 1.1-1.4), which also creates oxygen vacancies at the surface. In an oxygen-rich environment, oxygen vacancies are replenished with gas-phase O_2 leading to the re-oxidation of CeO_2 to maintain AFR at stoichiometric conditions. In addition to its role in oxygen storage, the incorporation of CeO_2 to TWC formulations also improves precious metal dispersion [28], promotes water-gas shift and steam reforming reactions [29]–[31], and enhances catalytic activity at the metal-support interface [32], [33]. With its poor thermal stability at high temperatures, small quantities of Zr are added to CeO_2 leads to improve thermal stability and oxygen storage capacity [34]–[37].

Current research trends in TWC development mostly focus on enhancing the efficiency of precious metal usage and mitigating deactivation effects stemming from exposure to high temperature (>1050 °C) [13], [38]–[40]. Since the inception of aftertreatment systems in the 1970s, precious metals (Pt, Pd, Rh) have been used as the active centers for TWC chemistry due to their high performance; however, exposure to high operating temperatures leads to the loss of metal surface area due to agglomeration of nanoparticles, loss of surface area of the support and/or promoters, and the conversion of active materials into inactive forms [41], [42]. Due to the high price and low availability of precious metals, new synthesis routes have emerged to achieve high precious metal utilization while minimizing the deactivation mechanisms caused by exposure to high temperature [43], [44]. Atom trapping and fine-tuning TWC supports are potential techniques to achieve highly dispersed and stable catalysts [45], [46].

1.2.2 Diesel Oxidation Catalysts

As the first unit operation of the diesel aftertreatment system, the diesel oxidation catalyst (DOC) is responsible for the oxidation of unburned HCs, CO, and NO emissions (Eq. 1.1-1.2 and 1.6) [17], [18]. Unlike TWCs, DOCs operate under fuel lean conditions as shown in Figure 1-1 and due to the excess oxygen in the engine exhaust, additional components must be added to the aftertreatment system to fully convert all pollutants to meet emission standards.

NO oxidation:

$$2NO + O_2 \rightarrow 2NO_2 \tag{1.6}$$

Generally, DOC components closely resemble those found in TWCs, except they are predominantly composed of Pt and do not contain Rh. The utilization of Pt in DOC formulations offers notable advantages, including its low surface oxygen coverage and high oxidation activity [47]. However, these catalysts are susceptible to sintering at high temperatures and can easily oxidize SO_2, a common catalyst poison, to undesirable products such as SO_3 and H_2SO_4 [48]–[50]. Introducing small quantities of Pd to Pt-based DOCs can alleviate these drawbacks while also improving their overall cost.

To curb pollutant production and diminish the need for complex aftertreatment systems, improving the diesel combustion process inside the engine is a viable option. Modern low temperature combustion (LTC) engines can emit less NOx and particulate matter emissions compared to conventional engines [51], [52]; however, due to the low operating temperatures, especially during the cold-start period, the DOC fails to fully convert HC and CO emissions, leading to their release into the atmosphere. Therefore, as the current research goal, the "150 °C Challenge" was created by the Department of Energy to drive the creation of improved DOC formulations, aiming to achieve 90% conversion of pollutants by 150 °C [53].

1.3 Impact of SO_2 on Oxidation Catalysts

Small amounts of sulfur originating from both fuel and lubricating oils are the cause of the main chemical degradation mode of oxidation catalysts, due to the strong chemisorption of sulfur species on the catalyst surface [54]. Because of the adverse impact of sulfur on aftertreatment performance, the EPA has mandated an average sulfur content of 10 ppm in gasoline and 15 ppm in diesel [8]. The most common sulfur form found in the exhaust is sulfur dioxide (SO_2); however, in the presence of oxygen and water vapor, SO_2 can be further oxidized on the oxidation catalyst to SO_3 and H_2SO_4, thereby compromising the performance of downstream catalysts. Exposure to SO_2 leads to the formation of different sulfur species on the catalyst surface, which depends on the catalyst composition. In most cases, these sulfur species accumulate on the surface and inhibit reaction pathways from occurring on the precious metal sites. Even though the current research goal in oxidation catalysts focuses on developing more active and stable formulations, there is also a need to ensure resilience against sulfur poisoning.

1.4 Regeneration Strategies after Sulfur Poisoning

Due to the strong chemisorption of sulfur species on the catalyst surface, regeneration strategies often require subjecting the catalyst to high temperatures (> 600 °C) under different reaction conditions. These conditions may vary depending on what type of sulfur species are on the catalyst surface. Typically, reducing environments at high temperatures leads to the highest rate of decomposition of sulfur species, enhancing the overall recovery of catalytic activity. A critical aspect of implementing these regeneration strategies is selecting conditions that may not induce further/other deactivation (i.e., agglomeration of active and support materials).

1.5 Research Objectives

Evaluating the sulfur resistance of new oxidation catalyst formulations and understanding their regeneration remain crucial for aftertreatment implementation due to the persistent presence of sulfur in fuels or oils. With this in mind, we assessed the effects of sulfur poisoning and regeneration on a new methane oxidation catalyst formulation that integrates spinel oxides as the oxygen storage material. The extent of catalyst regeneration, concerning both catalytic activity and oxygen storage, depended on the ability of inducing the decomposition of high temperature sulfur species. For this reason, key regeneration parameters – temperature, feed composition, and cycling parameters – were evaluated. Next, we examined the effects of sulfur exposure and regeneration of a bimetallic Pd-Cu diesel oxidation catalyst. Our findings showed that a small substitution of Cu not only provides enhanced sulfur resistance but also improves regenerability, particularly under reducing conditions. Finally, we expanded our understanding of how initial particle size and aging protocols influences sulfur speciation, thereby shedding light on their impact on oxidation activity and sulfur resistance.

2. Effects of SO_2 poisoning and regeneration on spinel containing CH_4 oxidation catalysts

This chapter contains published work found in N. Diaz Montenegro and W. S. Epling, "Effects of SO_2 poisoning and regeneration on spinel containing CH_4 oxidation catalysts," Appl. Catal. B Environ., vol. 336, no. February, p. 122894, 2023. Responses to committee questions can be found in Page 47.

2.1 Abstract

Methane oxidation under periodic conditions and the oxygen storage capacity of a bilayer $Pt/Pd/Al_2O_3$ over a $Mn_{0.5}Fe_{2.5}O_4$ spinel catalyst were studied before and after SO_2 exposure, and after simulated regeneration conditions. Prior to sulfur exposure, improvement in CH_4 oxidation conversion under periodic conditions compared to steady-state conditions was observed. After sulfur exposure at 100 °C, there was a loss in CH_4 oxidation performance and a loss of oxygen storage capacity of the spinel material. The extent of regeneration from sulfur poisoning depends on the ability to induce the decomposition of sulfate species, and while all regeneration methods tested in this study did improve CH_4 conversion, regeneration methods under periodic conditions induced greater sulfur species desorption from the catalyst surface leading to improved CH_4 conversion. Key regeneration parameters – temperature, feed composition, modulation amplitude and frequency – were optimized to induce S species decomposition and correlated to CH_4 oxidation activity recovery.

2.2 Introduction

Due to the abundance of natural gas in the United States [55] and relatively high fuel efficiency, natural gas engines are an attractive alternative to gasoline or diesel engines. In terms of emissions, they release less NO_x, CO and particulate matter into the atmosphere compared to diesel engines [56], [57]. However, the main hydrocarbon found in natural gas is methane (CH_4), and since CH_4 is a powerful greenhouse gas [58], limiting CH_4 emissions from natural gas engine exhaust is necessary to lessen the effects of global warming and to comply with the 0.1 g/bhp-hr methane emission standard for heavy-duty vehicles and 0.05 g/mile for small pick-up trucks and vans set by the Environmental Protection Agency [8]. Current methane oxidation catalysts (MOCs), which operate at the stoichiometric air-to-fuel ratio, run into several challenges. First, due to the stable C-H bond (450 kJ/mol) and low sticking coefficient of CH_4 [59], [60], high exhaust aftertreatment temperatures ($T > 500$ °C) and high precious metal loadings are needed to significantly reduce CH_4 emissions. Second, the mode of engine operation at the stoichiometric point provides a rather narrow window for the simultaneous conversion of CH_4, CO and NO_x. Third, the added sulfur-based odorant to natural gas can lead to a loss in MOC performance over time [20], [57], [61]. Based on these reasons and others, the development of new MOC formulations is needed to improve low temperature CH_4 oxidation activity.

Commercial MOCs are composed of a cordierite substrate in a honeycomb structure, on which a high surface area support, such as Al_2O_3 combined with a CeO_2-based oxygen storage material is washcoated. On this high surface area support, a combination of Pt group metal (Pt, Pd, or Rh) nanoparticles is deposited [22], [57], [61].The precious metal materials are the active centers where MOC chemistry occurs (Eq. 2.1-2.3).

$$CH_4 + 2O_2 \rightarrow CO_2(CO) + 2H_2O \tag{2.1}$$

$$CO + {}^{1}\!/_{2}\,O_2 \rightarrow CO_2 \tag{2.2}$$

$$CH_4 + 4NO \rightarrow 2N_2\,(N_2O, NH_3) + CO_2 + 2H_2O \tag{2.3}$$

The CeO_2-based oxygen storage material is added to MOC formulations to alleviate the effects of changes in the air-to-fuel ratio during operation. In oxygen-deficient environments, CeO_2 reduces to CeO_{2-x}, and the released oxygen is used in the reactions described above (Eq. 2.1-2.2), which also creates oxygen vacancies at the surface. Once there is excess oxygen, oxygen vacancies are replenished with gas-phase O_2 leading to the re-oxidation of CeO_2 to maintain the air-to-fuel ratio at stoichiometric conditions (Eq. 2.4) [62], [63].

$$CeO_2 \leftrightarrow CeO_{2-x} + \frac{x}{2} O_2 \tag{2.4}$$

Current research trends prioritize improving precious metal utilization and new material discovery to promote MOC performance and tackle the challenges mentioned above. Due to their low cost, catalytic tunability and high abundance, spinel materials have been explored as candidates for diesel aftertreatment technologies, especially for hydrocarbon, soot and NO_x removal [64], [65], [74], [66]–[73]. Spinel oxides have an AB_2O_4 crystal structure, where A^{2+} transition metal ions occupy tetrahedral sites, while B^{3+} ions occupy octahedral sites in the lattice. As potential oxygen storage materials, spinel materials show promise as the lattice oxygen in the framework can be used without any structural impact. For example, Cu-Mn spinel materials have more readily available oxygen during transient conditions compared to commercial CeO_2-based oxygen storage materials [75], [76]. Plus, the addition of these spinel-based oxygen storage materials could also reduce the amount of PGM added to MOC formulations [77]–[79].

Due to their difficulty in being oxidized, one way to improve low temperature conversion of saturated hydrocarbons, such as methane [80]–[83] and propane [84], is by periodically changing the oxygen concentration in the feed composition. For Pt-based catalysts, the improvement in low temperature CH_4 conversion under periodic conditions is due to the formation of a partially oxidized Pt surface that favors methane dissociation at lower temperatures. Plus, periodic conditions mitigate the oxygen poisoning effect on Pt active sites. Previous studies have reported that under periodic operation, the temperature at which 50% CH_4 conversion is achieved under a simulated exhaust feed over a dual-layer MOC formulation that includes a PGM layer (Pt:Pd 19:1, 30g/ft^3) and a $Mn_{0.5}Fe_{2.5}O_4$ spinel layer (25wt% $Mn_{0.5}Fe_{2.5}O_4/Al_2O_3$, 100g/L) decreased by ~85 °C compared to steady-state inlet conditions [79]. The addition of the $Mn_{0.5}Fe_{2.5}O_4$ spinel as an oxygen storage material provided extra oxygen during the oxygen-deficient phases during periodic conditions, which maintained the oxygen balance closer to the stoichiometric point and curbed the production of undesirable byproducts, such as NH_3 [79]. The catalyst structure of this MOC formulation can also be designed to maximize the storage/release capabilities of $Mn_{0.5}Fe_{2.5}O_4$ layer under periodic conditions [85] and minimize potential inhibitory effects that may occur at high temperatures, such as species migration and active Pt site blockage [85], [86]. Periodic operation can also be optimized by finding an optimal amplitude and frequency to promote CH_4 oxidation activity [86]–[88].

Natural gas exhaust contains ppm levels of SO_2 due to the combustion of the odorant added to the fuel. Over time, these low levels of SO_2 may have a detrimental effect on catalyst performance and structure, but the extent of deactivation depends on the precious metal and support used [54], [61], [89]–[91]. In the case of Pd-based catalysts, SO_2 can strongly chemisorb to Pd sites and form inactive $PdSO_4$ species [90], [92], [93]. Unlike Pd, Pt sites do not form $PtSO_4$ species, but weakly adsorbed S species, such as sulfides and molecular SO_2, can form [94]. Regarding the support, sulfating supports, such as Al_2O_3 and CeO_2, interact with SO_2 to form sulfate species (SO_4^{-2}) allowing precious metal sites to remain available until the support is saturated. On the other hand, non-sulfating supports, such as SiO_2, are not able to form sulfate species leaving precious metals the only site where SO_2 can chemisorb [89], [95]–[99]. Additionally, reaction conditions, especially the presence of oxygen and adsorption temperature, and precious metal nanoparticle size affect the formation of more oxidized S species, such as sulfite (SO_3^{-2}) and sulfate (SO_4^{-2}) species [94], [100], [101]. Ultimately, the presence of S-related species leads to the loss of CH_4 oxidation performance due to inhibition of active sites and chemistry at the metal-support interface, especially for CeO_2-based supports. However, the addition of small amounts of Pt to Pd-based methane oxidation catalysts does offer some sulfur resistance [100], [102]–[104]. There is ample literature regarding PGM-based aftertreatment catalyst materials and the impact of S on them; however, since transition metal oxides have become an alternative to PGM-based aftertreatment systems, their sulfur resistance must also be assessed for implementation. For example, Mn-based catalysts can easily form $MnSO_4$ species which leads to the loss of active sites, especially for NO oxidation [105], [106].

To recover performance, the effects of SO_2 poisoning can be reversed via a catalyst regeneration strategy. Common regeneration techniques usually involve high temperature treatments to induce the decomposition of the adsorbed S species from the catalyst surface [101], [103], [114]–[120], [104], [107]–[113]. For example, Pt/Pd-based catalysts supported on Al_2O_3, molecular SO_2 and surface SO_3^{-2} species decompose and desorb around 400 °C from the catalyst surface, while more stable S species, such as SO_4^{-2}, do not decompose until temperatures higher than 600 °C [100]. Regarding the regeneration of Pd active sites, the regeneration environment influences the final Pd state after $PdSO_4$ decomposition, which affects methane oxidation activity recovery [120], [121]. One way to lower the temperature of the decomposition of the adsorbed S species from the catalyst surface is by altering the regeneration environment. For example, reducing environments with H_2 at 600 °C were found to remove all SO_4^{-2} species which led to the full recovery of CH_4 oxidation performance for Pd-based catalysts [107]. Other studies have shown sulfate decomposition at high temperature could also be induced by alternating the feed composition between the presence of a reductant (i.e., CH_4) and the presence of oxygen [108], [109], [112].

While the addition of a $Mn_{0.5}Fe_{2.5}O_4$ spinel layer to bimetallic Pt-Pd catalysts has been studied in terms of CH_4 oxidation, steam reforming, and under periodic conditions [79], [85], [86], [122], [123], the effects of SO_2 on this MOC formulation have yet to be explored, which is imperative for aftertreatment implementation. Here, we have studied the effects of SO_2 and model catalyst regeneration protocols on CH_4 oxidation performance and oxygen storage capacity of a bilayer PGM + $Mn_{0.5}Fe_{2.5}O_4$ spinel catalyst under steady-state and inlet feed modulated conditions. We focused on the response to SO_2 of the $Mn_{0.5}Fe_{2.5}O_4$ spinel material as an oxygen storage material, and its impact on CH_4 oxidation performance. Different regeneration methods were applied and evaluated in terms of CH_4 oxidation activity recovery and S species desorption, measured as SO_2, from the sample. Then, temperature, feed composition and modulation parameters, such as amplitude and frequency, were evaluated during regeneration for their impact on inducing the decomposition of S species on the catalyst, to improve CH_4 oxidation performance.

2.3 Experimental Methods

2.3.1 Catalyst Information and Experimental Set-up

All powder and monolith samples were provided by CDTi Advanced Materials, Inc, and a summary of their compositions and configurations is displayed in Figure 2-1 and Table 7-1. The PGM only monolith sample is a single-layer catalyst that is wash-coated onto a cordierite monolith substrate. The catalyst is composed of Pt/Pd deposited onto Al_2O_3. The Pt:Pd loading is 30 g/ft^3 of monolith, with a Pt:Pd mass ratio of 19:1. The PGM + spinel monolith sample is a dual layer catalyst that includes a top layer of the same Pt/Pd catalyst, and a bottom layer of $Mn_{0.5}Fe_{2.5}O_4$ spinel material. The spinel layer loading is 2832 g/ft^3 with 25 wt% spinel material supported on Al_2O_3. Both layers were wash-coated, sequentially, onto a cordierite monolith. For experiments with the monolith samples, the gas hourly space velocity (GHSV) was 60,000 hr^{-1} with a total flowrate of 1 L/min. Monolith samples were 6 mm in diameter and 28 mm in length. The $Mn_{0.5}Fe_{2.5}O_4$ spinel powder (referred to as Mn-Fe spinel powder) includes the spinel material with the same composition as the spinel layer of the monolith sample, i.e. 25% spinel on Al_2O_3. For the powder sample experiments, 15 mg of spinel powder was diluted with 150 mg of cordierite, and a total flowrate of 300 sccm was used. Prior to all experiments, all catalysts were pretreated in 10% O_2 in N_2 at 550 °C for 45 minutes. Surface area and precious metal dispersion have been reported in previous studies [85].

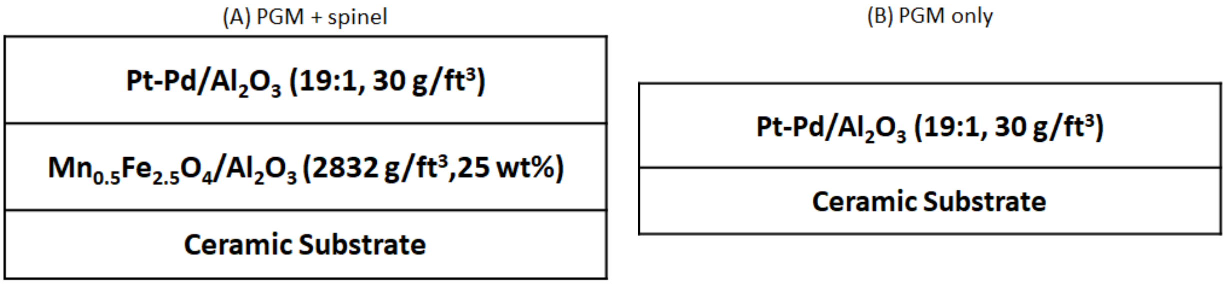

Figure 2-1 Compositions and configuration for the monolith samples: (A) PGM + spinel and (B) PGM only.

Each catalyst sample was placed in a quartz tube inside a Thermo Scientific Lindberg/Blue tube furnace as part of a flow reactor system. Bronkhorst and MKS mass flow controllers were used to adjust inlet gas flowrates. Type K thermocouples at the catalyst inlet and outlet were used to monitor the temperature, and the inlet temperature was used to plot results. For all experiments, outlet CH_4, CO, CO_2, H_2O, SO_2, SO_3 and COS gas concentrations were measured using an MKS MultiGas 2030 FTIR Spectrometer gas analyzer. Data were acquired at a rate of 1 Hz. To provide the gas mixtures, specialty gas cylinders were purchased from Praxair Inc and N_2 was generated using an OnSite Gas System N-20 nitrogen generator. Water vapor was introduced using a Bronkhorst CEM system. To avoid sulfur deposition along the reactor lines, stainless steel reactor lines treated with a sulfinert coating were purchased from Swagelok. Reactor lines were heated to temperatures above 100 °C to avoid water condensation.

2.3.2 CH_4 Oxidation Activity and Oxygen Consumption Measurements

The CH_4 oxidation activity assessment was performed using a temperature programmed reaction protocol with a temperature ramp of 5 °C/min. For periodic operation experiments, an inlet gas composition of 1500 ppm CH_4, with varying O_2

amounts in a N_2 balance was used. For the preliminary experiments in Figure 2-2, the oxygen concentration of the inlet gas was varied from 3000 ppm to 1%. For these experiments, a four-way solenoid air control valve purchased from Grainger (Part #6JJ44) was used to switch between O_2/N_2 flow and N_2. For steady-state experiments, the inlet oxygen concentration was 2750 ppm. Note, water was not included in the bulk of the experiments. Although water is ubiquitous in combustion exhaust gas, we intentionally excluded it to keep things simpler as we begin to understand this relatively new catalytic system.

As a measure of the available reactive oxygen on the Mn-Fe spinel material, the amount of O consumed during a 2-minute CO pulse – $O_{consumed}$ – was calculated between 200 and 600 °C in increments of 100 °C. After the O_2 pretreatment at 500 °C, the reactor was cooled to 200 °C in the presence of 10% O_2 in N_2. Once the temperature stabilized, oxygen was turned off and a N_2 purge was introduced for 15 minutes. Using the four-way switching valve, a pulse of 0.8% CO in N_2 was introduced for 2 minutes, and the concentration of CO_2 was monitored. After 5 minutes, 10% O_2 in N_2 flow was reintroduced to the reactor to reoxidize the sample, and the temperature was increased. Assuming that the oxygen that leads to the production of CO_2 comes exclusively from the Mn-Fe spinel material, $O_{consumed}$ was calculated using Eq. 2.5 using the CO_2 produced during the 2-minute CO pulse divided by the mass of the catalyst, $m_{Mn\text{-}Fe\ spinel}$. This measurement provides a way to evaluate changes in the available O in the spinel as a function of temperature, S exposure and regeneration conditions. Periodic operation conditions used less than 2-minute cycles, this $O_{consumed}$ value was simply used to probe the changes in the available oxygen of the Mn-Fe spinel material.

$$O_{consumed} = \frac{\int_0^t [CO_2]dt}{m_{Mn-Fe\,Spinel}} \tag{2.5}$$

2.3.3 Sulfur Poisoning

To assess the effects of SO_2 exposure on the CH_4 oxidation activity and the amount of available O in the 2-minute CO pulse, $O_{consumed}$, the samples were exposed to 10 ppm of SO_2 in a N_2 balance at 100 °C after the 550 °C pretreatment described above. Once the SO_2 outlet concentration recorded by the FTIR reached the inlet 10 ppm concentration, a N_2 purge was introduced to clear the lines and remove weakly absorbed sulfur species from the sample. Then, the CH_4 oxidation temperature programmed reaction activity test, as described above, was again performed. For the oxygen consumption measurements, after SO_2 exposure at 100 °C, SO_2 was turned on during the reoxidation steps between each temperature and turned off during the N_2 purge and CO pulse duration.

2.3.4 Catalyst Regeneration

Different regeneration methods were applied and evaluated in the recovery of CH_4 oxidation activity and the amount of available O in the 2-minute CO pulse, $O_{consumed}$. After SO_2 exposure at 100 °C, each sample was either exposed to 10% O_2, 3% H_2 or 0.8% CO in N_2 and a 10 °C/min temperature ramp to 600 °C, followed by an isothermal hold at 600 °C for 45 minutes. After each regeneration treatment, the sample was pretreated in 10% O_2 in N_2 balance at 550 °C for 45 minutes. Then, the reactor was cooled down to 100 °C in the presence of 10% O_2 in N_2 balance, and the CH_4 oxidation and oxygen consumption activity tests were performed.

Separately, higher temperature regeneration methods were also used. Table 1 summarizes the regeneration conditions the catalyst sample experienced for 45 minutes at 700 °C after SO_2 exposure at 100 °C. For these regeneration treatments, the regeneration protocol is described by Schematic 7-1. After the CH_4 oxidation temperature programmed reaction, the temperature was held at 600 °C for 60 minutes. Then, the temperature was ramp at 10 °C/min to 700 °C under regeneration conditions described in Table 1, and the temperature was held for 45 minutes at 700 °C. The temperature was then lowered to 600 °C in CH_4 oxidation conditions.

Table 2-1 Regeneration operating conditions

#	**O_2 (%)**	**H_2 (%)**	**CH_4 (ppm)**	**Cycling Frequency (Hz)**
1	-	3%	-	N/A
2	0/0.55%	-	1500	0.25
3	0/0.55%	-	1500	0.0625
4	0/0.55%	0.1%	1500	0.0625

2.4 Results and Discussion

2.4.1 Role of $Mn_{0.5}Fe_{2.5}O_4$ addition on CH_4 oxidation during periodic conditions

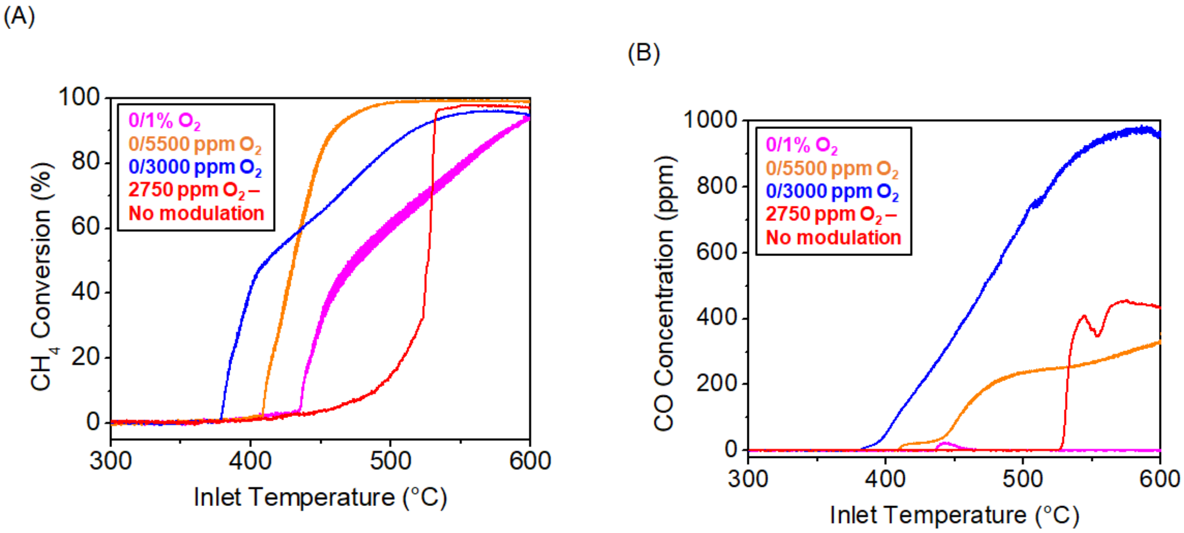

Figure 2-2 (A) CH_4 conversion and (B) CO formation using the PGM + spinel sample under no modulation and with periodic conditions during the CH_4 temperature programmed reaction.

First, we investigated the effects of periodic conditions on methane oxidation activity using the PGM + spinel sample. Such periodic conditions not only mimic realistic operation conditions more closely due to changes in the air-to-fuel ratio (AFR) during the driving cycle, but also the varying oxygen concentration over the catalyst surface improves catalytic performance [124]. Figure 2-2A shows the methane conversion on the PGM + spinel sample with no modulation and with periodic conditions. Under periodic conditions, the onset temperature for methane conversion increases with increased oxygen concentration in the oxygen containing phase. The methane oxidation onset temperature was highest under no modulation conditions. This is also consistent with prior literature, where when including H_2O in the mixture the same improvement with modulation was noted [79]. The initial increase in conversion as a function of temperature is also faster with modulation. The onset temperature increasing with increasing oxygen suggests that the formation of the more active partially oxidized Pt surface that occurs during periodic conditions depends on the oxygen concentration of the inlet gas, as might be expected. The formation of CO during periodic and no modulation conditions is shown on Figure 2-2B. The presence of byproduct CO indicates that partial oxidation (Eq. 2.6) and/or steam reforming (Eq. 2.7) of CH_4 occurred. For the lowest O_2 concentration under modulation conditions, 3000 ppm, as temperature increased past 400 °C, the rate of change in CH_4 conversion as a function of temperature slows due to the lack of oxygen availability, which also leads to the greater formation of CO. In the case of the highest O_2 concentration in the O_2-containing phase, 1%, the more abundant oxygen may lead to oxygen poisoning of Pt sites at high temperatures which slows CH_4 conversion [81], [125]–[127]. As oxygen becomes more abundant, the formation of CO decreases as expected. With the intermediate 5500 ppm O_2 concentration, full conversion of CH_4 was achieved in the temperature range used. With no modulation conditions and the 3000 ppm oxygen, complete or near complete conversion of CH_4 was also achieved suggesting that enough O was available to oxidize CH_4 without poisoning the Pt sites; however, the onset of CH_4 oxidation occurs at higher temperatures compared to those that included modulation. Since the oxygen concentration is slightly lower than the stoichiometric point, under no modulation conditions, some CO formation is observed as well. The improved CH_4 conversion under periodic conditions on the PGM + spinel monolith sample has also been observed in previous studies [79], [85]. Furthermore, this improvement in CH_4 conversion under periodic conditions is observed under simple (CH_4 + O_2 + N_2) inlet gas conditions, such as those used to obtain the results in Figure 2-2, as well as more complex simulated exhaust feeds, such as one containing CH_4, O_2, H_2O, CO, H_2, NO and CO_2, as shown in Figure 7-1.

$$CH_4 + \frac{1}{2}O_2 \leftrightarrow 2H_2 + CO \tag{2.6}$$

$$CH_4 + \ H_2O \leftrightarrow 3H_2 + CO \tag{2.7}$$

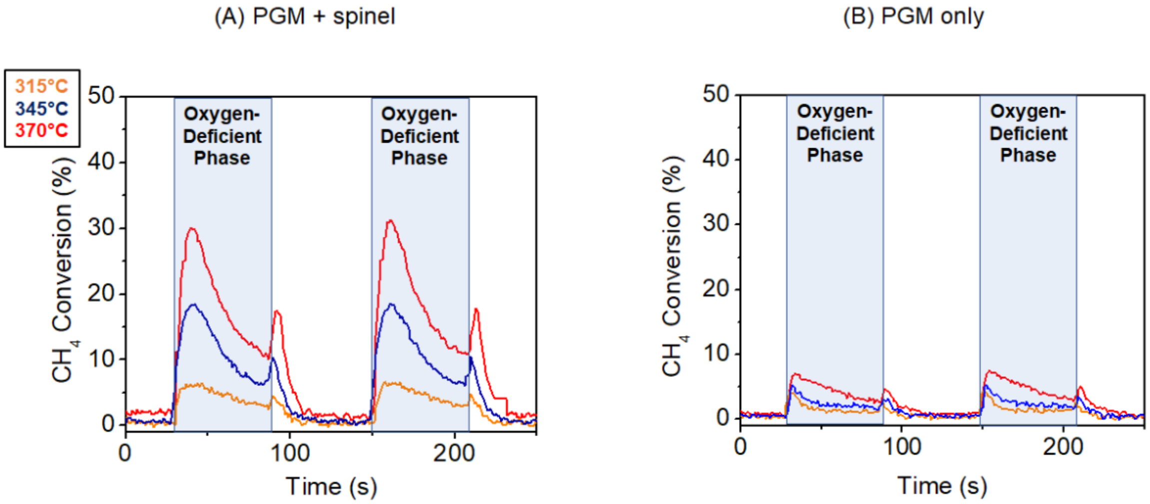

Figure 2-3 CH_4 conversion using 2-minute cycles ([CH_4] – 1500 ppm, [O_2] – 0/5500 ppm, N_2 balance) on (A) PGM + spinel and (B) PGM only samples as a function of time.

To corroborate that the addition of an oxygen storage material would improve catalytic performance of a PGM-based sample [28], [79], [85], we performed 2-minute cycles, with one phase containing O_2 and the other none ([O_2] = 0 or 5500 ppm) on both the PGM + spinel and PGM only samples. Methane conversions using this protocol at 315, 345 and 370 °C are shown in Figure 2-3, where the phases containing no oxygen have been shaded. For the PGM + spinel monolith sample, a sharp increase in CH_4 conversion is seen with the switch to the oxygen-deficient gas environment for all temperatures, and then the conversion eventually decreases with time. Once the feed switches to the oxygen-containing environment, only a slight increase in methane conversion is observed and quickly decreases. In the following oxygen-absent phase, the high CH_4 conversion peak is again observed. In the case of the PGM only sample, only a small peak in CH_4 conversion is observed during the switch to the oxygen absent phases, and no conversion is observed during the oxygen-containing phases. The 2-minute cycle results show that the incorporation of the Mn-Fe spinel layer with the PGM leads to an increase in CH_4 conversion during the oxygen-deficient phases compared to the PGM only sample. This has been attributed to the ability of the Mn-Fe spinel layer to store and release oxygen depending on the operating conditions, while maintaining precious metal sites in a more favorable oxidation state for CH_4 oxidation [79], [85]. As oxygen is released from the spinel lattice to the PGM sites during the oxygen-deficient phases, oxygen vacancies are created. Once oxygen is reintroduced into the feed, gas-phase oxygen dissociates, and the oxygen vacancies created in the spinel lattice are refilled. The 2-minute pulse experiment results suggest that oxygen from the Mn-Fe spinel layer is released during the oxygen-deficient phases and participates in the conversion of CH_4. However, this oxygen reservoir depletes over time leading to the CH_4 conversion decrease with time during this phase. In the oxygen-containing phase, the oxygen reservoir is replenished since in the next oxygen-deficient phase, the CH_4 conversion peak is of the same magnitude as the previous one. However, during the oxygen-containing phase, a small CH_4 conversion peak for all temperatures is observed due to the newly introduced oxygen; however, CH_4 conversion quickly ceases since the oxygen concentration during this phase leads to oxygen poisoning of the precious metal sites. Direct comparison of the CH_4 conversion under the CH_4 temperature programmed oxidation of these two catalysts can also be found in Figure 7-2.

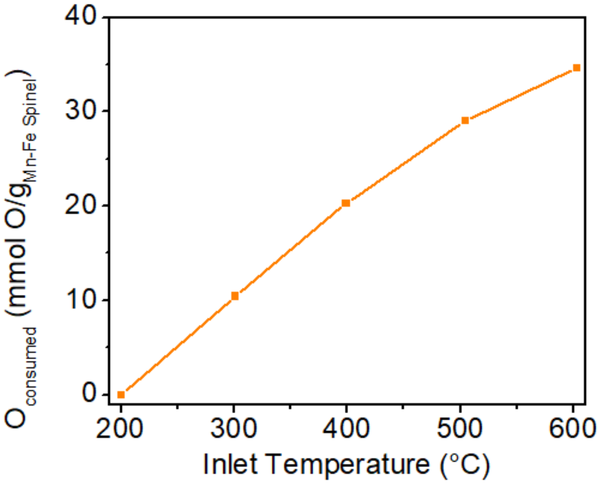

Figure 2-4 Calculated $O_{consumed}$ of the fresh Mn-Fe spinel powder sample as a function of temperature.

As a measure of O accessibility during the oxygen-deficient phases, the amount of oxygen consumed during a 2-minute CO pulse ($O_{consumed}$) for the Mn-Fe spinel material was calculated. Figure 2-4 shows these amounts from 200 to 600 °C. As temperature increases, the calculated $O_{consumed}$ from the Mn-Fe spinel material increases showing that more oxygen can be accessed during periodic conditions with increasing temperature. In the presence of a reductant, for example CO, Mn and Fe cations in the spinel lattice can reduce to their metallic forms (shown in Eq. 2.8 and 2.9), which would release lattice oxygen. This is what leads to the production of CO_2 during the CO pulse. Different extents of reduction, or different relative amounts of spinel being reduced, occur at each temperature. To rule out thermal decomposition of the Mn-Fe spinel as a possible oxygen source, a temperature programmed desorption (TPD) study showed that under inert flow conditions, although desorbed oxygen was observed at high temperatures, the total amount of oxygen released corresponds to only a small fraction (~0.1%) of the total oxygen storage capacity of the Mn-Fe spinel material [85]. Therefore, the oxygen that leads to the production of CO_2 during this CO protocol comes exclusively from the lattice oxygen released during the reduction of the Mn-Fe spinel material.

$$\mathrm{Mn_{0.5}Fe_{2.5}O_4} + \mathrm{CO} \rightarrow 0.5\mathrm{MnO} + 2.5\mathrm{FeO} + \mathrm{CO_2} \tag{2.8}$$

$$\mathrm{Mn_{0.5}Fe_{2.5}O_4} + 3.5\mathrm{CO} \rightarrow 0.5\mathrm{MnO} + 2.5\mathrm{Fe} + \mathrm{CO_2} \tag{2.9}$$

2.4.2 Sulfur Impact on CH_4 Oxidation Activity and $O_{consumed}$

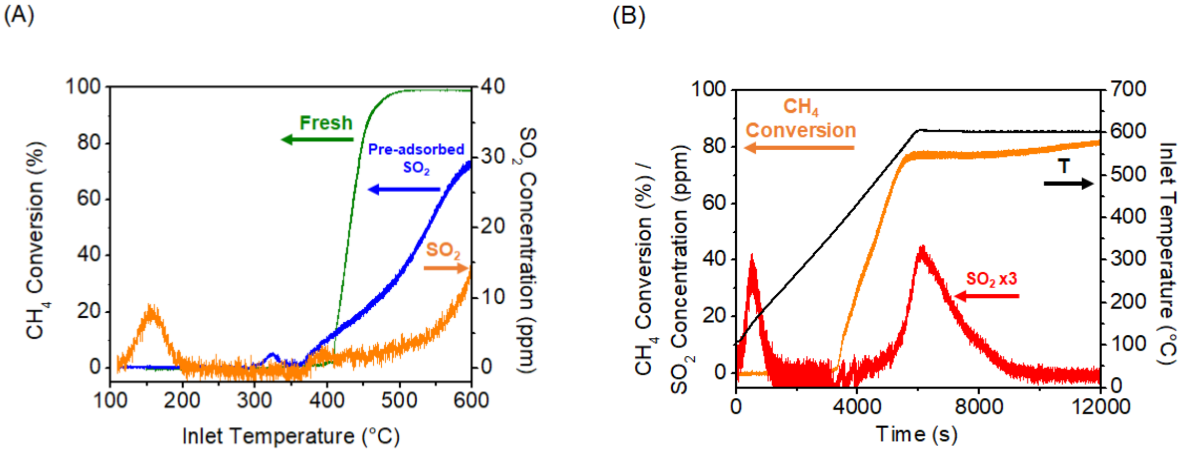

Figure 2-5 (A) CH_4 conversion before and after SO_2 exposure at 100 °C under periodic conditions and the SO_2 concentration during the CH_4 temperature programmed reaction, (B) CH_4 conversion and SO_2 profile after SO_2 exposure at 100 °C during the same experiment as shown in panel A, but also including the isothermal hold at 600 °C for 1 hour.

After SO_2 exposure at 100 °C, the CH_4 oxidation temperature programmed reaction under periodic conditions ($[O_2]$ – 0/5500 ppm, $[CH_4]$ – 1500 ppm, frequency – 0.25 Hz) was performed using the PGM + spinel sample. The CH_4 conversion for the fresh and SO_2-exposed samples, and the SO_2 concentration profile, representing the amount of SO_2 desorbed, during the temperature ramp are shown in Figure 2-5A. Sulfur exposure at 100 °C leads to both promoting and inhibiting effects on CH_4 oxidation. Between 370 and 400 °C, the CH_4 conversion is higher after SO_2 exposure, whereas at higher temperature the conversion is lower. An increase in low-temperature hydrocarbon conversion (specifically for propane [128]–[130] and methane [131]) has been previously reported on S-exposed Pt/Al_2O_3 catalysts. In the case of propane oxidation, the formation of new active sites at the metal-support interface promotes hydrocarbon dissociation. We speculate the same might occur here.

During the temperature ramp, two SO_2 desorption peaks were observed. No SO_3, COS or H_2SO_4 was detected. Based on the literature, the low temperature desorption peak (located at 150 °C) corresponds to the desorption of SO_2 from physisorbed SO_2 and decomposed sulfite (SO_3^{-2}) species on the catalyst surface, while the higher temperature desorption peak, located at temperatures above 500 °C, corresponds to the desorption of SO_2 from the decomposition of sulfate species [89], [96]–[99].

The temperature program was extended to include an isothermal hold at 600 °C to further look into the evolution of the higher temperature SO_2 desorption peak. Methane conversion on the PGM + spinel sample and the SO_2 profile during the latter part of the temperature ramp and the isothermal hold at 600 °C are shown in Figure 2-5B. During the isothermal hold at 600 °C, CH_4 conversion initially stayed constant at ~75%; however, after 30 minutes, CH_4 conversion began to slowly increase and continued to until the end of the isothermal hold. During the isothermal hold, the release of SO_2 was observed, and while SO_2 was observed, CH_4 conversion remained constant. Once SO_2 release ended, CH_4 conversion began to increase. During the initial part of the isothermal hold, the sulfate species were decomposing, likely those close to the active precious metal sites, or began migrating to the precious metal sites to decompose [132]. Ultimately, the decomposition of S species continues to influence precious metal sites in terms of CH_4 oxidation, and once those in proximity to the active sites are removed or the migration of S species toward the precious metal sites ceases, CH_4 conversion increases.

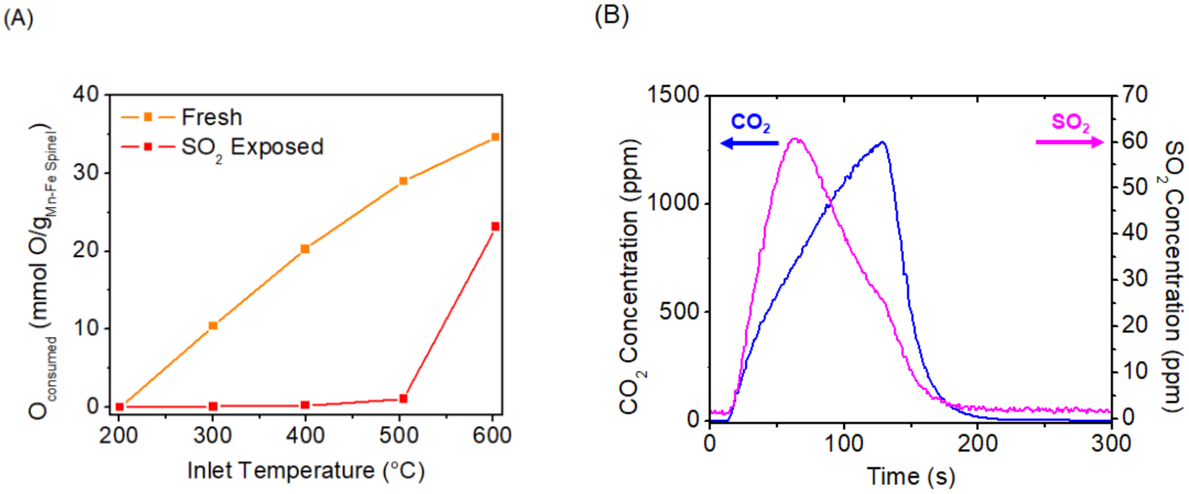

Figure 2-6 (A) Comparison of the calculated $O_{consumed}$ of the fresh and SO_2-exposed Spinel Powder sample; (B) CO_2 and SO_2 profile during the CO pulse at 600 °C from the SO_2-exposed Spinel Powder sample.

To assess the effects of SO_2 on the calculated $O_{consumed}$ of the Mn-Fe spinel layer during the 2-minute CO pulse, the amount of CO_2 formed during the CO pulse experiment was again calculated using just the Mn-Fe spinel powder. Figure 2-6A shows the comparison of the fresh and SO_2-exposed $O_{consumed}$ of the Mn-Fe spinel powder. In the presence of SO_2, little to no $O_{consumed}$ was observed in the 200 to 500 °C temperature range, suggesting that SO_2 poisons the reactive O sites on the Mn-Fe spinel powder. In terms of CH_4 oxidation under periodic conditions, no oxygen from the Mn-Fe spinel material would be provided which could also contribute to the shift in CH_4 conversion to higher temperatures observed in Figure 2-5A. No SO_2 desorption from the spinel occurred in this temperature range. However, $O_{consumed}$ was observed at 600 °C. At these high temperatures, as CO was introduced to the reactor, the appearance of both CO_2 and SO_2 was observed as shown in Figure 2-6B. CO reduces the high temperature sulfate species leading to the release of S from the catalyst surface. Once the CO pulse ends, SO_2 desorption ends.

2.4.3 Catalyst Regeneration Methods

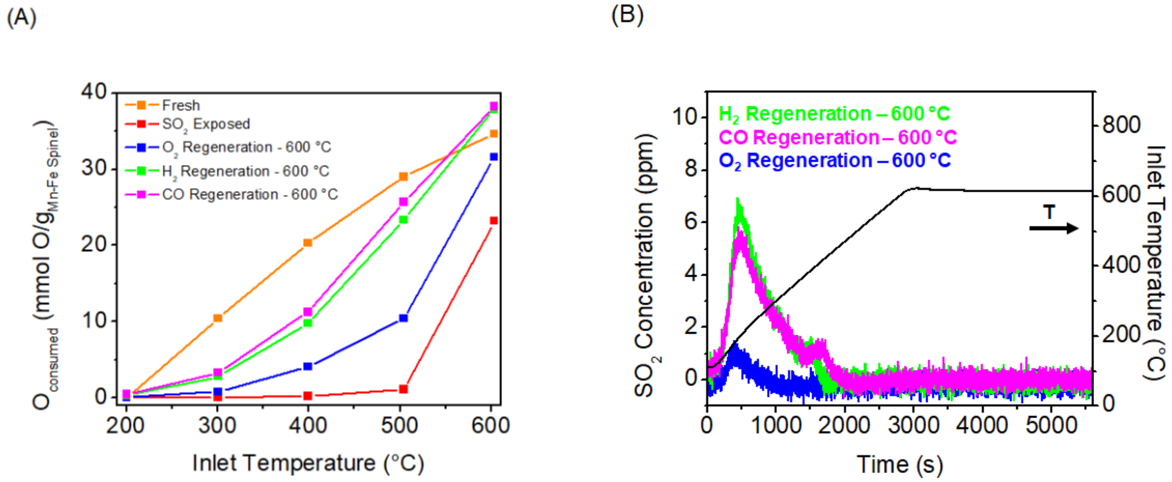

Figure 2-7 (A) Comparison of $O_{consumed}$ for the fresh, SO_2 exposed and regenerated Spinel Only powder; (B) SO_2 profile during the regeneration ramps.

Common literature regeneration methods, such as oxidizing and reducing environments, as well as oscillating between them, were used to assess their effectiveness in the decomposition of the adsorbed S species from the catalyst surface. This should lead to increased $O_{consumed}$ of the Mn-Fe spinel material, and based on the results shown above, should lead to an increase in CH_4 conversion. The recovery of the $O_{consumed}$ during the 2-minute CO pulse of the Mn-Fe spinel material was first assessed, and the best regeneration method was then used to verify if CH_4 oxidation activity was recovered over the PGM + Spinel sample. Figure 2-7A shows the comparison of the $O_{consumed}$ of the fresh, SO_2-exposed, and regenerated Mn-Fe spinel powder after three different regeneration methods. A regeneration temperature of 600 °C was chosen based results shown in Figure 2-5B and 2-6B, as well as literature results that show that this temperature can induce the decomposition of S species, especially sulfate (SO_4^{-2})

species [107]. All regeneration methods successfully recovered some $O_{consumed}$ for the Mn-Fe spinel powder, with the extent of recovery a function of the gas composition during the regeneration treatment. Figure 2-7B shows the SO_2 profiles during the regeneration temperature ramp before the isothermal hold at 600 °C for 45 minutes. The SO_2 desorption profiles under reducing environments (in H_2 and CO, 32 and 35% of the SO_2 that was adsorbed, respectively) are far greater compared to the SO_2 desorption during oxidative conditions, which was only ~2% of that that adsorbed, consistent with prior results [50,60,64]. A sulfur mass balance during the adsorption and regeneration phase for these three regeneration treatments can be found in Table 2-2. Reducing environments induce more decomposition of the sulfate species (% desorbed > 30%), compared to the treatment in O_2 (% desorbed ≈ 2%).

Table 2-2 S mass balance after regeneration of the Mn-Fe spinel powder samples

Regeneration Temperature (°C)	**Regeneration Conditions**	**SO_2 Adsorbed (μmol)**	**SO_2 Desorbed (μmol)**	**% Desorbed**
600	10% O_2 + N_2	3.0	0.1	2.3
600	3% H_2 + N_2	2.7	0.9	32
600	0.8% CO + N_2	2.6	0.9	35

Sulfates are readily formed on Al_2O_3 and CeO_2 with exposure to SO_2 [97]. Such sulfate species, on Pd/CeO_2 at least, decompose at lower temperatures in a reducing environment relative to an oxidizing environment [100], [118], [119] consistent with our observations. This is due to the reductant exposure leading to sulfate reduction and then S species desorption, whereas under oxidizing conditions, the sulfates remain stable to higher temperatures. Interestingly, reducing environments in both H_2 and CO at 600 °C led to an increased measure of $O_{consumed}$ at 600 °C compared to the fresh sample. In the literature, it has been hypothesized that oxygen from the decomposition of SO_4^{-2} species in CeO_2-based materials may contribute to the oxygen storage capacity process [86]. At 600 °C, as shown in Figure 2-6B and Figure 7-3, the CO pulse at 600 °C not only leads to CO_2 formation via consumption of oxygen from the spinel lattice, but also the desorption of SO_2 from the decomposition of sulfate species, which could lead to the increased $O_{consumed}$ compared to the fresh sample. Note, since the S mass balance did not close for all regeneration treatments, there is remaining S on the catalyst surface, and it still could impact catalytic activity.

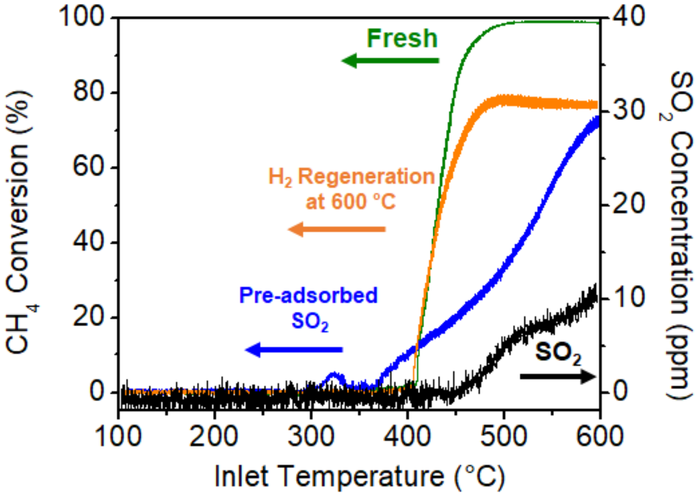

Figure 2-8 Comparison of the CH_4 conversion using fresh, SO_2 exposed and H_2 regenerated PGM + Spinel monolith samples, and the SO_2 profile during the CH_4 oxidation temperature reaction ramp after H_2 regeneration.

Based on the recovery of $O_{consumed}$, reducing treatments can effectively regenerate the ability for the Mn-Fe spinel material to provide lattice oxygen by inducing the decomposition of S species from the catalyst surface. Reducing treatments were therefore applied to the PGM + spinel sample to assess if CH_4 oxidation activity was recovered. Figure 2-8 shows the CH_4 conversion obtained using the fresh, SO_2-exposed, and H_2- regenerated at 600°C samples, and the SO_2 concentration profile during the temperature ramp after the H_2 regeneration at 600 °C. At low temperatures (< 450°C), the H_2 regeneration at 600 °C successfully recovered all CH_4 oxidation activity since CH_4 conversion profiles matched that for the experiment using the fresh sample. However, at higher temperatures, the rate of change in CH_4 conversion as a function of temperature slowed and ultimately only achieved ~77%. In evaluating the SO_2 desorption profile during the CH_4 oxidation temperature ramp, as CH_4 conversion achieves its maximum, SO_2 desorption is observed before the end of the temperature ramp. The sulfur mass balances during adsorption and desorption during the regeneration and CH_4 oxidation ramps can be found in Table 2-3. The amount of S adsorbed on the Mn-Fe spinel material found in Table 2-2 was used to extrapolate the amount of S adsorbed on the Mn-Fe spinel layer of the PGM + spinel monolith sample, which corresponds to 18.1 μmol. Using the total SO_2 adsorbed found in Table 2-3 (38.1 μmol), the amount of S adsorbed on the PGM layer is 20 μmol. Since the amount of S adsorbed on the PGM layer (total amount of PGM is 5.6 μmol) is slightly higher than the amount of S adsorbed on the Mn-Fe spinel layer, the addition of the PGM layer does influence S adsorption and spillover onto the Al_2O_3 support.

Table 2-3 S mass balance after regeneration for the PGM + spinel monolith samples

Regeneration Temperature (°C)	Regeneration Conditions	SO_2 Adsorbed (μmol)	SO_2 Desorbed During Regeneration Ramp (μmol)	SO_2 Desorbed During CH_4 Oxidation Ramp (μmol)	% Desorbed
600	3% H_2 + N_2	38.1	14.2	7.3	56%
700	CH_4 + H_2 + cycled [O_2] – 0/5500 ppm at 0.0625 Hz	42	-	36	87%

Regarding the SO_2 desorption during the regeneration and CH_4 oxidation ramp, only 56% of the total SO_2 adsorbed was desorbed, suggesting that a fraction of S was decomposed under the regeneration and CH_4 oxidation steps, and the remaining S influences CH_4 oxidation performance. Since no low temperature desorbing S species were observed during the CH_4 oxidation temperature ramp, H_2 regeneration at 600 °C can decompose these species and recover $O_{consumed}$ from the Mn-Fe spinel material but falls short at inducing the decomposition of some other S species. Inhibition by SO_4^{-2} species is most likely impacting CH_4 oxidation performance, likely due to their stability and possibly also proximity to the active sites [113], [130], [134]. Furthermore, the pattern observed matches that in Figure 2-5B, where CH_4 conversion plateaued and only began increasing once SO_2 desorption stopped. Another concern with high temperature regeneration treatments is the potential of irreversible deactivation via precious metal particle sintering or changes in oxygen storage. However, exposing the PGM + spinel sample to these H_2 regeneration conditions, but with no SO_2 exposure at 100 °C, led to no differences in the CH_4 oxidation performance, as shown in Figure 7-4. Therefore, the unconventional CH_4 oxidation behavior at high temperatures is due to inhibition by residual SO_4^{-2} species, not caused by deactivation via sintering or changes in oxygen storage properties.

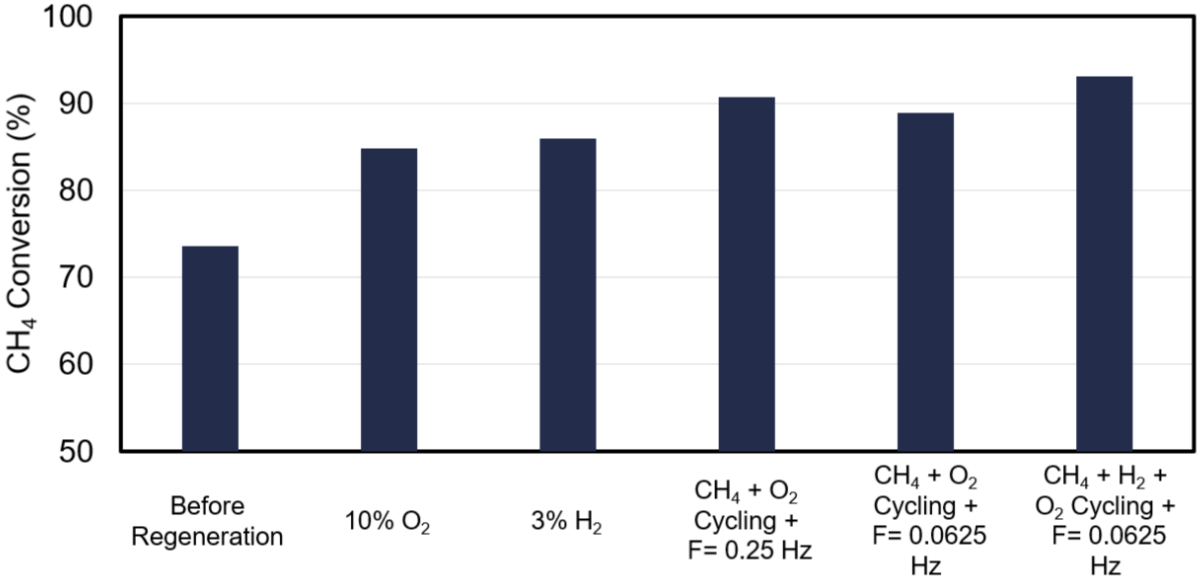

Figure 2-9 Summary of CH_4 conversion after regeneration at 700 °C using Schematic 7-1.

The effectiveness of the regeneration method at inducing the decomposition of S species depends on the gas composition as shown from the results above. However, those regeneration methods were not completely effective in the decomposition of stable SO_4^{-2} species, which have been noted to affect CH_4 oxidation activity at high temperatures [134]. Since the 600 °C regeneration technique induced the decomposition of some S species on the catalyst, increasing the regeneration temperature should lead to more S species decomposition. In the case of O_2 regeneration (Figure 7-5A), two higher regeneration temperatures were tested, 650 and 700 °C, using the protocol described in Schematic 7-1. After each regeneration step, CH_4 conversion improved and ultimately reached 85%. Interestingly, in evaluating the SO_2 profile during the regeneration protocol (Figure 7-5B), some SO_2 desorption occurred once CH_4 oxidation conditions were reintroduced after the O_2 regeneration steps. This suggests that during the O_2 regeneration steps, the oxidized precious metal sites do not lead to S species decomposition. With the switch to CH_4 oxidation conditions, even though oxygen was present, exposure to CH_4 as a reductant led to the decomposition of SO_4^{-2} species as desorbed SO_2. This is consistent with studies that have shown improvement in CH_4 conversion under regeneration methods where the feed composition alternates between periods of high oxygen concentrations and the presence of reductant (i.e., CH_4) [104], [108], [109]. In the case of H_2 regeneration (Figure 7-6A), regeneration temperatures at 650 and 700 °C were also tested. Methane conversion also improved after each regeneration step, again reaching 85% after regeneration at 700 °C; however, the rate of change in CH_4 conversion after each regeneration step was slower compared to the CH_4 conversion recovery after O_2 regeneration steps. No SO_2 desorption occurred during the regeneration steps at high temperatures or after the reintroduction of CH_4 oxidation conditions as shown in Figure 7-6B. Alternating between periods of high H_2 concentrations and the presence of CH_4 and O_2 does not appear to induce the decomposition of S species into SO_2.

Alternating the feed composition between reductant- and oxygen-rich phases has been shown to be an effective regeneration method at low temperatures (< 600 °C) [59,60]. To test how alternating the feed composition affects regeneration, the CH_4 oxidation conditions (CH_4 – 1500 ppm + $[O_2]$ – 0/5500 ppm + frequency = 0.25 Hz) were kept during temperature steps at 650 and 700 °C (Figure 7-7A). After both temperature steps, CH_4 conversion improved to 90% verifying that feed fluctuations between the two phases did improve regeneration and catalyst performance. In evaluating the SO_2 profile during this regeneration protocol (Figure 7-7B), only a small SO_2 desorption peak during the first regeneration ramp phase was observed. According to the literature, alternating the feed composition from reducing to oxidizing conditions leads to SO_2 release due to the reduction of stable sulfate species by CH_4 at the precious metal sites [108]. Even though SO_2 release during this regeneration was minimal, S species decomposition via the desorption of other S-containing species (i.e., H_2S) may have occurred.

Since amplitude and frequency are key parameters during periodic operation that affect CH_4 oxidation performance [86]–[88], these parameters can also potentially have an impact on the rate of S species decomposition on the PGM + spinel sample as well. First, the frequency of the [O_2] – 0/5500 ppm cycles was slowed from 0.25 to 0.0625 Hz. Figure 7-8A shows the CH_4 conversion after regeneration at 700 °C, and it improved from 73 to 89% at 600 °C. In evaluating the S profile (Figure 7-8B), some S desorbed from the catalyst surface in the presence of the regeneration gas conditions at 700 °C. Alternating the feed composition between the O-containing phase and its absence does lead to S release due to the reduction of sulfate species by CH_4 (or derived reductant). The faster frequency, 0.25Hz, did not induce as much SO_2 release as shown in Figure 7-7B. Slowing down the frequency to 0.0625 Hz may induce deeper reduction and/or also allow S species diffusion from the support to the precious metal sites which leads to more S species decomposition. Figure 2-9 shows a summary of the CH_4 conversions after the application of these different regeneration methods where key regeneration parameters, such as the regeneration temperature and the application of cycling, were introduced using the protocol described by Schematic 7-1.

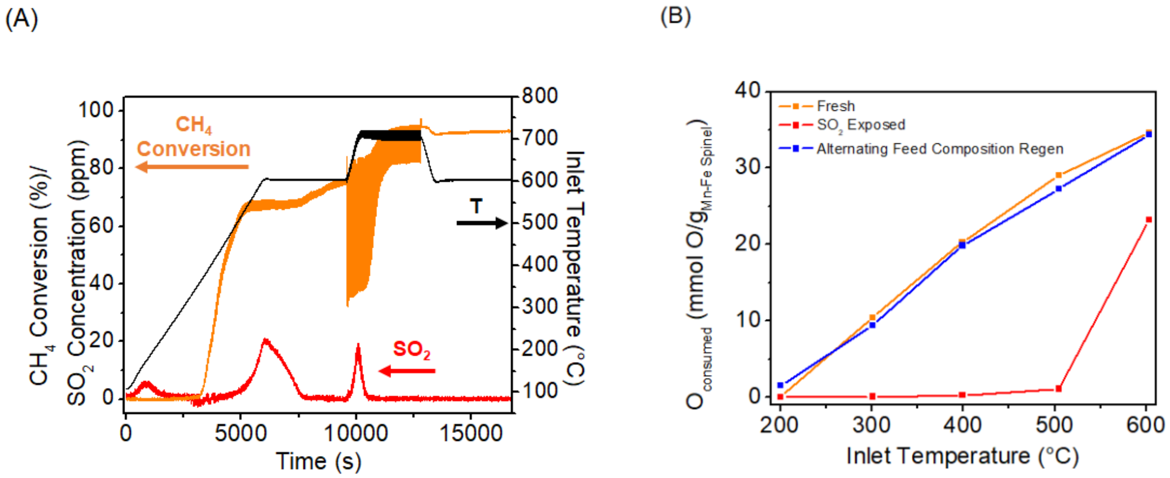

Figure 2-10 (A) CH_4 conversion and SO_2 profile after regeneration at 700 °C with CH_4 + H_2 and cycling O_2 at a frequency = 0.0625 Hz step using the PGM + spinel monolith sample; (B) Comparison of the $O_{consumed}$ for the fresh, SO_2 exposed and regenerated (700 °C, CH_4 + H_2 + [O_2] – 0/5500 ppm + frequency = 0.0625 Hz) Spinel Only powder.

Alternating the feed composition and optimizing cycling parameters during the regeneration process led to an increase in CH_4 conversion at 600 °C. The regeneration methods using cycling of the inlet gases discussed above include CH_4 as the reductant. Increasing the reductant concentration could lead to more S species decomposition during the regeneration step, which could in turn lead to an increase in catalyst performance. Figure 2-10A shows the CH_4 conversion and SO_2 profile before and after regeneration in a gas mixture that included H_2. The gas mixture was again modulated, with the O_2 cycling between 0/5500 ppm at a frequency of 0.0625 Hz, all at 700 °C. Note, the slower cycling frequency leads to more significant oscillations in the conversion as a function of time, especially at the higher temperature where deeper reduction can occur in the absence of O_2.With the addition of 0.1% H_2 to the regeneration feed composition,

CH_4 conversion improved from 73 to 93%. Table 2-3 shows the S balance during adsorption and desorption during the CH_4 oxidation temperature ramp. This regeneration method with H_2 included was able to induce the decomposition of 87% of the adsorbed S species, which led to the catalytic activity recovery at 600 °C. Figure 2-10B shows the comparison of the $O_{consumed}$ for fresh, SO_2-exposed, and regenerated Mn-Fe spinel powder using this regeneration protocol, and it successfully recovered all the $O_{consumed}$ lost after S exposure.

To evaluate any effects due to exposure at high temperature treatment, i.e., separate from that of S exposure combined with the high temperature treatment, a separate experiment was run duplicating all regeneration conditions excluding the sulfur exposure at 100 °C. Figure 7-9 shows that methane conversion dropped from 100 to 90% during the first isothermal hold at 600 °C, suggesting that high temperature deactivation might have likely occurred (i.e., sintering or changes in oxygen storage properties). These results suggests that deactivation due to exposure at 600 °C could have possibly affected the results for CH_4 oxidation and $O_{consumed}$ during CO pulse measurements after regeneration; however, high temperature exposure is needed for catalyst regeneration from S exposure. After the application of the regeneration step at 700 °C to the control sample, CH_4 conversion reached 89% at the second isothermal hold at 600 °C, showing that these regeneration conditions do not cause any further deactivation to the PGM + spinel sample. Comparing these control results with the high temperature regeneration results shown in Figure 2-10A, the combination of alternating the feed composition and optimizing cycling parameters regenerated the catalyst fully; however, thermal degradation did occur.

While some amount of CH_4 oxidation activity was recovered for all regeneration methods tested, the extent of regeneration depends on the ability to induce and drive the decomposition of SO_4^{-2} species, which influence the CH_4 oxidation performance at high temperatures on the PGM + spinel catalyst. Even though CH_4 conversion improved, regeneration methods with a constant feed composition (i.e., O_2 and H_2 conditions) did not induce the decomposition of all SO_4^{-2} species since no S release occurred during the regeneration steps as shown in Figure 7-5B and 7-6B. It is likely these conditions do not drive S species decomposition since a highly oxidized or reduced S species cannot be released as SO_2. Once a reductant (i.e., CH_4) is reintroduced into the feed after O_2 regeneration steps as shown in Figure 7-5B, the sulfate species can be reduced and S released as SO_2. In the case of H_2 regeneration, the small oxygen concentration during methane oxidation conditions might not be sufficient to drive SO_2 release from the highly reduced S species, or S was released during the regeneration step, but as H_2S which was not measured. The latter is likely given the recovery of some CH_4 oxidation activity. Alternating the feed composition from reducing to oxidizing conditions results in more sulfate decomposition via the release of SO_2, since it avoids the formation of highly oxidized or reduced S species. With this in mind, the effects of cycling parameters (i.e., frequency) should and do lead to differences in the released S profiles as shown in Figure 7-7B and 7-8B. Slower frequencies show a greater S release during the regeneration steps compared to the S release profile of the faster frequencies tested, suggesting that alternating the feed composition drives S diffusion on the catalyst surface. Ultimately, the decomposition of SO_4^{-2} species on the PGM + spinel catalyst is best achieved by the application of periodic operation in the presence of both reducing and oxidizing agents.

2.5 Conclusions

The effects of SO_2 and catalyst regeneration on the methane oxidation performance of a bilayer PGM + $Mn_{0.5}Fe_{2.5}O_4$ spinel catalyst operating under periodic inlet gas composition conditions were studied. Improvement in CH_4 conversion under periodic conditions relative to steady-state inlet gas composition conditions was observed. A measure of the reactive oxygen associated with the $Mn_{0.5}Fe_{2.5}O_4$ spinel was probed via CO pulse injection and showed that oxygen from its spinel lattice can be released and be an oxygen source during the oxygen-deficient phases during periodic conditions. After sulfur exposure at 100 °C, the CH_4 oxidation performance loss over the PGM + spinel catalyst was due to the influence of SO_4^{-2} on the catalyst, and the loss of reactive O of the spinel material. The extent of regeneration of the PGM + spinel catalyst is dependent on the ability to induce the decomposition of the more stable SO_4^{-2} species, and while all regeneration methods tested in this study do improve CH_4 conversion at 600 °C, regeneration methods under periodic conditions not only improved CH_4 conversion, but also induced greater S species decomposition from the catalyst surface.

2.6 Acknowledgements

The authors gratefully acknowledge CDTI for the samples provided. The authors also acknowledge funding support from the Department of Energy under contract DOE-EE0008332.

3. Effects of Hydrothermal Ageing and Sulfur Poisoning of PdCu Alloy Catalyst for Low-Temperature Diesel Oxidation Catalyst Applications

This chapter contains work in preparation in collaboration with Oregon State University.

3.1 Introduction

Catalytic oxidation is critical in pollution abatement, chemical production, and energy production technologies [135]. Pollution abatement for diesel vehicles is important as global use is expected to increase over the next 25 years [136]. Compared to gasoline-based engines, diesel engines offer high efficiency and durability while generating more torque, making them well-suited for heavy weight transportation [136]. Additionally, in terms of emissions, they release less CO_2 into the atmosphere [137]. The current diesel aftertreatment system is composed of a diesel oxidation catalyst (DOC), diesel particulate filter (DPF), selective catalytic reduction (SCR) catalyst, and ammonia slip catalyst (ASC). As the first unit operation of the current diesel aftertreatment system, the DOC is responsible for the oxidation of unburned hydrocarbons, carbon monoxide (CO), and nitric oxide (NO) as shown in Eqs. 3.1-3.3 [14], [17], [18].

$$\text{CO Oxidation: } CO + \frac{1}{2}O_2 \rightarrow CO_2 \tag{3.1}$$

$$\text{Hydrocarbon Oxidation: } C_xH_y + O_2 \rightarrow CO_2 + H_2O \tag{3.2}$$

$$\text{NO Oxidation: } NO + \frac{1}{2}O_2 \rightarrow NO_2 \tag{3.3}$$

Modern low-temperature combustion (LTC) diesel engines achieve high fuel efficiencies and release lower NO_x and particulate matter emissions compared to conventional diesel vehicles [51], [52]. However, due to the lower exhaust temperature, slower reaction kinetics over the DOC can lead to incomplete combustion and release of unburned hydrocarbons and CO. Therefore, designing DOCs that operate efficiently at low temperatures (< 150 °C) and high CO concentrations in the presence of competitive adsorbates should be considered [53].

Commercial DOCs contain precious metals (such as Pt and Pd) as the active centers for DOC chemistry. Due to their low availability and high price, current efforts to improve precious metal utilization primarily focus on synthesizing highly dispersed catalysts and altering current formulations via alloying. For example, single atom catalysts (SACs) are a promising avenue to achieve full precious metal use [43], [44], [138]. Typically, synthesis methods involve low metal loadings and reducible supports (i.e., CeO_2, MgO, Fe_2O_3) and SACs have been studied for CO oxidation [139], CH_4 activation [140], propane dehydrogenation [141]–[143], and other probe reactions. However, due to their low thermodynamic stability, they often agglomerate to form clusters and nanoparticles during reaction conditions [144] and deactivate in the presence of common catalyst poisons, such as H_2S [145].

Another way to reduce precious metal content while designing highly active surfaces is to improve current DOC formulations via alloying. Pt-Pd bimetallic systems have been implemented as DOC catalysts due to their higher catalytic activity and resistance to degradation through hydrothermal aging [146]–[148]. However, under LTC conditions where exhaust temperatures are low, these systems fail at oxidizing CO and NO simultaneously [149]–[153].

The incorporation of non-precious metals into DOC catalysts could offer an economical yet productive alternative. Particularly, the introduction of Cu to Pd catalysts has been explored for CO oxidation [154], [155], water gas shift [156]–[158], and selective hydrogenation of alkanes [159]–[161]. According to Kristy et al., the incorporation of Cu into Pd-based DOCs shows promising activity for CO oxidation under simulated exhaust conditions, even in the presence of competitive adsorbates [162]–[164]. Based on IR spectroscopy results, formation of surface nitrosyl species was not observed on the bimetallic sample, suggesting that the incorporation of Cu in Pd-based DOCs reduces NO adsorption on Pd active sites. However, as Cu substitution increases, CO oxidation activity decreases due to the Cu covering the active Pd surface [164].

Even though these bimetallic catalysts show promising CO oxidation activity, even in the presence of competitive adsorbates, new DOC formulations must be tested under more realistic conditions, and their response to hydrothermal aging and common catalyst poisons, such as SO_2, needs to be understood. For hydrothermal aging, exposure to water vapor at high temperatures has been known to induce agglomeration of the active components and physical changes to the oxide supports such as loss of surface area [165], [166].

Even though a 15 ppm standard for sulfur in diesel fuel has been set by the US Environmental Protection Agency (EPA) [167], the impact of this quantity over time has a detrimental effect on DOC performance due to the strong chemisorption of sulfur species on the catalyst surface [91], [168], [169]. Sulfur in the diesel aftertreatment system originates from the fuel itself and lubricating oils and its most abundant form after combustion is SO_2. In the presence of oxygen and water vapor, SO_2 can be further oxidized to undesired products such as SO_3 and H_2SO_4 [49], [50], [169], [170]. These potentially lead to the loss of surface area and catalyst component phase transformations and jeopardize the performance of further downstream aftertreatment catalysts [171]. Exposure to SO_2 forms numerous sulfur species that inhibit precious metal sites from carrying out oxidation reactions, which results in the suppression of DOC catalytic activity. However, the extent of sulfur poisoning impact depends on catalyst composition, i.e., active materials and oxide supports used. In terms of the precious metal used, Pd easily reacts with SO_2 to form stable $PdSO_4$ species [93], [110], [121], [172]. In the case Pt, weakly adsorbed S species, such as molecular SO_2 and sulfite (SO_3^{2-}) species, can form while $PtSO_4$ formation is unlikely [172]. Concerning the oxide supports used, they can be classified as sulfating (i.e., Al_2O_3, CeO_2) and non-sulfating supports (i.e., SiO_2): in the presence of SO_2, the sulfating supports react with SO_2 to create relatively stable sulfate species (SO_4^{2-}), while the reaction and formation of these species do not occur on non-sulfating supports [89]. Sulfur speciation on the catalyst surface can also vary based on reaction conditions, especially the presence of oxygen, adsorption temperature and the precious metal particle size [99], [101]. In bimetallic systems, the composition ratio also directly impacts sulfur speciation, and bimetallic formulations can exhibit resistance to poisoning as seen for Pt-Pd [48], [100] and Pt-Cu [173], [174]. In the case of Pt-Cu bimetallic catalysts, Liau et al. showed that addition of a small amount of Cu into Pt catalysts led to lower sulfur content on the catalyst surface and retained activity after sulfur poisoning [173]. For Cu-based catalysts, numerous studies have explored the sulfur speciation for selective reduction of NOx [175], [176]; for DOC applications, sulfur speciation depends on the oxidation state of Cu, temperature and the presence of O_2 and H_2O [177]. Most reports indicate that Cu ions can easily react with SO_2 to form $CuSO_4$ species that decompose at temperatures above 600 °C [178].

Regeneration treatments can potentially reverse the effects of sulfur poisoning and recover catalytic activity by inducing the decomposition of sulfur species from the catalyst surface [99], [100], [120], [179], [101], [103], [104], [107], [111], [112], [115], [118]. Typically, high temperatures (> 500 °C) and the presence of a reductant (i.e., H_2, CO, HCs) are used to decompose oxidized sulfur species on the catalyst surface. Generally, desorption of molecular SO_2 and SO_2 from the decomposition of sulfite species occurs between 100 and 300 °C while SO_2 desorption from the decomposition of surface and bulk sulfate species occurs above 600 °C [101]. As stated above, loss of active sites via $PdSO_4$ formation is the dominant inhibition pathway when Pd-based catalysts are exposed to sulfur. The final state of Pd after $PdSO_4$ decomposition depends on the regenerative atmosphere the catalyst is subjected to. According to Kinnunen et al., $PdSO_4$ decomposition under inert conditions occurs via a stepwise reaction as shown in Eq. 3.4 [121].

$$\text{PdSO}_4\text{ Decomposition: } PdSO_4 \rightarrow\ PdSO_3 + \frac{1}{2}O_2 \rightarrow Pd + SO_2 + \frac{1}{2}O_2 \qquad (3.4)$$

Other studies have hypothesized that under reductive treatments, $PdSO_4$ decomposes to Pd_xS due to the reaction between Pd and residual sulfur in the catalyst [120]. For bimetallic systems, the composition ratio also impacts the effectiveness of the regeneration treatment as seen for Pt-Pd and Pt-Cu [48], [173].

Here, we investigated the performance of a bimetallic PdCu catalyst in the presence of competitive adsorbates and its response to hydrothermal aging and sulfur poisoning. First, the NO resistance reported previously in these bimetallic systems was found to be a function of concentration – when enough NO is present in the reactant gas, inhibition is observed, but at low NO concentrations it is not. With monometallic Pd, the inhibition is observed in both low and high NO concentrations cases. Second, we explored the effects of reducing and not reducing the catalyst intermediately under wet conditions, to see if dry/intermediate reductions contributed to the high activity or resistance to NO inhibition observed previously. Apparently, CO oxidation activity over both Pd and PdCu catalyst does not suffer when water is added, and when no intermediate reduction is performed. We also assessed the catalytic activity after hydrothermal aging in the presence of competitive adsorbates. Both Pd and PdCu catalysts have similar activity after hydrothermal aging in the presence of NO, H_2O and toluene. The effects of SO_2 poisoning and regeneration on both CO oxidation and CO + NO co-oxidation were investigated for both the monometallic Pd/SiO_2 and the bimetallic PdCu/SiO_2. The small addition of Cu to the Pd-based DOC offered some resistance to SO_2 poisoning and led to a greater extent of regeneration under reducing conditions.

3.2 Methods

3.2.1 Catalyst Synthesis

A silica-supported monometallic Pd and an alloy PdCu catalyst with a 3:1 Pd:Cu atomic ratio were synthesized using the strong electrostatic adsorption (SEA) method reported by Jiao and Regalbuto [180]. The Pd catalyst had a 4% Pd loading and the 3:1 PdCu had 2.5% Pd and 0.5% Cu by weight. For the synthesis, 5 g of silica gel (Davisil 636, Millipore Sigma) were mixed with 45 mL of deionized water (18.2 M-Ω) and 4 mL of stock ammonium hydroxide solution. The palladium nitrate and copper nitrate precursor (TCI America) were dissolved in 5 mL of water, to which 4 mL of stock ammonium hydroxide solution were added. The solution of metal ammine nitrate precursors was added to silica under vigorous stirring. The mixture was stirred for 1 hour and the solids were separated from the liquid by vacuum filtration. The retentate was washed with 100 mL of water and then dried under ambient air pressure at 90 ˚C for 16 h. Portions of the dried solids were then treated for 4 hours under flowing air (100 cm^3 $min^{-1}g^{-1}$) in a tubular furnace at 700 ˚C with a heating rate of 5 ˚C/min.

3.2.2 Details of Hydrothermal Aging Testing

We performed multi component oxidation experiments (TPO – temperature programed oxidation) on the two synthesized powder catalysts using a plug flow reactor with the product gas CO, NO, CO_2, NO_2 and H_2O outlet concentrations measured using a FTIR (California Analytical Instrument 600 FTIR (SC)).

3.2.3 Details on Activity Tests

Various activity tests (Trials 1-4 below) were conducted with the catalysts. In Trials 1-3, the catalyst was diluted 1:1000 with silica gel (Davisil Grade 635 Silica gel, pore size 60 Å, 60-100 mesh) by repeated crushing and pelletizing processes, sieved to eliminate particles smaller than 106 μm, and loaded into the quartz reactor directly on top of a porous frit in the reactor chamber. Since the two catalysts have different metal loadings, dispersion-based particle size was used to load equal surface moles of each catalyst. 840 mg of diluted Pd and 1000 mg of diluted 3:1 PdCu result in 2.65 surface micromoles of catalyst loaded [164]. A gas manifold with electronic mass flow controllers was used to deliver reactant gases to the reactor, and the effluent as noted was analyzed by FTIR.

In all trials, the fresh catalyst was reduced with pure H_2 flowing at 20 cm^3 min^{-1} while being heated at 6 °C min^{-1} from room temperature (RT) to 250 °C and held for 45 min before cooling to room temperature (TPR – temperature programed reduction), before oxidation reactions were performed. The experimental parameters for each trial are as follows (Table 8-1 details feed and reactor reagent concentrations):

3.2.3.1 Trial 1

This is a series of three experiments runs with an intermediate TPR before each TPO. This is a repeat of experimental results previously published [164], with higher NO concentration and the addition of water. The final CO only TPO is performed to determine if any activity loss occurs between runs 1 and 3 from NO inhibition, or from repeated heat treatments. The feed composition was 12% O_2 (15 kPa), 0.6% CO (0.5 kPa), 400 ppm NO, and 1.2% H_2O (balance Ar and N_2). Water is injected using a syringe pump at a rate of 2 mL h^{-1} in all runs. In Trial 1, during the TPO, gasses are introduced with a gas hourly space velocity (GHSV) of 27,200 $hr^{-1}g\ Pd^{-1}$ (1200L $g^{-1}\ hr^{-1}$) and 23,000 $hr^{-1}g\ PdCu^{-1}$ (1030 L $g^{-1}\ hr^{-1}$).

3.2.3.2 Trial 2

This is a series of four TPO runs with only an initial TPR (no intermediate reduction treatments). The purpose of this experiment is to determine if the intermediate reductions contribute to observed activity [164]. This feed composition was 12% O_2 (15 kPa), 0.6% CO (0.5 kPa), 50 ppm NO, and 1.2% H_2O (balance Ar and N_2). Water is injected from a syringe pump at a rate of 2 mL h^{-1} in all runs. In Trial 2, during the TPO experiments, gasses are introduced with a gas hourly space velocity (GHSV) of 27,200 $hr^{-1}g\ Pd^{-1}$ (1200L $g^{-1}\ hr^{-1}$) and 23,000 $hr^{-1}g\ PdCu^{-1}$ (1030 L $g^{-1}\ hr^{-1}$) (same flowrates at Trial 1).

3.2.3.3 Trial 3

Hydrothermal aging: Prior to Trial 3 experiments, the undiluted catalysts were hydrothermally aged at 700 °C for 80 h in air (100 mL min^{-1}) and water (0.3 mL hr^{-1}) flow using a tubular furnace. Catalysts were then diluted as described above.

The hydrothermally aged catalyst underwent a series of 8 TPOs following an initial TPR, with no intermediate reductions. The total time on stream comes to ~50 h to complete these oxidation reactions, helping to further probe activity loss over time in these materials. Odd numbered TPOs (runs 1, 3, 5, and 7) contain only CO and O_2 (balance N_2 and Ar). Run 2 contains NO (200 ppm balance N_2). Run 4 contains NO as in run 2, but with the addition of water at a rate of 2 mL h^{-1}. Run 6 contains NO, water at a rate of 1 mL h^{-1} and toluene at a rate of 1 mL h^{-1}. Run 8 contains water and toluene at the same rates as run 6, but without NO present. TPO experiments were run at a gas hourly space velocity (GHSV) of 27,200 hr^{-1}g Pd^{-1} (1200L g^{-1} hr^{-1}) and 23,000 hr^{-1}g PdCu^{-1} (1030 L g^{-1} hr^{-1}) (same flowrates at Trial 1).

3.2.3.4 Trial 4

The catalysts used in this set of experiments are those that have been poisoned by SO_2 exposure, and subsequently regenerated. Here, 15 mg of active catalyst powder were diluted with 150 mg of cordierite, and a total flowrate of 300 sccm were used. The active material and diluent were sieved to achieve a mesh size range of 250-420 µm. The mixture of the active material and diluent was placed in a quartz tube and secured with quartz wool at each end. The sample was then installed inside a Thermo Scientific Lindberg/Blue tube furnace as part of a powder flow reactor system. Bronkhorst and MKS mass flow controllers were used to control feed gas flowrates. Type K thermocouples were placed at the catalyst inlet and outlet positions to measure temperature, and the inlet temperature was used to plot results. Outlet gas concentrations were monitored using MKS MultiGas 2030 FTIR Spectrometer gas analyzer and data was acquired at 1 Hz. To avoid sulfur deposition along reactor lines, stainless steel lines treated with sulfinert coating were purchased from Swagelok. Before all experiments, all samples were pretreated in 5% H_2 in N_2 at 300 °C for 45 minutes. Note, these experiments were done on a different reactor than those described above. After cooling down the samples to 50 °C under pretreatment conditions, the CO oxidation activity was evaluated, using the following TPO protocol: 0.5% CO and 10% O_2 in N_2 with a 5 °C/min ramp rate. For the CO + NO co-oxidation activity of the samples, 50 ppm of NO was added to the CO oxidation activity protocol.

Temperature Programmed Desorption

To estimate the temperature at which formed sulfur species on the catalysts decompose, the samples were first exposed to 30 ppm SO_2 and 10% O_2 in N_2 at 100 °C until SO_2 saturation was achieved after the H_2 pretreatment mentioned above. After the outlet SO_2 concentration reached the inlet 30 ppm concentration, the reactor was purged with N_2 at 100 °C to remove weakly adsorbed SO_2 from the sample and reactor lines until the SO_2 concentration recorded by the FTIR reached zero. Then, a temperature programmed desorption ramp was performed at a rate of 10 °C/min to 900 °C followed by an isothermal hold at 900 °C for 15 minutes.

Sulfur Regeneration

After SO_2 exposure at 100 °C, samples were exposed to a gas mixture of 5% H_2 in N_2, and a temperature ramp of 100 to 700 °C was performed. The temperature was then held at 700 °C for 45 minutes. Following this regeneration treatment, the sample was cooled to 100 °C in H_2 and the CO oxidation activity protocol was performed to assess if catalytic activity had recovered. To rule out if the regeneration treatment induced any further deactivation via sintering, the regeneration protocol was performed without the SO_2 adsorption step at 100 °C.

3.3 Results

3.3.1 Trial 1

Figure 3-1 shows the respective conversion as a function of temperature curves acquired for Pd (A) and PdCu (B) under trial 1 conditions. The results of Run 1 (green) are like those shown in previous publications, in terms of the conversion vs temperature shape and T_{50} acquired [164]. Since water was included in these conditions, but not in previous publications, this indicates water alone does not significantly affect CO oxidation performance under these conditions. Run 2 data (red) indicates that both Pd and PdCu are inhibited by the addition of NO, as seen by the shift in conversion values to higher temperatures. Previous work has shown that PdCu offers resistance to NO inhibition of CO oxidation activity at low NO concentrations (50 ppm). This means the NO inhibition resistance is a function of NO concentration for PdCu or that the addition of water compounds the NO inhibition effect. To determine if the result is from NO concentration or water, dry runs at high NO concentration are shown in Figure 8-1, and clearly show the inhibition effect is present, indicating NO inhibition resistance in PdCu is in fact a function of NO concentration. Repeat experiments conducted at 50 ppm NO are shown in Figure

8-2 to confirm PdCu does show inhibition free activity at low NO concentrations. Run 3 (blue) data indicates a loss of activity with repeated runs for Pd, but an apparent resistance to loss of activity for PdCu, at low temperatures. Figure 8-3 displays T_{50} results acquired for the Trial 1 experiments.

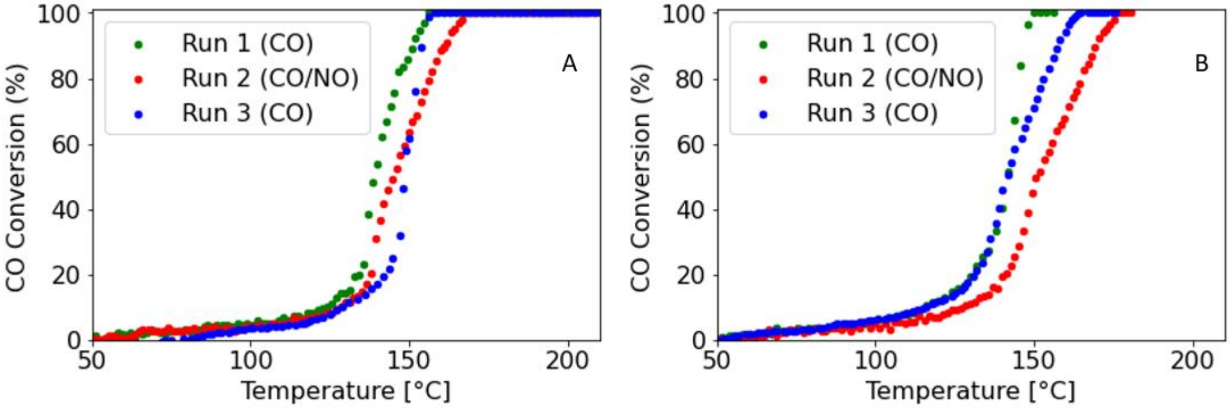

Figure 3-1 Conversion versus temperature for Pd/SiO_2 (A) and 3:1 PdCu/SiO_2 (B) under Trial 1 conditions. Run 1 (green) and 3 (blue) contain only CO and O_2. Run 2 (red) contains NO.

3.3.2 Trial 2

Figure 8-4 displays the conversion versus temperature results acquired for Trial 2 data on 8-4A Pd and 8-4B PdCu. The primary differences between Trial 1 and 2 are that Trial 2 contains lower NO concentration (50 ppm) and that no intermediate reductions take place. All four results sets for both catalysts are very similar in terms of temperature where the onset of conversion occurs, indicating the intermediate reduction step had little effect on activity. The T_{50}s shown in Figure 3-2 indicate Pd and PdCu have similar activity. However, we note that PdCu has an apparent loss of activity with more runs, whereas the Pd T_{50} decreases with increasing run numbers. The loss of activity for PdCu is not likely due to the addition of NO at this concentration, but rather from the repeated heat treatments, as discussed in Trial 1 proofs.

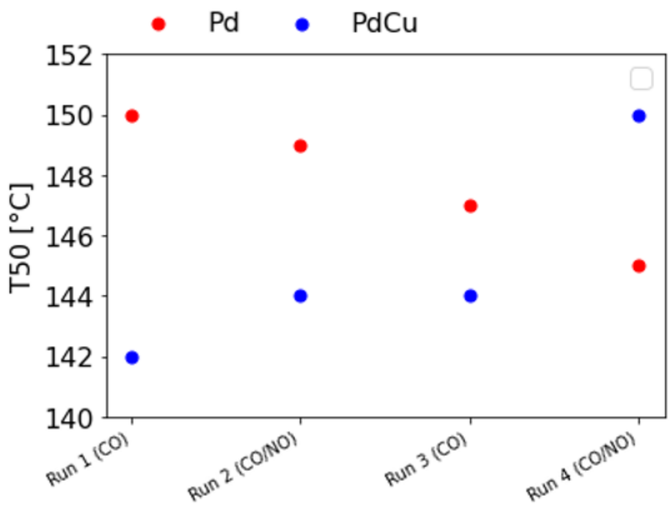

Figure 3-2 T_{50} values for Pd/SiO_2 (red) and 3:1 PdCu/SiO_2 (blue) under Trial 2 conditions.

3.3.3 Trial 3

T_{50} values acquired from the activity tests performed on the hydrothermally aged catalysts are shown in Figure 3-3 where Pd is shown in red (A) and PdCu in blue (B). The X-axis is labeled with the reactants included in each run. Conversion versus temperature results from which the T_{50}s were acquired are shown in Figure 8-5, (A) showing Pd and (B) showing PdCu results. The initial CO-only run for both catalysts is of comparable temperature to that acquired without hydrothermal aging. However, both catalysts also show an increase in T_{50} value as subsequent runs are performed. Run 6 for Pd (A) shows a strong inhibition effect when NO, water, and toluene is present in the system. The effect is less pronounced on the PdCu in run 6, but still significant. Further, PdCu appears to continually increase in T_{50} as more reactants are added, indicating activity falls with each run cycle. These results indicate the initial hydrogen reduction post hydrothermal aging has a positive effect on activity for both materials, but this effect is lost with each sequential run. The effect of additional reactants appears to be more pronounced for the Pd catalyst only in run 6, whereas all other runs are comparable.

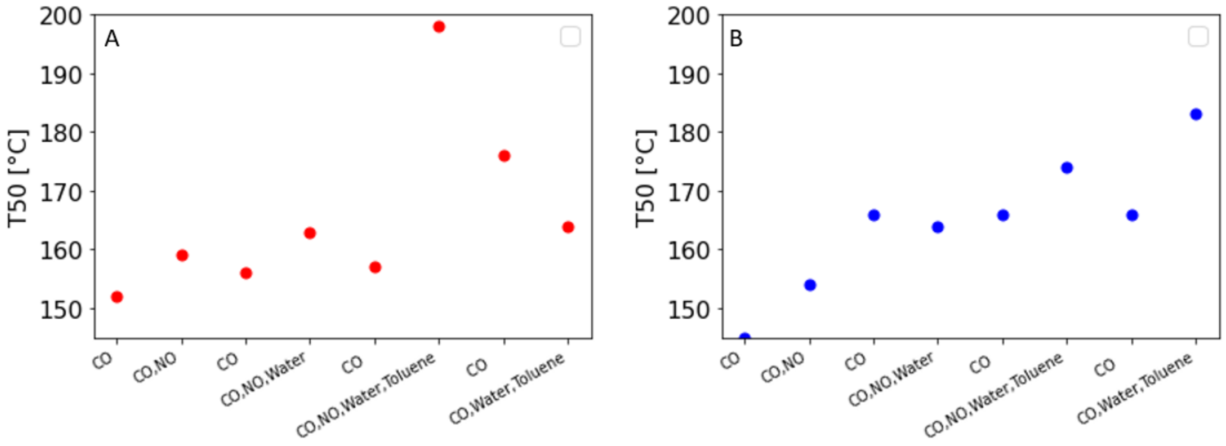

Figure 3-3 Temperatures at 50% conversion acquired for Pd/SiO_2 (A) and 3:1 PdCu/SiO_2 (B) under Trial 3 conditions.

3.3.4 Trial 4

Sulfur and Regeneration Study of Bimetallic PdCu Alloys

Baseline Activity before SO_2 exposure for CO and CO + NO co-oxidation

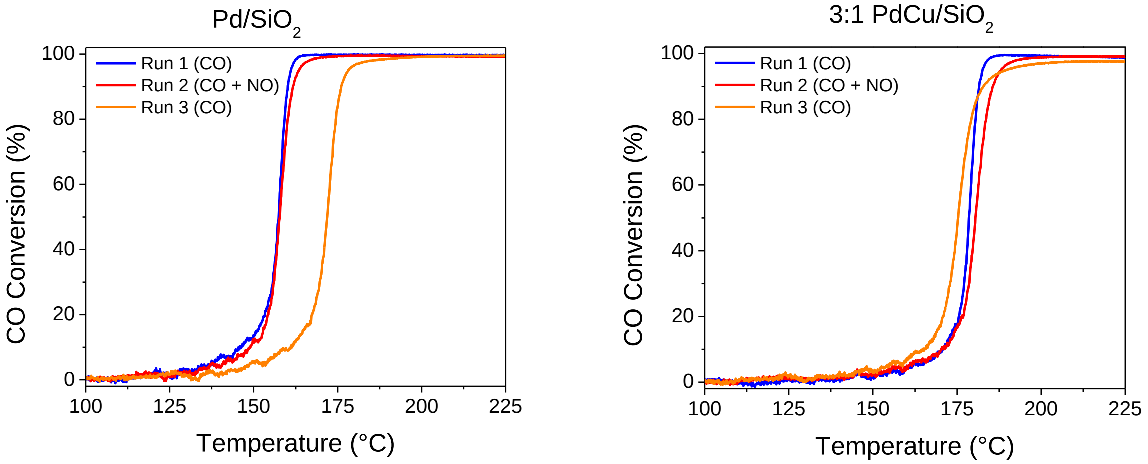

Figure 3-4 CO conversion using Pd/SiO_2 (left) and 3:1PdCu/SiO_2 (right). Runs 1 and 3 are under CO oxidation baseline conditions, 0.5% CO and 10% O_2 in N_2, while Run 2 includes 50 ppm NO with the CO oxidation baseline conditions.

To assess the effects of SO_2 on the catalytic activity of these samples, baseline activity experiments for CO and CO+NO co-oxidation were performed over the monometallic Pd/SiO_2 and bimetallic 3:1 PdCu/SiO_2 samples. Figure 3-4 shows the CO conversion as a function of temperature during a series of TPO tests over Pd/SiO_2 (left) and bimetallic 3:1 PdCu/SiO_2 (right). In the case of Pd/SiO_2, when 50 ppm of NO was introduced during Run 2, the CO conversion profile shifts to higher temperatures. Comparing the temperature at 50% conversion (T_{50}) for Run 1 and 2, a 14 °C difference was observed indicating that Pd/SiO_2 was susceptible to the inhibition caused by the presence of competitive adsorbates. The introduction of Cu substitution into the Pd catalyst led to an increased resistance in the presence of competitive adsorbates since the CO conversion profile under Run 2 conditions did not shift to higher temperature and matched the CO conversion profile during Run 1 and 3 conditions. This behavior has been predicted by DFT studies [162] and verified by experimental studies [163]. However, the T_{50} comparison between Pd/SiO_2 and bimetallic 3:1 PdCu/SiO_2 for CO oxidation (157 °C vs. 179 °C) and CO + NO co-oxidation (172 °C vs. 180°C) shows that the monometallic catalyst is more active for both reactions, although impacted by the addition of NO. This difference is attributed to the different weight loadings of the synthesized samples. Note, in the sulfur exposure experiments, the space velocity was not varied to account for the lower Pd loading, for consistency with prior SO_2 poisoning experiments [100], [179].

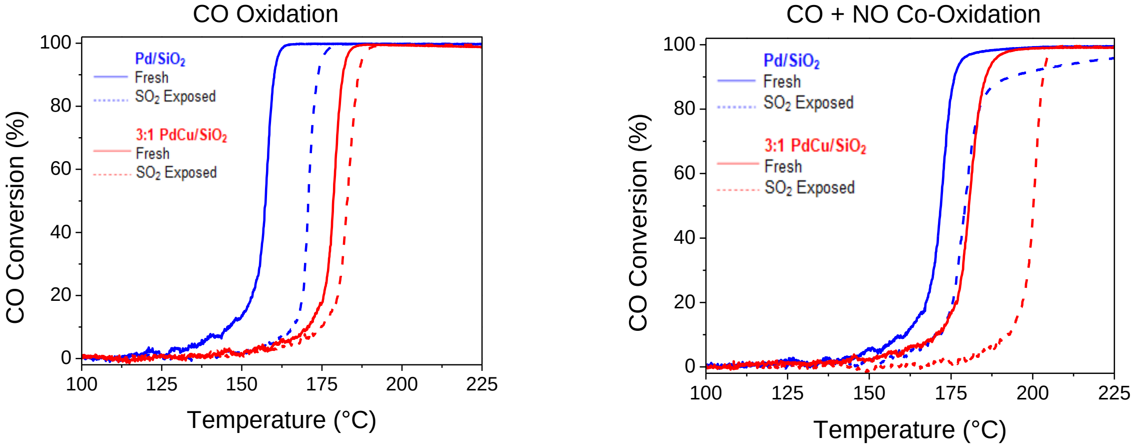

Figure 3-5 CO conversion before and after SO_2 exposure under CO oxidation (left) and CO + NO co-oxidation (right) conditions for Pd/SiO_2 and 3:1 PdCu/SiO_2. Fresh CO conversion profiles are depicted by solid lines, while SO_2-exposed CO conversion profiles are depicted by dashed lines.

After SO_2 exposure at 100 °C, the baseline activity experiments for CO oxidation and CO + NO co-oxidation reactions for the monometallic Pd/SiO_2 and bimetallic 3:1 PdCu/SiO_2 samples were run to evaluate the impact of SO_2 on the catalytic activity. The fresh (solid) and SO_2-exposed (dashed) CO conversion profiles under CO oxidation and CO + NO co-oxidation conditions are shown in Figure 3-5. The amount of SO_2 adsorbed during exposure at 100°C and the extent of inhibition based on the difference for T_{50} values for fresh and SO_2-exposed runs can be seen in Table 3-1.

Table 3-1 SO_2 adsorption quantification and changes in the T_{50} values due to SO_2 exposure at 100 °C

Catalyst	**SO_2 Adsorbed (μmol)**	**ΔT_{50} between Fresh and SO_2 Exposed for CO oxidation**	**ΔT_{50} between Fresh and SO_2 Exposed for CO + NO co-oxidation**
Pd/SiO_2	0.4	13	7
3:1 $PdCu/SiO_2$	0.3	4	20

Under CO oxidation conditions, SO_2 exposure shifted CO conversion profiles for both catalysts to higher temperatures, indicating that SO_2 did inhibit CO oxidation activity. However, the change in T_{50} between fresh and SO_2-exposed runs is higher for Pd/SiO_2 as shown in Table 3-1. Based on this difference, addition of Cu to Pd-based DOC catalysts offers resistance to the inhibiting effect of SO_2. This response has also been observed for addition of Cu to Pt-based catalysts [173].

In the case of the CO + NO co-oxidation reaction, CO conversion profiles for both catalysts also shifted to higher temperatures. Based on the difference of T_{50} values for fresh and SO_2-exposed samples shown in Table 3-1, the difference is higher on the bimetallic 3:1 $PdCu/SiO_2$ sample. However, the rate of change in CO conversion at higher temperatures is faster for the bimetallic sample compared to the monometallic sample. We speculate that at high temperatures, SO_2 inhibition could affect the formation of reaction intermediates on Pd/SiO_2 impeding the completion of the reaction.

Regarding the sulfur mass balance during the SO_2 including runs, Table 3-1 shows only the amount of SO_2 adsorbed during exposure at 100 °C since no SO_2 desorption was observed in the temperature range of these TPO tests. Neither were SO_3, COS, H_2S or H_2SO_4 detected during these TPO experiments. The bimetallic 3:1 PdCu/SiO_2 shows a lower amount of SO_2 adsorbed at 100 °C compared to the monometallic sample. A similar result has been observed with the addition of Cu to Pt-based catalysts due to interaction between Pt-Cu that alters the bonding strength of sulfur species [173].

TPD After SO_2 Exposure

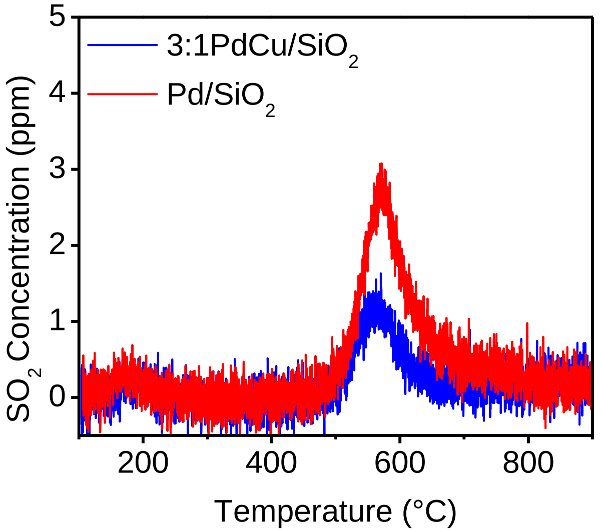

Figure 3-6 SO_2 desorption profiles during temperature program desorption study for Pd/SiO_2 (red) and 3:1 PdCu/SiO_2 (blue).

Before a regeneration protocol was designed for removal of sulfur species from the catalyst surface, some idea of when S species decompose and S desorbs needed to be explored. To assess this, a temperature programmed desorption study was performed after SO_2 exposure at 100 °C and the SO_2 desorption profiles for both monometallic Pd/SiO_2 (blue) and bimetallic 3:1 PdCu/SiO_2 (red) are shown in Figure 3-6. For the

Pd/SiO_2 sample, two SO_2 desorption peaks were observed during the temperature ramp. Based on the literature, the low temperature desorption peak (located at 173 °C) corresponds to the desorption of molecular SO_2 from the catalyst surface, most likely the SiO_2 support, while the high temperature desorption peak (located at ~560 °C) corresponds to SO_2 from the decomposition of $PdSO_4$ species from the catalyst surface as shown in Eq. 4 [121]. No high temperature sulfur species should be attributed to the SiO_2 support since it is non-sulfating support and does not react with SO_2 to create any sulfate species [89].

For the bimetallic 3:1 PdCu/SiO_2 sample, there are also two main SO_2 desorption regions: the low temperature peak (located at 173 °C) again should correspond to the desorption of molecular SO_2 from the catalyst surface, and the high temperature region (starting at 500 °C) corresponds to SO_2 from the decomposition of various sulfate species. The decomposition of $PdSO_4$ and $CuSO_4$ occur in this temperature range (> 600 °C); however, due to the bimetallic nature of this catalyst, the existence of Pd-rich, Cu-rich, and alloyed regions are possible and vary depending on the temperature and operating conditions. We speculate that the SO_2 desorption that occurs at these higher temperatures are from the decomposition of sulfate species from the Pd and Cu, but the distribution is unknown. Based on the SO_2 profiles for both catalysts, most of the sulfur species on the catalyst surface have desorbed by 700 °C; therefore, 700 °C was chosen as the regeneration protocol temperature.

Sulfur dioxide desorption peaks and the sulfur mass balance for control experiments, i.e., the same protocol run with an empty tube, the SiO_2 support and the cordierite diluent are shown in Figure 8-6 and Table 8-2, respectively. For all control experiments, there is a small SO_2 desorption peak at 569 °C.

Catalyst Regeneration

Typically, catalyst regeneration protocols after sulfur poisoning involve high temperatures (> 500 °C) to induce sulfur species decomposition but can also include the presence of a reductant (I.e., H_2, CO, CH_4) as these often lead to lower temperatures for decomposition of sulfate species. Literature results have shown that regeneration treatments in reductive environments not only decompose a higher amount of sulfur species, but also provide higher catalytic activity recovery compared to other conditions [100], [107], [118]. Based on the TPD results mentioned above and literature results, a regeneration temperature of 700 °C and the presence of H_2 were selected as the regeneration conditions to test whether the decomposition of sulfur species would lead to recovered oxidation performance. Figure 3-7 shows CO conversion profiles for fresh (green), SO_2-exposed (red), and H_2-regenerated (blue) under CO oxidation (left panel) and CO + NO co-oxidation (right panel) conditions for both catalysts.

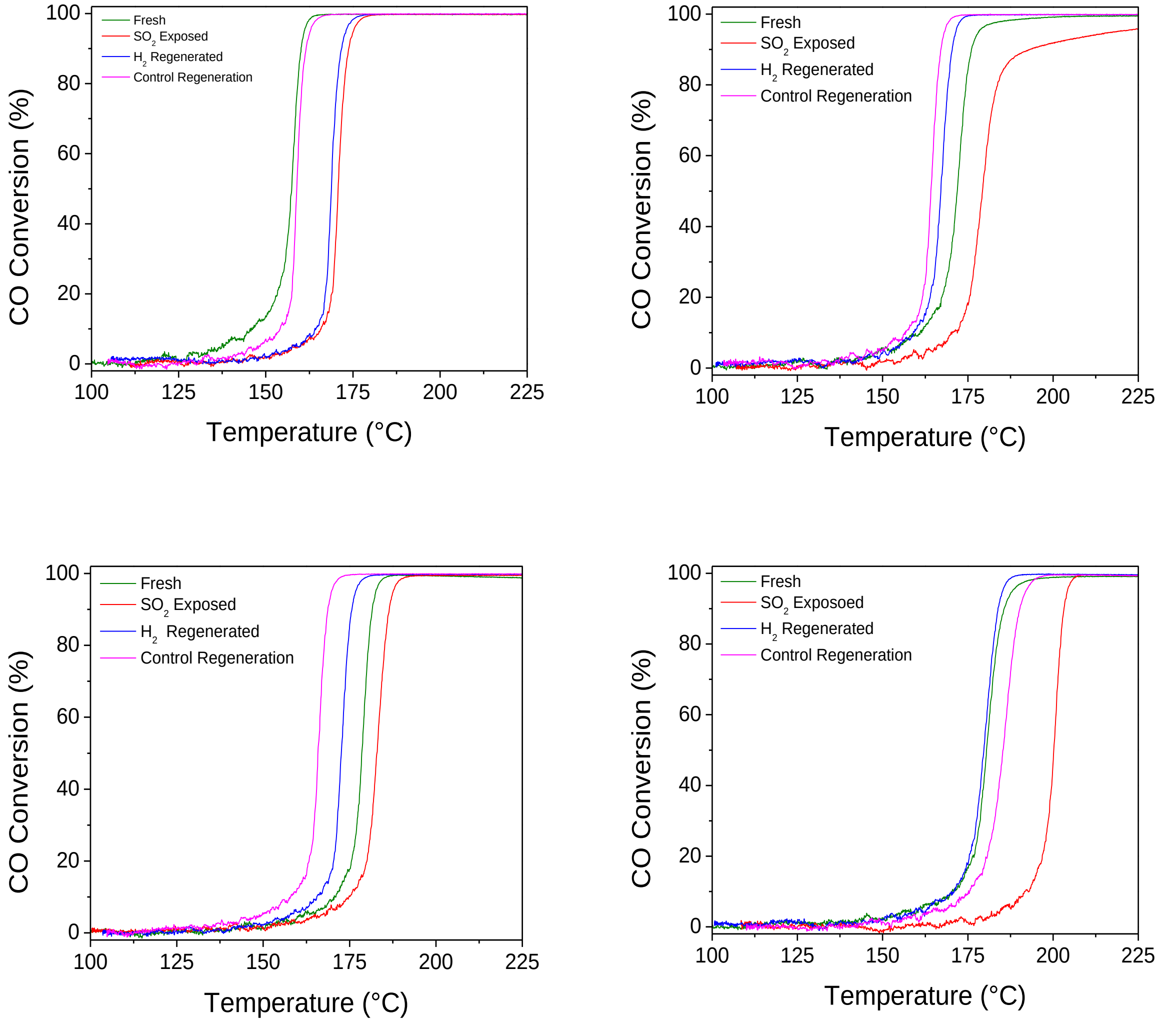

Figure 3-7 Comparison of the CO conversion during CO oxidation (left) and CO + NO co-oxidation (right) using fresh (green), SO_2-exposed (red) and H_2-regenerated (blue) Pd/SiO_2 (top panel) and 3:1PdCu/SiO_2 (bottom panel) samples. To verify that the regeneration protocol did not induce further deactivation, the samples were subjected to the same regeneration protocol in the absence of SO_2 adsorption at 100 °C and the control (magenta) CO conversion profiles as a function of temperature are also shown.

For CO oxidation conditions, the regeneration treatment at 700 °C successfully recovered and enhanced the catalytic activity of the bimetallic 3:1 PdCu/SiO_2 sample - the CO conversion as a function of temperature profile of the regenerated catalyst shifted to lower temperatures compared to even that of the fresh conversion profile. In the case of the monometallic Pd/SiO_2 sample, the regeneration treatment did not recover any CO oxidation activity, the regenerated CO conversion as a function of temperature profile matches the conversion profile of the SO_2-exposed sample. The difference in the activity recovery of these samples suggests that the addition of Cu offers some resistance to SO_2 as previously stated. It also indicates that the Cu addition favors the decomposition of $PdSO_4$ species, which leads to improved CO oxidation activity. On the other hand, the monometallic sample is more susceptible to SO_2 poisoning and the regeneration conditions were not sufficient to decompose the $PdSO_4$ species on the catalyst surface as shown in the SO_2 TPD results. To demonstrate that the regeneration treatment did not induce any other modes of deactivation (i.e., sintering), the regeneration protocol was performed in the absence of SO_2, and the control (magenta) CO conversion as a function of temperature profiles are featured in Figure 3-7 for both the monometallic Pd/SiO_2 and bimetallic 3:1 PdCu/SiO_2 samples. For CO oxidation conditions, the control regeneration protocol did not induce further deactivation for either sample. However, in the case of the bimetallic sample, the H_2 regeneration protocol improved the CO oxidation activity, explaining the improvement observed post SO_2 exposure and regeneration.

For CO + NO co-oxidation conditions, the regeneration treatment in H_2 at 700 °C led to recovery of catalytic activity for both samples. Based on the oxidation results after sulfur poisoning shown in Figure 3-7, the presence of NO as a competitive adsorbate led to further deactivation, potentially indicating a more challenging recovery process. For both samples, the regenerated CO conversion profiles match the fresh sample suggesting that the effects sulfur poisoning can be reversed. The control CO conversion profiles also match the fresh profile suggesting that the regeneration protocol again did not induce further deactivation.

Regarding sulfur mass balances, since no SO_3, COS, or H_2SO_4 were detected during the regeneration and baseline activity temperature ramps and we are unable to measure H_2S, mass balances were not realized. However, since the regenerated and fresh CO conversion profiles match on the bimetallic sample, the regeneration treatment successfully decomposes sulfur species on the catalyst surface that influenced activity. In the case of the monometallic sample, the regeneration protocol successfully recovered all activity under CO + NO co-oxidation conditions but did not for CO conditions.

Altogether, the addition of Cu to Pd-based DOCs does offer some resistance to SO_2 poisoning based on the lower amount of SO_2 adsorbed during the SO_2 exposure part of the TPD experiments, compared to the SO_2 adsorbed on the monometallic sample. Plus, the regeneration protocol under reducing conditions can reverse the effects of SO_2 poisoning for both CO oxidation and CO+NO co-oxidation conditions. Even though the effects of SO_2 exposure led the CO conversion profile shift to higher temperature under CO+NO co-oxidation conditions, the benefits of Cu addition on catalytic activity in the presence of competitive adsorbates were recovered after the regeneration treatment. Ultimately, as shown in previous literature studies, the addition of Cu to Pd-based DOCs not only amplifies their improved resistance in the presence of competitive adsorbates but also proves instrumental in mitigating the effects of SO_2 poisoning and facilitating regeneration.

3.4 Conclusions

The effects of hydrothermal aging and sulfur poisoning were investigated for a bimetallic PdCu catalyst in the absence and presence of competitive adsorbates. Further investigation into NO resistance of bimetallic PdCu catalyst revealed its dependency on the NO concentration. The CO oxidation activity for the monometallic Pd and bimetallic PdCu catalysts remains unaffected in the presence of water, both with no intermediate reduction and after hydrothermal aging in the presence of NO, H_2O, and toluene. The effects of SO_2 poisoning and regeneration on both CO oxidation and CO + NO co-oxidation were assessed for both the monometallic Pd/SiO_2 and the bimetallic PdCu/SiO_2. The small addition of Cu to the Pd-based DOC offered some resistance to SO_2 poisoning and led to a greater extent of regeneration under reducing conditions.

4. SO_2 Interactions with Hydrothermally Treated Pd-based Catalysts: Influence of Exposed Number of Metal Sites on SO_2 Poisoning

4.1 Introduction

As vehicular emission standards become increasingly stringent, there is a growing demand for the development of more active and stable aftertreatment oxidation catalysts. Also known as 'The 150 °C Challenge', this US Department of Energy initiative aims for new catalyst developments to achieve 90% conversion of emissions by 150 °C [53]. Current aftertreatment oxidation catalysts in diesel engines are responsible for the conversion of unburned hydrocarbons, CO and NOx emissions found in the exhaust [17], [181]. These catalysts are composed of (ideally) small nanoparticles of precious metals (Pt, Pd) supported on Al_2O_3 with the incorporation of various additives for oxygen storage and thermal stability.

However, for new formulations of oxidation catalysts to be considered for further development and vehicular implementation, they must meet emission control standards set by the US Environmental Protection Agency over a useful life of 150,000 miles or 15 years whichever occurs first [8]. To assess the durability and activity over their operational lifetime in a laboratory setting, new formulations of oxidation catalysts must be exposed to high temperatures (> 700 °C) in the presence of high levels of H_2O (5%), CO_2 (5%) and O_2 (10%) [182], [183]. Studying the aged state of the catalyst is crucial for development, as sintering or thermal deactivation is a main cause of loss of catalytic activity. The agglomeration of the active and support materials of the catalyst occurs at high temperatures (> 500 °C) and is accelerated by the presence of water vapor [38], [184]–[186]. The two main sintering mechanisms are Ostwald ripening and particle migration. Ostwald ripening involves the growth of large particles through the transport of mobile species from small particles. In particle migration, nanoparticles coalesce when in proximity to each other. While the precious metal and support used do influence sintering rates, the precious metal particle size [187], gas composition [188]–[190] and temperature have the most significant impact on the sintering rates. Generally, the first phase of the sintering process is the growth of larger particles at the expense of the smallest particles through Ostwald ripening. As particles increase in size, they tend to coalesce when in proximity, but the sintering rate slows down due to the increased interparticle distance.

In addition to studying the effects of deactivation caused by exposure to high temperatures, it is crucial to investigate the sulfur resistance of new oxidation catalyst formulations. Small quantities of sulfur found in both the fuel and lubricating oils causes chemical deactivation of these catalysts due to the strong adsorption of sulfur on the active and support components [54], [91], [168], [169]. Due to the detrimental effect of sulfur on catalyst performance and its contribution to air pollution, the US Environmental Protection Agency has limited the sulfur content in diesel fuel to a maximum of 15 ppm [8]. While various sulfur species may be present in the exhaust, the main form of sulfur derived from fuel is sulfur dioxide (SO_2). In the presence of oxygen and water, SO_2 can be further oxidized to SO_3 and H_2SO_4 on the oxidation catalyst [49], [50]. These undesired products could induce irreversible changes to the structure of the catalyst and potentially affect the performance of subsequent downstream aftertreatment catalysts [191]. Exposure to SO_2 leads to the formation of different sulfur species on the catalyst surface, which depends on the catalyst composition (precious metal and support used) [89], [90], [94], [100], [101], [192]. In most cases, these sulfur species accumulate on the surface and inhibit oxidation reaction pathways from occurring at the active site and/or metal-support interface [91], [95]. Furthermore, sulfur speciation on the catalyst surface is influenced by reaction conditions [94], [97], [115] and precious metal particle size [99], [101]. According to Wilburn et al., the exposed number of metal sites on Pt- and Pd-based catalysts supported on γ-Al_2O_3 significantly impacts the amount of SO_2 adsorbed and desorbed during temperature programmed desorption (TPD) experiments, as well as the nature of sulfur species formed on the catalyst surface when exposed to SO_2. Typically, catalysts with a high number of exposed metal sites form a greater amount of high temperature sulfur species (i.e., surface and bulk $Al_2(SO_4)_3$), while catalysts with a low number of exposed metal sites form a greater amount of low temperature sulfur species (i.e., molecular SO_2 and $Al_2(SO_3)$). Plus, the amount of SO_2 adsorbed and desorbed during the TPD ramp decreased with decreasing number of exposed metal sites [99]. In the case of CeO_2-based catalysts, sulfur poisoning primary leads to the loss of oxygen storage capacity ($Ce^{4+} \leftrightarrow Ce^{3+}$ interconversion) [26], [95], [117]. This occurs due to reaction between CeO_2 and SO_2 to form stable sulfate ($Ce_2(SO_4)_3$) species that block oxygen transfer [193]. However, to the best of our knowledge, there is a lack of comparable studies exploring the impact of the number of exposed metal sites on sulfur speciation for CeO_2-based catalysts, unlike the extensive research conducted on alumina-supported catalysts.

In both thermal and chemical deactivation, the extent of deactivation is influenced by the precious metal particle size. In this study, to avoid particle size heterogeneity, we synthesized uniform Pd nanoparticles with two particle sizes (3.4 nm and 13.1 nm) and deposited them onto supports relevant to aftertreatment applications, Al_2O_3 and CeO_2.

We then further investigated the effects of exposed number of metal sites and the influence of aging protocols (hydrothermal vs. thermal) on sulfur adsorption and release during temperature programmed desorption studies. The gas composition of aging protocols (hydrothermal vs. thermal) and exposed number of metal sites do influence sulfur speciation for both Al_2O_3-supported catalysts. In the case of CeO_2-supported catalysts, exposed number of metal sites does not lead to changes in sulfur speciation. CO pulse injection measurements evaluate the changes in exposed number of metal sites that occurred during aging and show that catalysts with a large number of exposed metal sites are more susceptible to sintering compared to catalysts with a low number of exposed metal sites. Even though aging does affect CO oxidation activity for catalysts with a larger number of exposed metal sites, they exhibit higher resistance to sulfur poisoning. Conversely, the catalysts with a smaller number of exposed metal sites experience the opposite effect.

4.2 Experimental Methods

Note: The synthesis of unsupported Pd nanoparticles and supported catalysts and TEM characterization was performed by Dr. Grayson Johnson.

4.2.1 Materials

Palladium (II) acetylacetonate ($Pd(acac)_2$, 99% technical grade), 1-octadecene (1-ODE, 90% technical grade), trioctylphosphine (TOP, 90% technical grade and 97% technical grade), 1-oleylamine (OAm, 70% technical grade), oleic acid (OAc, 90% technical grade), 1-tetradecene (TDE, 97% technical grade), 1-dodecene (DDE, 95% technical grade), the Al_2O_3 support (pore size 58 Å, ~ 150 mesh) and the CeO_2 support (nanopowder, < 25 nm particle size) were purchased from Sigma-Aldrich. Isopropanol (IPA, ACS Grade), toluene (Certified ACS), tetrahydrofuran (ACS Reagent, 99.0%) and hexanes (Certified ACS) were purchased from Fisher Chemical.

4.2.2 Synthesis of Small Pd Nanoparticles

The synthesis was based on J. Willis et al. [194] A mix of 0.5 mmol $Pd(acac)_2$ in 11 mL DDE, 9 mL TDE, and 5 mL OAm was degassed under vacuum for 15 minutes at room temperature. Then, the atmosphere was switched to Ar and 1.25 mL TOP (90% technical grade) was injected. This solution was returned to vacuum and heated to 50 °C for 30 minutes. A clear, pale yellow solution was obtained. Next, the atmosphere was returned to Ar, and the temperature was rapidly increased to 230 °C (rate of 20°C/min achieved) at which the reaction proceeded for 15 minutes. Compressed air was used to cool the reaction vessel to 170 °C and was followed by submerging the vessel in a water bath. Excess IPA was used to precipitate the nanoparticles out of solution, and this product was centrifuged at 6000 RPM for 10 minutes. The pelleted nanoparticles were redispersed in 10 mL of hexane with 50 µL of OAm added to improve particle stability. The precipitation/redispersion procedure was repeated for a total of three washes.

4.2.3 Synthesis of Large Pd Nanoparticles

This synthesis was based on L. Wu *et al*. [195] The mixture of 0.25 mmol $Pd(acac)_2$ in 4.5 mL 1-ODE was stirred under Ar for 15 minutes. Next, 0.56 mL of TOP (97% technical grade) and 5 mL of OAc were injected into this mixture. The temperature was raised to 60°C under continuous Ar flow for an hour to further degas the solvent and a clear, pale yellow solution was obtained. The reaction temperature was then raised to 280 °C at a rate of 15 °C/min. The reaction proceeded for 30 minutes before cooling naturally to room temperature. An identical washing procedure was used as that for the small particles.

Initial TEM images showed a few smaller particles mixed with the larger ones, so a size selective procedure was used to improve the product quality. This was achieved by adding just enough IPA to see the solution turn turbid and centrifuging at 6000 RPM for 5 minutes. The slightly colored liquid phase containing the smallest particles that failed to precipitate was discarded and the pellet was redispersed in hexanes with a drop of OAm. The size selection procedure was performed twice.

4.2.4 Preparation of Supported Catalysts

The preparation of the supported catalysts on Al_2O_3 (calcined at 900 °C for 24 h prior to use) and CeO_2 followed the procedure described in Cargnello et. al. [196] One gram of the support was added to 50 mL of toluene, and the remaining dispersion was sonicated for 5 minutes. A solution of the Pd NPs (with a volume that corresponds to 0.5 wt%) was prepared by diluting the NPs in 10 mL tetrahydrofuran. This solution was quickly added to the solution containing the support and was rapidly stirred for 5 minutes. The support became dark, and the remaining solution was colorless. The powder was recovered by centrifugation at 6000 RPM for 5 minutes, washed once with tetrahydrofuran, and recovered by centrifugation at 6000 RPM for 5 minutes. The remaining powder was then dried in a Thermo Scientific Linberg/Blue M Moldatherm Box furnace at 110 °C for 24 hrs. To remove any remaining organic ligands, the sample was thermally treated at 700 °C for 30 seconds.

4.2.5 Material Characterization

Transmission electron microscopy (TEM) images were collected on a FEI Titan and operated at 300 kV. Particle size distribution of the unsupported Pd nanoparticles (n= 45 particles) was performed using ImageJ. Powder X-ray diffraction (XRD) profiles of the supported catalysts were collected on Empyrean Multipurpose X-Ray Diffractometer with Cu Kα radiation (λ = 1.54 Å).

4.2.6 Catalytic Activity Measurements

For the CO oxidation activity and sulfur poisoning experiments, 15 mg of catalyst powder were diluted with 150 mg of cordierite, and a total flowrate of 300 sccm were used. The active material and diluent were sieved to achieve a mesh size range of 250-420 µm. The mixture of the active material and diluent was placed in a quartz tube and secured with quartz wool at each end. The sample was then installed inside a Thermo Scientific Lindberg/Blue tube furnace as part of a powder flow reactor system. Bronkhorst and MKS mass flow controllers were used to control feed gas flowrates. Type K thermocouples were placed at the catalyst inlet and outlet positions to measure temperature, and the inlet temperature was used to plot the results. The gas mixtures used in this study were formulated using gas cylinders purchased by Linde. Outlet gas concentrations were monitored using a MKS MultiGas 2030 FTIR Spectrometer gas analyzer and data was acquired at 1 Hz. To minimize sulfur deposition along reactor lines, stainless steel lines treated with sulfinert coating were purchased from Swagelok. Before all experiments, all samples were pretreated in 10% O_2 in N_2 at 300 °C for 45 minutes. Hydrothermally aged catalysts were prepared from the fresh catalysts by exposing them to 10% H_2O in N_2 at 700 °C for 25 hours, while thermally aged catalysts were exposed to N_2 at 700 °C for 25 hours.

CO Oxidation Activity Measurements

After cooling the sample to 100 °C under pretreatment conditions, the CO oxidation activity measurement was performed using a temperature programmed reaction protocol with a temperature ramp of 5 °C/min and a gas composition of 5000 ppm of CO and 10% O_2 in a N_2 balance.

Sulfur Poisoning

To assess the effects of SO_2 exposure on the CO oxidation activity of the fresh, hydrothermally aged, and thermally aged samples, the samples were exposed to 30 ppm of SO_2 and 10% O_2 in a N_2 balance at 100 °C after pretreating and cooling the sample under pretreatment conditions. Once the SO_2 outlet concentration recorded on the FTIR reached the inlet composition, a N_2 purge was introduced to remove any weakly adsorbed sulfur species from the catalyst surface. Once the SO_2 outlet concentration reached near zero, the CO oxidation activity measurement was again performed.

Temperature Programmed Desorption

To assess what type of sulfur species formed on the catalyst surface, once the sample was exposed to SO_2 at 100 °C as the sulfur poisoning protocol mentioned above, a temperature programmed desorption ramp in N_2 was performed at a rate of 10 °C/min to 900 °C followed by an isothermal hold at 900 °C for 15 minutes.

CO Pulse Injection Measurements

Note: CO pulse injection measurements were performed by Dr. Zhuoran Gan.

For the CO pulse injection measurements, 50 mg of catalyst sample (mesh size range of 250-420 µm) was first treated with 10% O_2 in Ar balance with a flowrate of 100 sccm at 100 °C for 5 minutes; then it was heated to 400 °C under 5% H_2 in an Ar balance with a flowrate of 50 sccm for 30 minutes. After the reducing pretreatment, the sample was purged with 50 sccm Ar for another 30 minutes and then cooled under these conditions to 35 °C. At this temperature, doses of CO were injected into the reactor using a VICI four-way valve controlled by NI LabVIEW software. The valve was periodically switched between a feed of 20 sccm of 0.5% CO in Ar balance for 5 seconds and 20 sccm Ar for 20 seconds. The reactor outlet concentrations, represented as monitored masses (18 for H_2O, 28 for CO, 36 for Ar, and 44 for CO_2), were recorded using a Hiden HPR-20 Mass Spectrometer. No formation of CO_2 or H_2O was observed during the CO pulses. The sample was saturated once the concentration of the CO peaks was unchanged with additional pulses. To calculate the CO uptake, the peak area difference was used between the saturated peaks and the unsaturated peaks. All CO pulse measurements were performed three times on each sample to check repeatability. The particle size for spherical-shaped nanoparticles was calculated using Eq. 4.1, where ρ_{Pd} is the density of Pd and active metal surface area (SA) was calculated from CO uptake.

$$d_{particle} = \frac{6}{\rho_{Pd} * SA} \tag{4.1}$$

4.3 Results and Discussion

4.3.1 Characterization of colloidal nanoparticle catalysts

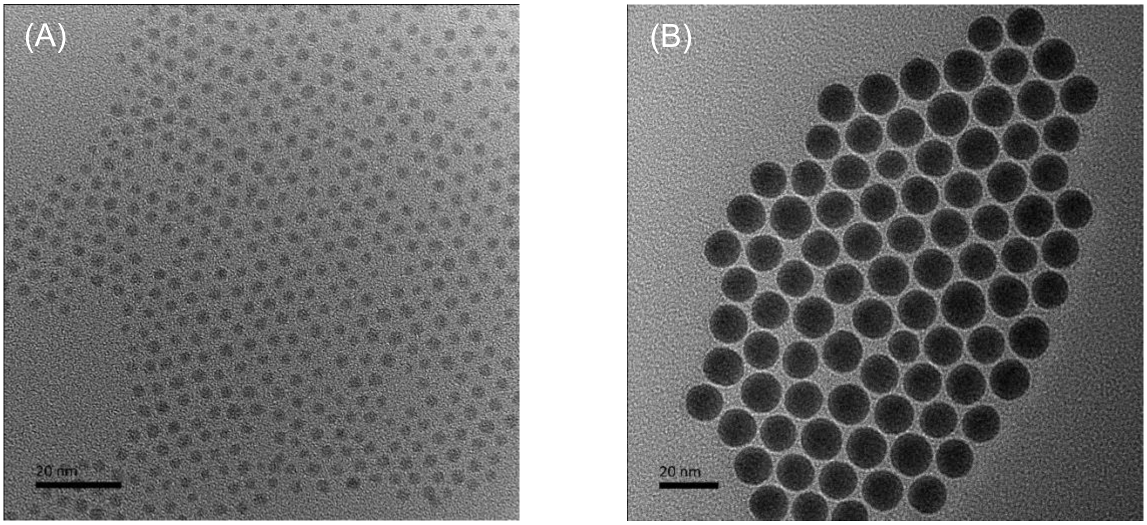

Pd/Al$_2$O$_3$ – Small

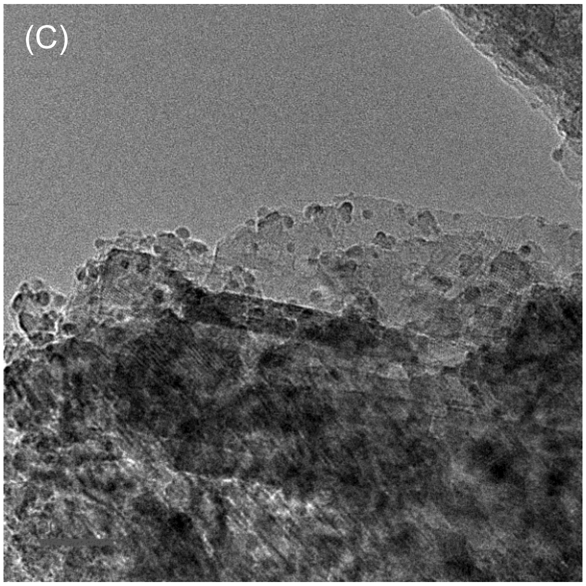

Pd/Al$_2$O$_3$ – Large

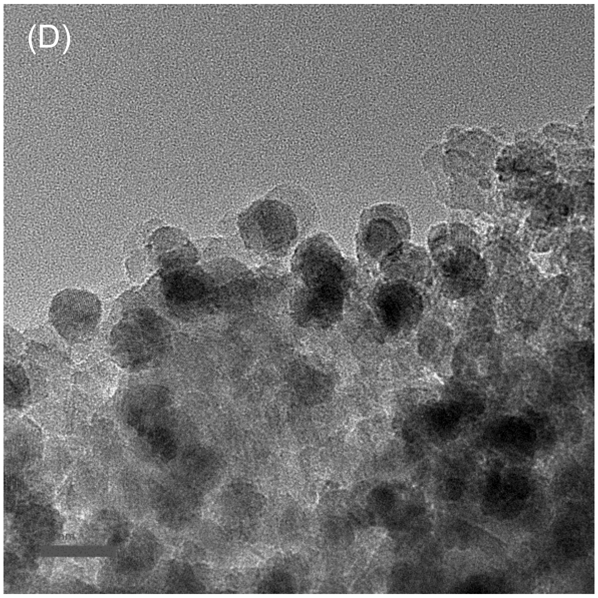

Pd/CeO$_2$– Small

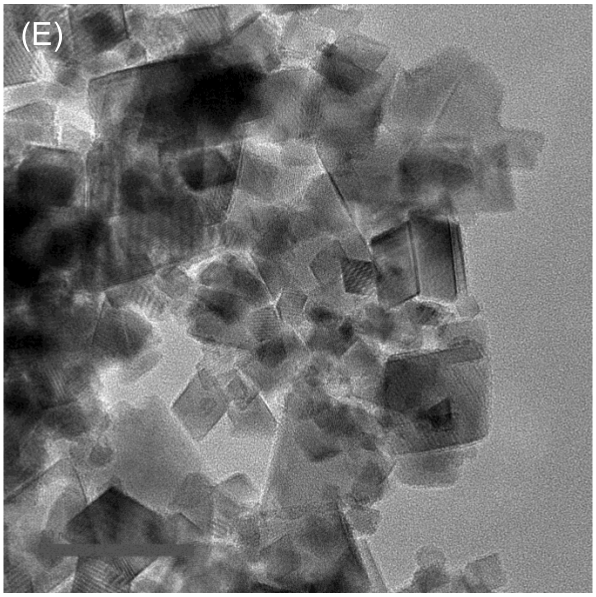

Pd/CeO$_2$ – Large

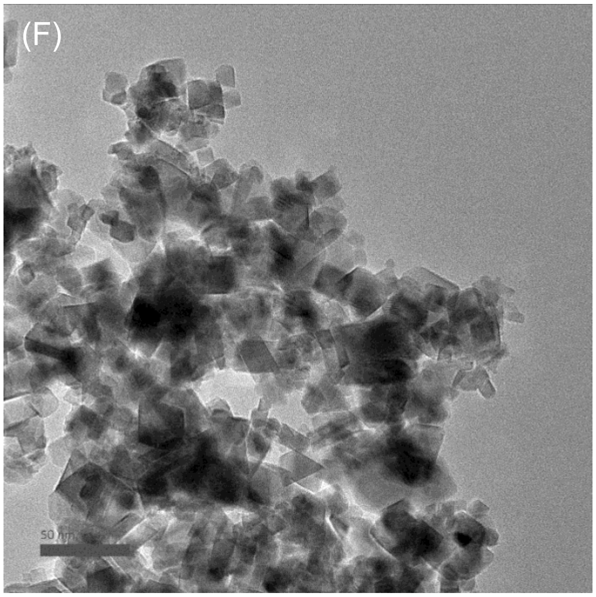

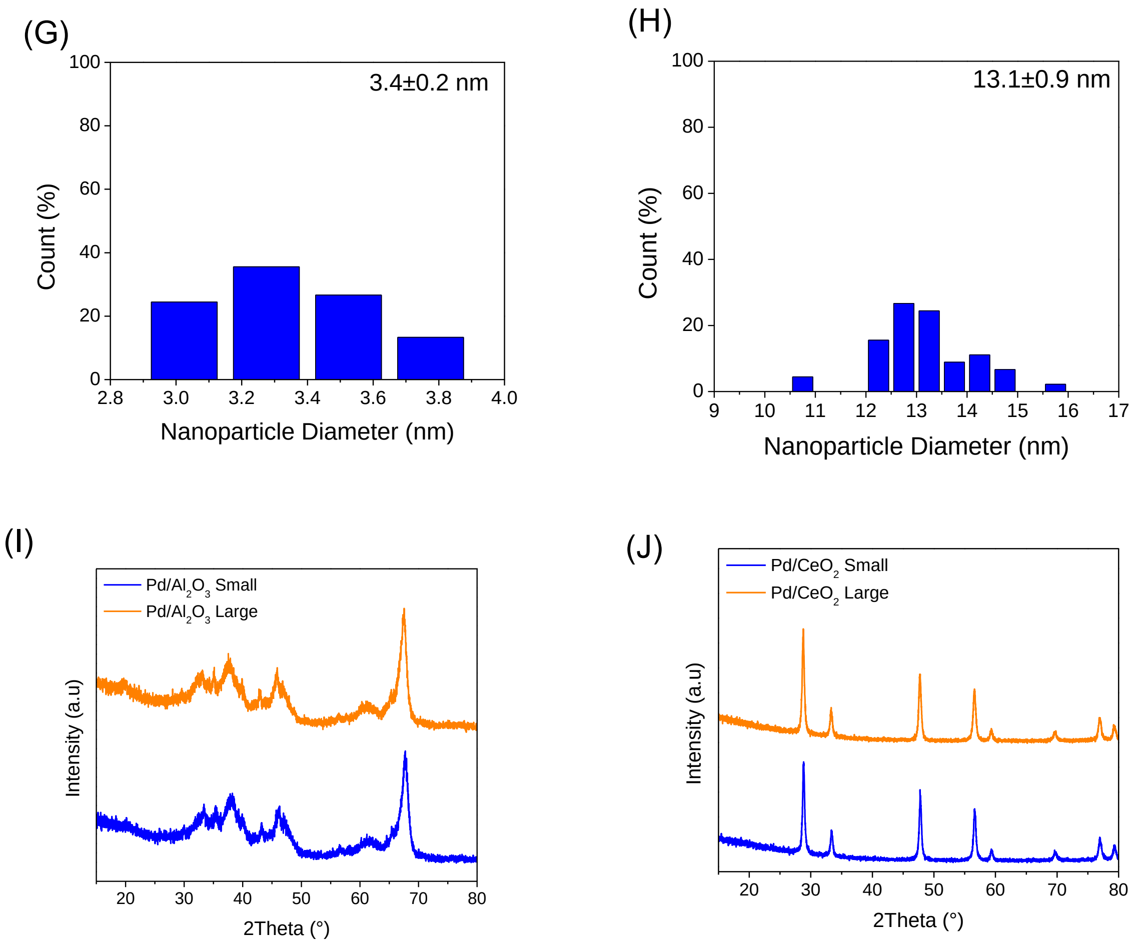

Figure 4-1 Ex situ TEM images of the (A, B) colloidal Pd nanoparticles and (C, D) nanoparticles supported on Al$_2$O$_3$, and (E, F) nanoparticles supported on CeO$_2$. (G, H) Particle size distribution of the unsupported Pd nanoparticles (n = 45 particles). (I) XRD profiles for fresh Pd/Al$_2$O$_3$ Small (dark blue) and Pd/Al$_2$O$_3$ Large (orange). (J) XRD profiles for fresh Pd/CeO$_2$ Small (dark blue) and Pd/CeO$_2$ Large (orange).

Uniform Pd nanoparticles of two sizes (3.4 nm and 13.1 nm) were synthesized following the literature protocols described above. Ex situ transmission electron microscopy images were collected to verify the size selectivity of the nanoparticles and are shown in Figure 4-1A, B. Based on the particle size distribution shown in Figure 4-1G, H, the average particle size of the small unsupported Pd nanoparticles is 3.4 nm with a standard deviation of 0.2 nm. The average particle size of the large unsupported Pd nanoparticles is 13.1 nm with a standard deviation of 0.9 nm. Once the shape and size selectivity had been confirmed, the nanoparticles were then deposited onto the γ-Al_2O_3 and CeO_2 supports with a weight loading of 0.5%. Henceforth, we designated the samples as Pd/support Small and Pd/support Large, aligning with the respective particle sizes of 3.4 nm and 13.1 nm. TEM images were collected after the addition of the γ-Al_2O_3 support and after the removal of the organic linkers at 700 °C for 30 seconds (Figure 4-1C, D) and the size and shape selectivity remained intact after these procedures. Figure 4-1I shows the XRD profiles of the fresh Pd/Al_2O_3 Small and Pd/Al_2O_3 Large samples. Only the diffraction patterns of the γ-Al_2O_3 support can be observed, while minimal to no detection of metallic Pd or PdO can be detected due to the low Pd weight loading. TEM images were collected after the addition of the CeO_2 support and after the removal of the organic linkers at 700 °C for 30 seconds (Figure 4-1E, F); however, it is difficult to detect the presence of Pd nanoparticles on the support. Figure 4-1J shows the XRD profiles of the fresh Pd/CeO_2 Small and Pd/CeO_2 Large samples. Only the diffraction patterns of the CeO_2 support can be observed. Similar to the Pd/Al_2O_3 results, minimal to no detection for PdO or metallic Pd was observed. The use of catalysts with uniform particle size will eliminate the effects of particle heterogeneity on sulfur speciation.

4.3.2 Pd/Al_2O_3 TPD after SO_2 Exposure

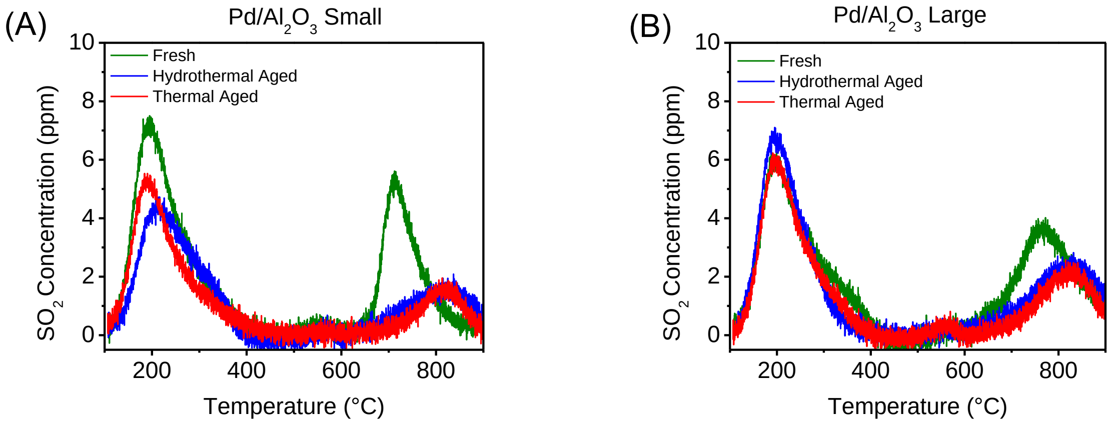

Figure 4-2 SO_2 desorption profiles for fresh (green), hydrothermally-aged (blue) and thermally-aged (red) (A) Pd/Al_2O_3 Small and (B) Pd/Al_2O_3 Large during the TPD ramp in N_2 at 10 °C/min. Hydrothermally aged catalysts were prepared from the fresh catalysts by exposing them to 10% H_2O in N_2 at 700 °C for 25 hours, while thermally aged catalysts were exposed to N_2 at 700 °C for 25 hours.

Initial precious metal particle size dictates the extent of deactivation caused by both sintering and sulfur poisoning [99], [187]. To assess the changes in what type of sulfur species are formed after exposure to common aging protocols, temperature programmed desorption studies after SO_2 exposure at 100 °C were performed over the fresh and aged Pd/Al_2O_3 Small and Large samples and are shown in Figure 4-2. For the fresh and aged Pd/Al_2O_3 Small sample, two SO_2 desorption regions were observed during the temperature ramp. The low temperature desorption peak (located between 100-400 °C) corresponds to molecular SO_2 and SO_2 from the decomposition of $Al_2(SO_3)$ species from the catalyst surface, while the high temperature desorption peak (located between 500-900 °C) corresponds to SO_2 from the decomposition of surface and bulk $Al_2(SO_4)_3$ species [99], [101]. However, after the exposure to aging conditions at 750 °C, the SO_2 desorption profiles during the temperature ramp changed for the hydrothermally- and thermally-aged Pd/Al_2O_3 Small sample. A decrease in both the low temperature and high temperature SO_2 desorption peaks was observed for both aged samples compared to the fresh sample; however, there are minimal differences in the SO_2 desorption profiles among the aged samples, suggesting that the inclusion of H_2O did not influence sulfur desorption. Additionally, a decrease in the amount of SO_2 adsorbed and desorbed for both aged samples compared to the fresh sample was observed (see Table 4-1). The changes in the SO_2 desorption profiles at high temperature and S mass balance of the aged samples could be indicative of the agglomeration of Pd nanoparticles [99]. This is consistent with the behavior of catalysts with a larger particle, which tends to release less high temperature sulfur species and adsorb and therefore desorb less SO_2.

Table 4-1 S mass balance for Pd/Al_2O_3 Small

	SO_2 Adsorbed (μmol)	**SO_2 Desorbed (μmol)**	**% Desorbed**
Fresh	2.5	2.7	108
Hydrothermally-Aged	1.6	1.1	69
Thermally-Aged	1.3	1.0	80
γ-Al_2O_3 Support	2.5	2.0	79

In the case of the Pd/Al_2O_3 Large sample as shown in Figure 4-2B, the SO_2 desorption profiles for both the fresh and aged samples again feature two desorption regions: the low temperature desorption peak (located between 100-400 °C) corresponds to molecular SO_2 and SO_2 from the decomposition of $Al_2(SO_3)$ species from the catalyst surface, while the high temperature desorption peak (located between 500-900 °C) corresponds to SO_2 from the decomposition of surface and bulk $Al_2(SO_4)_3$ species. After exposure to aging protocols at 750 °C, a decrease in the amount of SO_2 desorbed from high temperature region is observed for both hydrothermally- and thermally-aged samples. Similar to the findings with Pd/Al_2O_3 Small, there are minimal differences among the aged samples, suggesting that the inclusion of H_2O in the aging protocol did not influence sulfur desorption. Similar S mass balances for the fresh and aged samples are shown in Table 4-2. The minimal changes in SO_2 desorption profiles and S mass balance indicate that the number of exposed metal sites of these samples did not significantly change which is consistent with Pd catalysts with a larger particle size having slower sintering rates compared to Pd catalysts with a smaller particle size and therefore less likely to have changed much in particle size [187].

Table 4-2 S mass balance for Pd/Al_2O_3 Large

	SO_2 Adsorbed (μmol)	**SO_2 Desorbed (μmol)**	**% Desorbed**
Fresh	2.0	1.8	88
Hydrothermally-Aged	1.8	1.5	79
Thermally- Aged	1.6	1.2	75

Even though there are minimal changes in the SO_2 desorption profiles among the aged samples of each particle size, exposure to hydrothermal aging conditions led to a decrease in the SO_2 desorption profiles in the low temperature region for the Pd/Al_2O_3 Small compared to Pd/Al_2O_3 Large sample. The SO_2 desorption in the high temperature region remained unchanged after hydrothermal aging for both samples. The formation of low temperature sulfur species (i.e., molecular SO_2 and $Al_2(SO_3)$) could potentially be influenced by the gas composition of the aging protocol, while the aging temperature has more influence on the formation of high temperatures sulfur species (i.e., surface and bulk $Al_2(SO_4)_3$).

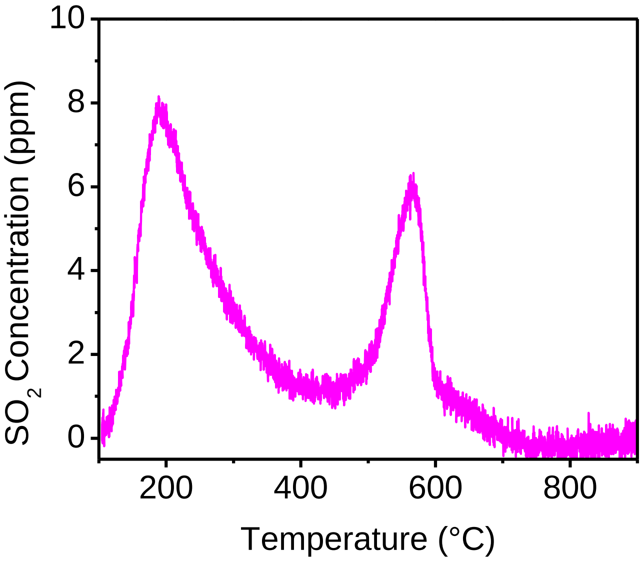

Figure 4-3 SO_2 desorption profile of the γ-Al_2O_3 support during the TPD ramp in N_2 at 10 °C/min.

Sulfur desorption profile of the γ-Al_2O_3 support during the temperature ramp is shown in Figure 4-3 after exposure to SO_2 at 100 °C. The SO_2 desorption profile again features two desorption peaks: the low temperature peak located at 200 °C corresponds to molecular SO_2 and SO_2 from the decomposition of $Al_2(SO_3)$ species from the catalyst surface, while the high temperature desorption peak located at 575 °C corresponds to SO_2 from the decomposition of surface and bulk $Al_2(SO_4)_3$ species. Considering that the high temperature desorption peak of the γ-Al_2O_3 support occurs at a lower temperature, these findings suggest that the number of exposed Pd metal sites impacts the formation and stability of high temperature sulfur species.

4.3.3 Pd/CeO2 TPD after SO2 Exposure

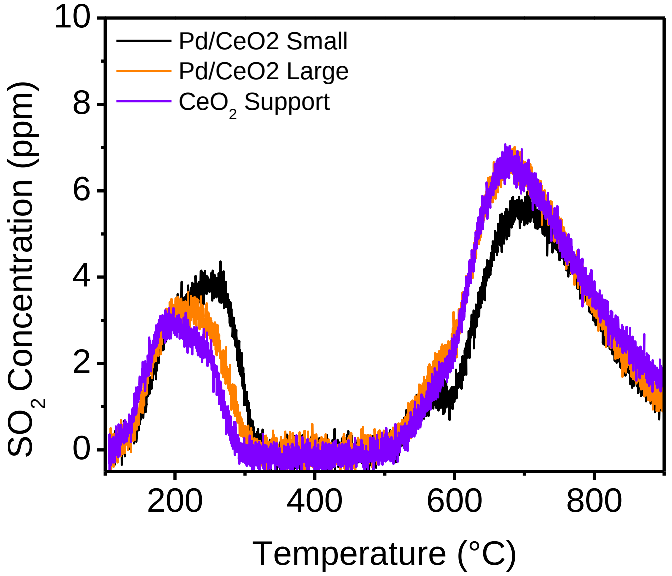

Figure 4-4 SO_2 desorption profiles for fresh Pd/CeO_2 Small (black), Pd/CeO_2 Large (orange) and CeO_2 support (purple) during the TPD ramp in N_2 at 10 °C/min.

While ample literature addresses the impact of number of exposed metal sites on sulfur speciation on Al_2O_3 supported catalysts, we extended these insights to catalysts supported on CeO_2. Figure 4-4 shows the SO_2 desorption profiles for fresh Pd/CeO_2 Small and Pd/CeO_2 Large during the temperature ramp. Unlike catalysts supported on Al_2O_3, minimal changes in the SO_2 desorption profiles are observed with the CeO_2-supported samples. Figure 4-4 shows the SO_2 desorption profiles for the CeO_2 support used in these catalysts, and its desorption profile is similar to the ones for the supported catalysts. Sulfur mass balances for both the supported catalysts and the CeO_2 support can be found on Table 4-3, and the amount of SO_2 adsorbed and desorbed for these samples are nearly identical. The resemblances in SO_2 desorption and sulfur mass balances suggest that, for CeO_2-supported catalysts, neither the number of exposed metal sites nor the addition of Pd impacts sulfur speciation on the catalyst surface.

Table 4-3 S mass balance for CeO_2-supported catalysts

	SO_2 Adsorbed (μmol)	**SO_2 Desorbed (μmol)**	**% Desorbed**
Pd/CeO_2 Small	2.1	2.1	100
Pd/CeO_2 Large	2.3	2.3	100
CeO_2 Support	2.5	2.3	94

4.3.4 CO pulse injection characterization

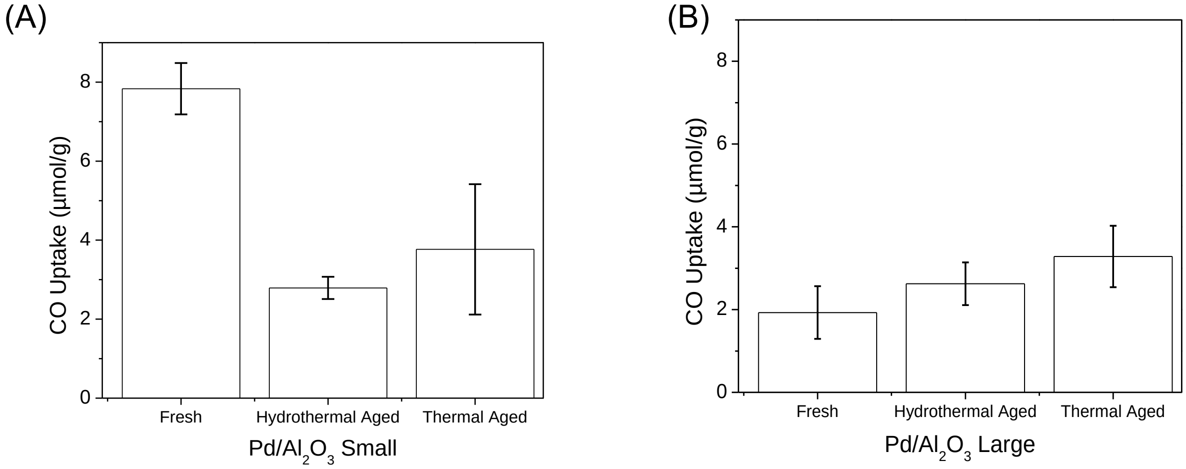

Figure 4-5 Average CO uptake of the fresh, hydrothermal, and thermal aged (A) Pd/Al_2O_3 Small and (B) Pd/Al_2O_3 Large samples.

To assess the changes in particle size after the aging protocols, CO pulse injection measurements were performed on the fresh and aged samples. In this protocol, the sample is dosed with a known CO volume until saturation. These measurements were performed three times over the sample to check reproducibility. We used Eq. 4.1 to calculate the particle size for spherical particles using the CO uptake from these measurements. Figure 4-5A shows the CO uptake for the fresh and aged Pd/Al_2O_3 Small samples. The average CO uptake (and particle size) of the fresh, hydrothermally, and thermally aged Pd/Al_2O_3 Small samples was 7.1 (7.4 nm), 2.8 (19 nm), and 3.8 (14 nm)

μmol/g_{cat} respectively. The lower CO uptake on the aged samples suggests that Pd particle size increased after exposure to 750 °C aging protocols and it was confirmed with particle size calculations. The inclusion of H_2O during the aging protocol results in a lower average CO uptake compared to the average CO uptake of the thermally aged sample. These CO uptake results on the fresh and aged Pd/Al_2O_3 Small samples confirm the changes in particle size that led to differences in the S mass balance and SO_2 desorption profiles during the temperature ramp. With particle size increasing during the aging protocol, the interfacial area between the precious metal and the support decreases, resulting in less adsorption and spillover of SO_2 onto the support.

As shown in Figure 4-5B, the average CO uptake (and particle size) of the fresh, hydrothermally, and thermally aged the Pd/Al_2O_3 Large samples was 1.9 (28 nm), 2.6 (20 nm), and 3.3 (16 nm) μmol/g_{cat}, respectively. The increase in CO uptake suggests that the particle size decreased after the application of aging protocols at 750 °C, which could indicate Pd redispersion. The extent of redispersion that occurred during the aging protocol is similar for both aged catalysts based on the particle size and sulfur desorption profiles during the temperature ramp.

4.3.5 CO oxidation baseline activity

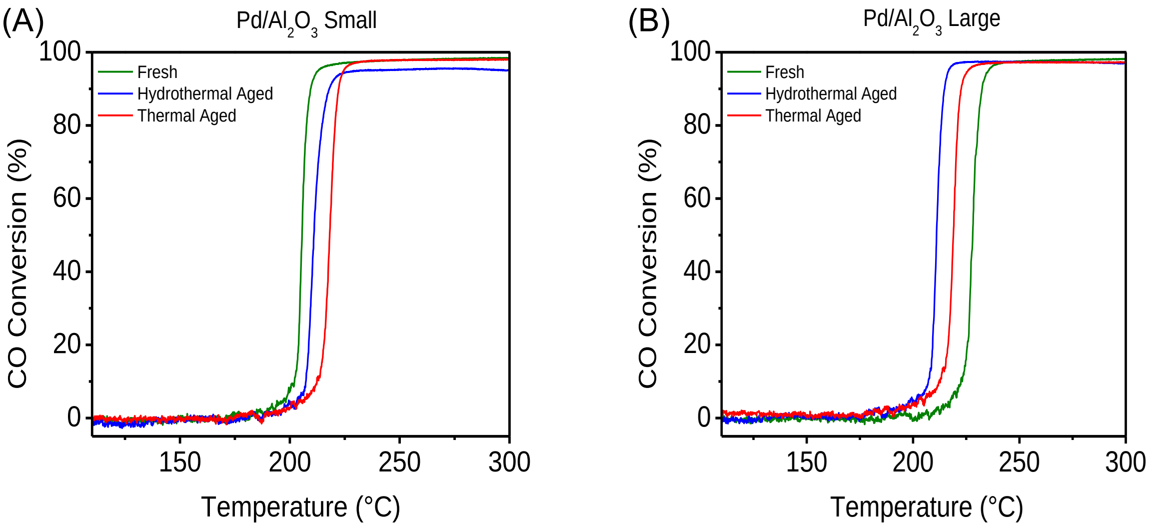

Figure 4-6 CO conversion profiles for fresh (green), hydrothermal aged (blue) and thermal aged (red) (A) Pd/Al$_2$O$_3$ Small and (B) Pd/Al$_2$O$_3$ Large samples.

Now that the sulfur speciation and particle size of the catalysts after exposure to 750 °C have been evaluated, we wanted to investigate how these aging protocols may affect catalytic activity of these samples after sulfur exposure. The CO oxidation activity was first investigated for the fresh and aged Pd/Al$_2$O$_3$ samples as shown in Figure 6. CO oxidation was chosen due to its significance in DOC applications and its inhibitory effect on other DOC reactions. In Figure 4-6A, the CO conversion profiles are depicted for the fresh, hydrothermally, and thermally aged Pd/Al$_2$O$_3$ Small samples. The temperatures at 50% conversion (T_{50}) of these samples are 206 °C, 211 °C, and 218 °C, respectively. Literature results suggest that catalysts with a larger Pd particle size exhibit higher CO light-off temperatures [40], and these changes in T_{50} confirm particle size changes, albeit not to a significant extent since the T_{50} values are close to each other. However, based on the CO pulse injection results, the thermally-aged sample showed a greater CO uptake compared to the hydrothermally-aged sample. According to Bergeld et al. [197] and Gong et al. [198] , the presence of water could promote CO oxidation due to the reaction between CO and surface hydroxyl species. In this case, we speculate that in the hydrothermally aged samples, the onset temperature for CO conversion being lower than in the thermally aged sample could be attributed to the hydroxyl-assisted CO oxidation from residual hydroxyl formed during the exposure to hydrothermal aging conditions [199].

Figure 4-6B shows the CO conversion profiles for the fresh, hydrothermally-, and thermally-aged Pd/Al_2O_3 Large samples. The temperature at 50% conversion (T_{50}) of the fresh, hydrothermally-, and thermally-aged samples is 228°C, 211 °C, and 219 °C, respectively. Based on the CO pulse injection results, the aging protocols led to an increase in CO uptake on the aged samples compared to the fresh sample, consistent with the lower T_{50} values for the aged samples. Similar to the results for Pd/Al_2O_3 Small sample, the CO uptake for the thermally-aged sample is higher than for the hydrothermally-aged samples, despite the CO conversion profile for the hydrothermally-aged sample being lower than for the thermal aged sample. Again, we speculate that reaction between CO and residual hydroxyl formed during the hydrothermal aging process could also be responsible for the lower CO conversion profile.

Typically, kinetic measurements, such as turnover frequency and activation energy, are performed under steady state conditions. However, to compare these kinetic measurements with literature values, the activation energy of the hydrothermally-aged samples for both particle sizes was calculated from the temperature ramps found in Figure 4-6. The estimated activation energies for the hydrothermally-aged Pd/Al_2O_3 Small and Pd/Al_2O_3 Large samples are 268 kJ/mol and 200 kJ/mol, respectively. According to the literature reports, the activation energy for CO oxidation on Pd catalysts supported on Al_2O_3 is in the range of 50-130 kJ/mol [200]. Since the estimated values are out of range from the values found in the literature, the disagreement of these values could be due to the calculation of these values from transient data.

4.3.6 Effects of Aging on Sulfur Exposure

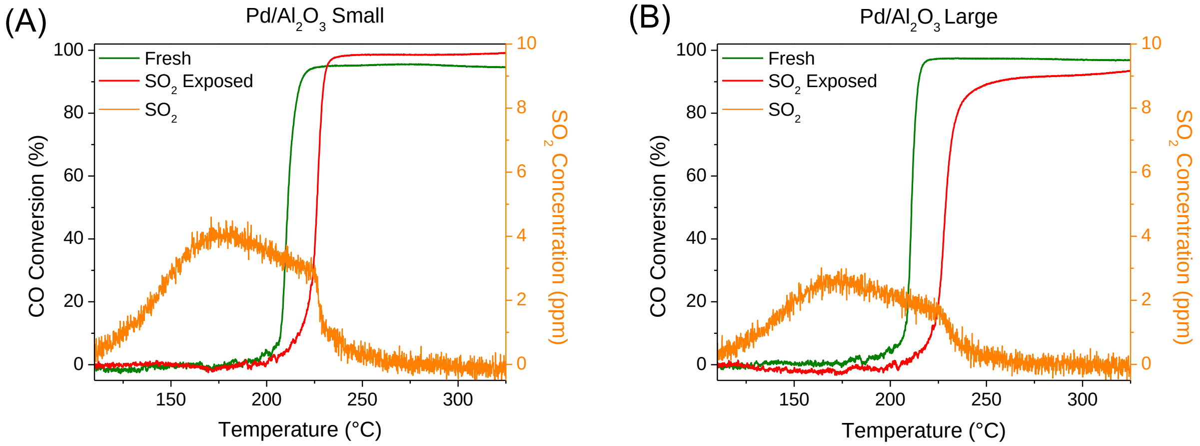

Figure 4-7 CO conversion profiles for fresh (green) and SO_2 exposed (red) (A) Pd/Al_2O_3 Small and (B) Pd/Al_2O_3 Large hydrothermally aged samples, and the SO_2 desorption profiles (orange) during the CO oxidation temperature ramp after SO_2 exposure.

To summarize our findings so far, the gas composition of the aging protocol influences sulfur speciation based on the SO_2 TPD results and the particle size changes after aging were probed using CO pulse injection. Next, the impact of sulfur exposure on the CO oxidation activity Pd/Al_2O_3 Small and Large hydrothermally-aged samples was explored. Figure 4-7 shows the CO conversion profiles before and after SO_2 exposure at 100 °C of the Pd/Al_2O_3 Small and Large hydrothermally-aged samples, and the SO_2 desorption profiles during the SO_2-exposed CO oxidation temperature ramp. For the hydrothermally-aged Pd/Al_2O_3 Small sample, exposure to SO_2 shifts the CO conversion profile to higher temperatures based on the T_{50} values (fresh – 211 °C vs. SO_2 exposed

– 226 °C). However, exposure to SO_2 did result in complete conversion of CO during the temperature ramp unlike the fresh sample. Looking at the SO_2 desorption profile during the temperature ramp, as temperature increased, SO_2 desorption from low temperature sulfur species (i.e., molecular SO_2 and $Al_2(SO_3)$) increased as well. As CO conversion reached completion, the SO_2 concentration sharply decreased. For the hydrothermally aged Pd/Al_2O_3 Large sample, exposure to SO_2 shifts the CO conversion profile to higher temperatures based on the T_{50} values (fresh – 211 °C vs. SO_2 exposed – 229 °C). However, in this case, exposure to SO_2 did not result in the complete conversion of CO during the temperature ramp. We speculate that the decomposition of desorption of sulfur species could potentially affect high temperature oxidation activity. Sulfur desorption from low temperature sulfur species also occurred during the experiment; however, in contrast to the SO_2 desorption from the hydrothermally aged Pd/Al_2O_3 Small sample, SO_2 desorption gradually decreased as the CO conversion at high temperature slowed too. Based on the SO_2 TPD profiles from Figure 4-2, we observe a less formation of low temperature sulfur species on the hydrothermally aged Pd/Al_2O_3 Small sample compared to hydrothermally aged Pd/Al_2O_3 Large sample. We speculate that these species can be easily decomposed, resulting in reduced sulfur inhibition based on the full conversion of CO as shown in Figure 4-7A.

4.4 Conclusions

In this study, we synthesized uniform Pd nanoparticles with two particle sizes (3.4 nm and 13.1 nm) and deposited them onto supports relevant to aftertreatment applications, Al_2O_3 and CeO_2. The gas composition of the aging protocols (hydrothermal vs. thermal) and number of exposed metal sites influence sulfur speciation for both Al_2O_3-supported catalysts. In the case of CeO_2-supported catalysts, number of exposed metal sites does not lead to changes in sulfur speciation. CO pulse injection measurements were used to evaluate the changes in particle size that occurred during aging and show that catalysts with a smaller particle size are more susceptible to sintering compared to catalysts with a larger particle size. Even though aging does affect CO oxidation activity for catalysts with a smaller particle size, they exhibit higher resistance to sulfur poisoning. Conversely, a catalyst with a larger particle size experiences the opposite effect.

5. Conclusions and Future Directions

Evaluating the sulfur resistance of new oxidation catalyst formulations and understanding their regeneration remain crucial for aftertreatment implementation due to the persistent presence of sulfur in fuels and lubricant oils. This dissertation addressed the effects of sulfur poisoning on new formulations of oxidation catalysts (Chapter 2 and 3), enhanced regeneration strategies to recover catalytic activity (Chapter 2), and further investigated the particle size effects on sulfur speciation after aftertreatment catalyst aging protocols (Chapter 4).

To summarize this work, we focus entirely on the effects of sulfur poisoning and regeneration on the performance of oxidation catalysts – a crucial metric for aftertreatment implementation. Yet, this provides a partial answer, overlooking the interactions between SO_2 and the catalyst surface. The use of *in situ/operando* characterization can help fill in the blanks in *how* sulfur causes deactivation and *how* regeneration occurs, especially under transient conditions. In Chapter 2, we assessed the sulfur poisoning and regeneration of a bilayer PGM + $Mn_{0.5}Fe_{2.5}O_4$ spinel catalyst; while we were able to regenerate catalytic activity after the application of various regeneration methods, remaining questions linger regarding the sulfur speciation on the spinel material and structural changes due to sulfur poisoning, demanding further investigation. Chapter 3 introduced an avenue of increasing sulfur resistance by adding small substitutions of Cu to Pd-based diesel oxidation catalysts. In this study, only one regeneration strategy was employed, and even though future studies could explore different regeneration protocols, remaining questions regarding how Cu can potentially affect $PdSO_4$ decomposition and the remaining product (i.e., Pd_xS) still need to be addressed. Chapter

4 investigated the effects of particle size on sulfur speciation after common ageing protocols. Here, the use of *in situ* studies could give us more supporting evidence regarding sulfur speciation.

However, the biggest challenge in sulfur research – and the reason why we heavily relied on performance tests – is the potential equipment damage due to sulfur exposure. The work that has been presented in this dissertation was performed in a reactor modified with sulfur-resistant coatings, which allow us to accurately quantify and obtain S mass balances.

6. References

[1] S. Cisneros, *The house on mango street*. London, England: Bloomsbury Publishing PLC, 2004.

[2] E. R. Stephens, P. L. Hanst, R. C. Doerr, and W. E. Scott, “Auto exhaust: Composition and photolysis products,” *J. Air Pollut. Control Assoc.*, vol. 8, no. 4, pp. 333–335, 1959, doi: 10.1080/00022470.1959.10467861.

[3] A. J. Haagen-Smit, “Chemistry and Physiology of Los Angeles Smog,” *Ind. Eng. Chem.*, vol. 44, no. 6, pp. 1342–1346, 1952, doi: 10.1021/ie50510a045.

[4] G. Z. Whitten, “The chemistry of smog formation: A review of current knowledge,” *Environ. Int.*, vol. 9, no. 6, pp. 447–463, 1983, doi: 10.1016/0160-4120(83)90003-X.

[5] A. Y. Watson, R. R. Bates, and D. Kennedy, *Air Pollution, the Automobile, and Public Health*. National Academies Press, 2003.

[6] S. K. Hoekman and J. S. Welstand, “Vehicle emissions and air quality: The early years (1940s–1950s),” *Atmosphere (Basel).*, vol. 12, no. 10, 2021, doi: 10.3390/atmos12101354.

[7] T. J. Wallington, J. E. Anderson, R. H. Dolan, and S. L. Winkler, “Vehicle Emissions and Urban Air Quality: 60 Years of Progress,” *Atmosphere (Basel).*, vol. 13, no. 5, 2022, doi: 10.3390/atmos13050650.

[8] F. Register, “Greenhouse Gas Emissions and Fuel Efficiency Standards for Medium- and Heavy-Duty Engines and Vehicles— Phase 2,” vol. 81, no. 206. pp. 73478–74274, 2016.

[9] “National Air Quality: Status and Trends of Key Air Pollutants,” 2023. https://www.epa.gov/air-trends/carbon-monoxide-trends (accessed Oct. 31, 2023).

[10] J. T. Kummer, “Catalysts for automobile emission control,” *Prog. Energy Combust. Sci.*, vol. 6, no. 2, pp. 177–199, 1980, doi: 10.1016/S0167-2991(08)63984-1.

[11] M. V. Twigg, “Catalytic control of emissions from cars,” *Catal. Today*, vol. 163, no. 1, pp. 33–41, 2011, doi: 10.1016/j.cattod.2010.12.044.

[12] S. Rood, S. Eslava, A. Manigrasso, and C. Bannister, “Recent advances in gasoline three-way catalyst formulation: A review,” *Proc. Inst. Mech. Eng. Part D J. Automob. Eng.*, vol. 234, no. 4, pp. 936–949, 2020, doi: 10.1177/0954407019859822.

[13] R. J. Farrauto, M. Deeba, and S. Alerasool, “Gasoline automobile catalysis and its historical journey to cleaner air,” *Nat. Catal.*, vol. 2, no. 7, pp. 603–613, Jul. 2019, doi: 10.1038/s41929-019-0312-9.

[14] R. M. Heck and R. J. Farrauto, “Automobile exhaust catalysts,” *Appl. Catal. A Gen.*, vol. 221, no. 1–2, pp. 443–457, 2001, doi: 10.1016/S0926-860X(01)00818-3.

[15] H. S. Gandhi, G. W. Graham, and R. W. McCabe, “Automotive exhaust catalysis,” *J. Catal.*, vol. 216, no. 1–2, pp. 433–442, 2003, doi: 10.1016/S0021-9517(02)00067-2.

[16] C. Huang, W. Shan, Z. Lian, Y. Zhang, and H. He, “Recent advances in three-way catalysts of natural gas vehicles,” *Catal. Sci. Technol.*, vol. 10, no. 19, pp. 6407–6419, 2020, doi: 10.1039/d0cy01320j.

[17] A. Russell and W. S. Epling, “Diesel oxidation catalysts,” *Catal. Rev. - Sci. Eng.*, vol. 53, no. 4, pp. 337–423, 2011, doi: 10.1080/01614940.2011.596429.

[18] A. V. Karre, R. K. Garlapalli, A. Jena, and N. Tripathi, “State of the art developments in oxidation performance and deactivation of diesel oxidation catalyst (DOC),” *Catal. Commun.*, vol. 179, no. May, p. 106682, 2023, doi: 10.1016/j.catcom.2023.106682.

[19] J. T. Kummer, “Use of noble metals in automobile exhaust catalysts,” *J. Phys. Chem.*, vol. 90, no. 20, pp. 4747–4752, 1986, doi: 10.1021/j100411a008.

[20] D. Jiang, K. Khivantsev, and Y. Wang, “Low-Temperature Methane Oxidation for Efficient Emission Control in Natural Gas Vehicles: Pd and beyond,” *ACS Catal.*, vol. 10, no. 23, pp. 14304–14314, Nov. 2020, doi: 10.1021/acscatal.0c03338.

[21] P. Taylor, M. Shelef, and G. W. Graham, “Why Rhodium in Automotive Three-Way Catalysts?,” *Catal. Rev. - Sci. Eng.*, vol. 36, no. 3, pp. 433–457, 1994.

[22] J. Wang, H. Chen, Z. Hu, M. Yao, and Y. Li, “A review on the Pd-based three-way catalyst,” *Catal. Rev. - Sci. Eng.*, vol. 57, no. 1, pp. 79–144, 2015, doi: 10.1080/01614940.2014.977059.

[23] M. Trueba and S. P. Trasatti, “γ-alumina as a support for catalysts: A review of fundamental aspects,” *Eur. J. Inorg. Chem.*, no. 17, pp. 3393–3403, 2005, doi: 10.1002/ejic.200500348.

[24] D. Mukherjee and B. M. Reddy, “Significance of Oxygen Storage Capacity of Catalytic Materials in Emission Control Application,” *Emiss. Control Sci. Technol.*, vol. 6, no. 4, pp. 381–389, 2020, doi: 10.1007/s40825-020-00170-2.

[25] J. Kašpar, P. Fornasiero, and M. Graziani, “Use of CeO2-based oxides in the three-way catalysis,” *Catal. Today*, vol. 50, no. 2, pp. 285–298, 1999, doi: 10.1016/S0920-5861(98)00510-0.

[26] R. J. Gorte, “Ceria in Catalysis: From Automotive Applications to the Water-Gas Shift Reaction,” *AIChE J.*, vol. 56, no. 5, pp. 1126–1135, 2010, doi: 10.1002/aic.

[27] P. Li, X. Chen, Y. Li, and J. W. Schwank, “A review on oxygen storage capacity of CeO 2 -based materials: Influence factors, measurement techniques, and applications in reactions related to catalytic automotive emissions control,” *Catal. Today*, vol. 327, no. May 2018, pp. 90–115, May 2019, doi: 10.1016/j.cattod.2018.05.059.

[28] H. C. Yao and Y. F. Y. Yao, “Ceria in automotive exhaust catalysts. I. Oxygen

storage," *J. Catal.*, vol. 86, no. 2, pp. 254–265, 1984, doi: 10.1016/0021-9517(84)90371-3.

[29] T. Bunluesin, R. J. Gorte, and G. W. Graham, "Studies of the water-gas-shift reaction on ceria-supported Pt, Pd, and Rh: Implications for oxygen-storage properties," *Appl. Catal. B Environ.*, vol. 15, no. 1–2, pp. 107–114, 1998, doi: 10.1016/S0926-3373(97)00040-4.

[30] R. J. Gorte and S. Zhao, "Studies of the water-gas-shift reaction with ceria-supported precious metals," *Catal. Today*, vol. 104, no. 1, pp. 18–24, 2005, doi: 10.1016/j.cattod.2005.03.034.

[31] W. Sutthisripok, S. Sattayanurak, and L. Sikong, "Effect of specific surface area on oxygen storage capacity (OSC) and methane steam reforming reactivity of CeO2," *J. Porous Mater.*, vol. 15, no. 5, pp. 519–525, 2008, doi: 10.1007/s10934-007-9107-5.

[32] M. Cargnello *et al.*, "Control of metal nanocrystal size reveals metal-support interface role for ceria catalysts," *Science (80-.).*, vol. 341, no. 6147, pp. 771–773, 2013, doi: 10.1126/science.1240148.

[33] S. Bedrane, C. Descorme, and D. Duprez, "Towards the comprehension of oxygen storage processes on model three-way catalysts," *Catal. Today*, vol. 73, no. 3–4, pp. 233–238, 2002, doi: 10.1016/S0920-5861(02)00005-6.

[34] J. Kašpar and P. Fornasiero, "Nanostructured materials for advanced automotive de-pollution catalysts," *J. Solid State Chem.*, vol. 171, no. 1–2, pp. 19–29, 2003, doi: 10.1016/S0022-4596(02)00141-X.

[35] C. E. Hori *et al.*, "Thermal stability of oxygen storage properties in a mixed CeO 2-ZrO 2 system," *Appl. Catal. B, Environ.*, vol. 16, pp. 105–117, 1998.

[36] Y. Madier, C. Descorme, A. M. Le Govic, and D. Duprez, "Oxygen mobility in CeO2 and CexZr(1-x)O2 compounds: Study by CO transient oxidation and18O/16O isotopic exchange," *J. Phys. Chem. B*, vol. 103, no. 50, pp. 10999–11006, 1999, doi: 10.1021/jp991270a.

[37] S. Bedrane, C. Descorme, and D. Duprez, "Investigation of the oxygen storage process on ceria- and ceria-zirconia-supported catalysts," *Catal. Today*, vol. 75, no. 1–4, pp. 401–405, 2002, doi: 10.1016/S0920-5861(02)00089-5.

[38] A. Kalantar Neyestanaki, F. Klingstedt, T. Salmi, and D. Y. Murzin, "Deactivation of postcombustion catalysts, a review," *Fuel*, vol. 83, no. 4–5, pp. 395–408, 2004, doi: 10.1016/j.fuel.2003.09.002.

[39] Q. Xu, K. C. Kharas, B. J. Croley, and A. K. Datye, "The Sintering of Supported Pd Automotive Catalysts," *ChemCatChem*, vol. 3, no. 6, pp. 1004–1014, 2011, doi: 10.1002/cctc.201000392.

[40] X. Chen, Y. Cheng, C. Y. Seo, J. W. Schwank, and R. W. McCabe, "Aging, re-dispersion, and catalytic oxidation characteristics of model Pd/Al2O3 automotive three-way catalysts," *Appl. Catal. B Environ.*, vol. 163, pp. 499–509, 2015, doi:

10.1016/j.apcatb.2014.08.018.

[41] M. Machida *et al.*, “Catalyst Deactivation via Rhodium-Support Interactions under High-Temperature Oxidizing Conditions: A Comparative Study on Hexaaluminates versus Al2O3,” *ACS Catal.*, vol. 11, no. 15, pp. 9462–9470, 2021, doi: 10.1021/acscatal.1c01695.

[42] C.-H. Li, J. Wu, A. B. Getsoian, G. Cavataio, and J. R. Jinschek, “Direct Observation of Rhodium Aluminate (RhAlO x) and Its Role in Deactivation and Regeneration of Rh/Al 2 O 3 under Three-Way Catalyst Conditions,” *Chem. Mater.*, 2022, doi: 10.1021/acs.chemmater.1c03513.

[43] A. Beniya and S. Higashi, “Towards dense single-atom catalysts for future automotive applications,” *Nat. Catal.*, vol. 2, no. 7, pp. 590–602, 2019, doi: 10.1038/s41929-019-0282-y.

[44] Y. Lu, Z. Zhang, F. Lin, H. Wang, and Y. Wang, “Single-atom Automobile Exhaust Catalysts,” *ChemNanoMat*, vol. 6, no. 12, pp. 1659–1682, 2020, doi: 10.1002/cnma.202000407.

[45] J. Jones *et al.*, “Thermally stable single-atom platinum-on-ceria catalysts via atom trapping,” *Science (80-.).*, vol. 353, no. 6295, pp. 150–154, 2016, doi: 10.1126/science.aaf8800.

[46] H. Jeong, G. Lee, B. S. Kim, J. Bae, J. W. Han, and H. Lee, “Fully Dispersed Rh Ensemble Catalyst to Enhance Low-Temperature Activity,” *J. Am. Chem. Soc.*, vol. 140, no. 30, pp. 9558–9565, 2018, doi: 10.1021/jacs.8b04613.

[47] Y. F. Y. Yao, “Oxidation of Alkanes over Noble Metal Catalysts,” *Ind. Eng. Chem. Prod. Res. Dev.*, vol. 19, no. 3, pp. 293–298, 1980, doi: 10.1021/i360075a003.

[48] M. S. Wilburn and W. S. Epling, “Formation and Decomposition of Sulfite and Sulfate Species on Pt/Pd Catalysts: An SO 2 Oxidation and Sulfur Exposure Study,” *ACS Catal.*, vol. 9, no. 1, pp. 640–648, 2019, doi: 10.1021/acscatal.8b03529.

[49] T. Hamzehlouyan, C. Sampara, J. Li, A. Kumar, and W. Epling, “Experimental and kinetic study of SO2 oxidation on a Pt/γ-Al2O3 catalyst,” *Appl. Catal. B Environ.*, vol. 152–153, no. x, pp. 108–116, 2014, doi: 10.1016/j.apcatb.2014.01.005.

[50] T. Hamzehlouyan, C. Sampara, J. Li, A. Kumar, and W. Epling, “Sulfur Poisoning of a Pt/Al2O3 Oxidation Catalyst: Understanding of SO2, SO3 and H2SO4 Impacts,” *Top. Catal.*, vol. 59, no. 10–12, pp. 1028–1032, Jul. 2016, doi: 10.1007/s11244-016-0592-0.

[51] K. Akihama, Y. Takatori, K. Inagaki, S. Sasaki, and A. Dean, “Mechanism of the smokeless rich diesel combustion by reducing temperature,” *SAE Int.*, vol. 2001-01–06, 2001, doi: https://doi.org/10.4271/2001-01-0655.

[52] M. Zheng, U. Asad, G. T. Reader, Y. Tan, and M. Wang, “Energy efficiency improvement strategies for a diesel engine in low-temperature combustion,” *Int. J. Energy Res.*, vol. 33, pp. 8–28, 2009, doi: 10.1002/er.

[53] M. Zammit *et al.*, “Future Automotive Aftertreatment Solutions: The 150 ° C Challenge Workshop Report,” 2012. [Online]. Available: http://www.ntis.gov/ordering.htm

[54] H. S. Gandhi and M. Shelef, “Effects of sulphur on noble metal automotive catalysts,” *Appl. Catal.*, vol. 77, no. 2, pp. 175–186, 1991, doi: 10.1016/0166-9834(91)80063-3.

[55] R. A. Kerr, “Natural Gas From Shale Bursts Onto the Scene,” *Sci. Mag. 328*, vol. 328, no. June, pp. 1624–1626, 2010.

[56] S. Pischinger, M. Umierski, and B. Hüchtebrock, “New CNG Concepts for Passenger Cars: High Torque Engines with Superior Fuel Consumption,” *SAE Tech. Pap. Ser.*, vol. 1, no. 724, 2003, doi: 10.4271/2003-01-2264.

[57] B. A. Raj, “Methane Emission Control,” *Johnson Matthey Technol. Rev.*, vol. 60, no. 4, pp. 228–235, Jan. 2016, doi: 10.1595/205651316x692554.

[58] Intergovernmental Panel on Climate Change, *Anthropogenic and Natural Radiative Forcing*, vol. 6, no. 4. Cambridge: Cambridge University Press, 2014.

[59] R. Horn and R. Schlögl, “Methane Activation by Heterogeneous Catalysis,” *Catal. Letters*, vol. 145, no. 1, pp. 23–39, Jan. 2015, doi: 10.1007/s10562-014-1417-z.

[60] E. D. German and M. Sheintuch, “Predicting CH4 dissociation kinetics on metals: Trends, sticking coefficients, h tunneling, and kinetic isotope effect,” *J. Phys. Chem. C*, vol. 117, no. 44, pp. 22811–22826, Nov. 2013, doi: 10.1021/jp406937r.

[61] P. Gélin and M. Primet, “Complete oxidation of methane at low temperature over noble metal based catalysts: A review,” *Appl. Catal. B Environ.*, vol. 39, no. 1, pp. 1–37, 2002, doi: 10.1016/S0926-3373(02)00076-0.

[62] R. Di Monte and J. Kašpar, “On the role of oxygen storage in three-way catalysis,” *Top. Catal.*, vol. 28, no. 1–4, pp. 47–58, 2004, doi: 10.1023/B:TOCA.0000024333.08447.f7.

[63] E. Aneggi, M. Boaro, S. Colussi, C. de Leitenburg, and A. Trovarelli, *Ceria-Based Materials in Catalysis: Historical Perspective and Future Trends*, 1st ed., vol. 50. Elsevier B.V., 2016. doi: 10.1016/bs.hpcre.2016.05.002.

[64] Neha, R. Prasad, and S. Vir Singh, “Catalytic abatement of CO, HCs and soot emissions over spinel-based catalysts from diesel engines: An overview,” *J. Environ. Chem. Eng.*, vol. 8, no. 2, p. 103627, Jan. 2020, doi: 10.1016/j.jece.2019.103627.

[65] S. Yang, C. Wang, J. Li, N. Yan, L. Ma, and H. Chang, “Low temperature selective catalytic reduction of NO with NH3 over Mn-Fe spinel: Performance, mechanism and kinetic study,” *Appl. Catal. B Environ.*, vol. 110, pp. 71–80, Nov. 2011, doi: 10.1016/j.apcatb.2011.08.027.

[66] M. Zawadzki, W. Walerczyk, F. E. López-Suárez, M. J. Illán-Gómez, and A. Bueno-López, “CoAl2O4 spinel catalyst for soot combustion with NOx/O2,” *Catal.*

Commun., vol. 12, no. 13, pp. 1238–1241, Jul. 2011, doi: 10.1016/j.catcom.2011.04.021.

[67] H. Lin, Y. Li, W. Shangguan, and Z. Huang, “Soot oxidation and NOx reduction over BaAl2O4 catalyst,” *Combust. Flame*, vol. 156, no. 11, pp. 2063–2070, Nov. 2009, doi: 10.1016/j.combustflame.2009.08.006.

[68] S. O. Soloviev, A. Y. Kapran, and Y. P. Kurylets, “Oxidation of diesel soot on binary oxide CuCr(Co)-based monoliths,” *J. Environ. Sci. (China)*, vol. 28, pp. 171–177, Feb. 2015, doi: 10.1016/j.jes.2014.08.017.

[69] D. Fino, N. Russo, G. Saracco, and V. Specchia, “Removal of NOx and diesel soot over catalytic traps based on spinel-type oxides,” *Powder Technol.*, vol. 180, no. 1–2, pp. 74–78, 2008, doi: 10.1016/j.powtec.2007.03.003.

[70] W. F. Shangguan, Y. Teraoka, and S. Kagawa, “Simultaneous catalytic removal of NO, and diesel soot particulates over ternary AB2O4 spinel-type oxides,” 1996.

[71] P. Mountapmbeme Kouotou *et al.*, “Structure-activity relation of spinel-type Co-Fe oxides for low-temperature CO oxidation,” *Catal. Sci. Technol.*, vol. 4, no. 9, pp. 3359–3367, 2014, doi: 10.1039/c4cy00463a.

[72] S. Trivedi, R. Prasad, and S. K. Gautam, “Design of active NiCo2O4-Δ spinel catalyst for abatement of CO-CH4 emissions from CNG fueled vehicles,” *AIChE J.*, vol. 64, no. 7, pp. 2632–2646, Jul. 2018, doi: 10.1002/aic.16162.

[73] J. Li, X. Liang, S. Xu, and J. Hao, “Catalytic performance of manganese cobalt oxides on methane combustion at low temperature,” *Appl. Catal. B Environ.*, vol. 90, no. 1–2, pp. 307–312, 2009, doi: 10.1016/j.apcatb.2009.03.027.

[74] S. A. Hosseini, D. Salari, A. Niaei, F. Deganello, G. Pantaleo, and P. Hojati, “Chemical-physical properties of spinel CoMn2O4 nano-powders and catalytic activity in the 2-propanol and toluene combustion: Effect of the preparation method,” *J. Environ. Sci. Heal. - Part A Toxic/Hazardous Subst. Environ. Eng.*, vol. 46, no. 3, pp. 291–297, Feb. 2011, doi: 10.1080/10934529.2011.539093.

[75] S. Golden, Z. Nazarpoor, and M. Launois, “Novel Mixed Metal Oxide Structure for Next Generation Three-Way Catalysts,” *SAE Int.*, vol. 2015-01–10, 2015, doi: 10.4271/2015-01-1007.

[76] Z. Nazarpoor and S. J. Golden, “Thermally Stable Compositions of OSM Free of Rare Earth Metals,” 9.486,784 B2, 2016

[77] S. Golden, Z. Nazarpoor, and R.-F. Liu, “TWC Using Advanced Spinel Materials and Prospects for BSVI Compliance,” *SAE Int.*, vol. 2017-26–01, 2017, doi: 10.4271/2017-26-0126.Copyright.

[78] S. Golden, Z. Nazarpoor, M. Launois, R. F. Liu, and P. Maram, “Development of Non-Copper Advanced Spinel Mixed Metal Oxides for Zero-Precious Metal and Ultra-Low Precious Metal Next-Generation TWC,” in *SAE Technical Papers*, SAE International, 2016. doi: 10.4271/2016-01-0933.

[79] S. B. Kang, K. Karinshak, P. W. Chen, S. Golden, and M. P. Harold, “Coupled methane and NOx conversion on Pt + Pd/Al2O3 monolith: Conversion enhancement through feed modulation and Mn0.5Fe2.5O4 spinel addition,” *Catal. Today*, vol. 360, pp. 284–293, 2021, doi: 10.1016/j.cattod.2020.02.039.

[80] S. Fouladvand, M. Skoglundh, and P. A. Carlsson, “A transient in situ infrared spectroscopy study on methane oxidation over supported Pt catalysts,” *Catal. Sci. Technol.*, vol. 4, no. 10, pp. 3463–3473, 2014, doi: 10.1039/c4cy00486h.

[81] P. A. Carlsson, E. Fridell, and M. Skoglundh, “Methane oxidation over Pt/Al2O3 and Pd/Al2O3 catalysts under transient conditions,” *Catal. Letters*, vol. 115, no. 1–2, pp. 1–7, 2007, doi: 10.1007/s10562-007-9057-1.

[82] D. Bounechada, G. Groppi, P. Forzatti, K. Kallinen, and T. Kinnunen, “Effect of periodic lean/rich switch on methane conversion over a Ce-Zr promoted Pd-Rh/Al2O3 catalyst in the exhausts of natural gas vehicles,” *Appl. Catal. B Environ.*, vol. 119–120, pp. 91–99, 2012, doi: 10.1016/j.apcatb.2012.02.025.

[83] S. Fouladvand, M. Skoglundh, and P. A. Carlsson, “Unsteady-state operation of supported platinum catalysts for high conversion of methane,” *Chem. Eng. J.*, vol. 292, pp. 321–325, 2016, doi: 10.1016/j.cej.2016.02.033.

[84] P. A. Carlsson, S. Mollner, K. Arnby, and M. Skoglundh, “Effect of periodic operation on the low-temperature activity for propane oxidation over Pt/Al2O3 catalysts,” *Chem. Eng. Sci.*, vol. 59, no. 20, pp. 4313–4323, 2004, doi: 10.1016/j.ces.2004.06.024.

[85] Z. Zhou, M. P. Harold, and D. Luss, “Enhanced NO, CO and C3H6 conversion on Pt/Pd catalysts: Impact of oxygen storage material and catalyst architecture,” *Catal. Today*, no. October 2019, pp. 1–13, 2020, doi: 10.1016/j.cattod.2020.01.026.

[86] K. Karinshak, P. W. Chen, R.-F. Liu, S. J. Golden, and M. P. Harold, “Optimizing feed modulation for coupled methane and NOx conversion over Pd-Pt/Mn0.5Fe2.5O4/Al2O3 monolith catalyst,” *Appl. Catal. B Environ.*, vol. 304, no. x, p. 120607, 2022, doi: 10.1016/j.apcatb.2021.120607.

[87] J. Gong *et al.*, “O2 dosage as a descriptor of TWC performance under lean/rich dithering in stoichiometric natural gas engines,” *Catal. Today*, vol. 360, no. February, pp. 294–304, 2021, doi: 10.1016/j.cattod.2020.02.022.

[88] M. Roger, O. Kröcher, and D. Ferri, “Assessing the effect of O2 dithering on CH4 oxidation on Pd/Al2O3,” *Chem. Eng. J.*, vol. 451, no. 4, p. 138865, 2023, doi: 10.1016/j.cej.2022.138865.

[89] J. K. Lampert, M. S. Kazi, and R. J. Farrauto, “Palladium catalyst performance for methane emissions abatement from lean bum natural gas vehicles,” *Appl. Catal. B Environ.*, vol. 14, no. 3–4, pp. 211–223, 1997, doi: 10.1016/S0926-3373(97)00024-6.

[90] H. N. Sharma, V. Sharma, A. B. Mhadeshwar, and R. Ramprasad, “Why Pt survives but Pd suffers from SOx poisoning?,” *J. Phys. Chem. Lett.*, vol. 6, no. 7, pp. 1140–

1148, 2015, doi: 10.1021/jz5027147.

[91] W. Yang, J. Gong, X. Wang, Z. Bao, Y. Guo, and Z. Wu, “A Review on the Impact of SO2 on the Oxidation of NO, Hydrocarbons, and CO in Diesel Emission Control Catalysis,” *ACS Catal.*, vol. 11, no. 20, pp. 12446–12468, Oct. 2021, doi: 10.1021/acscatal.1c03013.

[92] D. L. Mowery and R. L. McCormick, “Deactivation of alumina supported and unsupported Pdo methane oxidation catalyst: The effect of water on sulfate poisoning,” *Appl. Catal. B Environ.*, vol. 34, no. 4, pp. 287–297, 2001, doi: 10.1016/S0926-3373(01)00222-3.

[93] P. Auvinen, J. T. Hirvi, N. M. Kinnunen, and M. Suvanto, “PdSO4 Surfaces in Methane Oxidation Catalysts: DFT Studies on Stability, Reactivity, and Water Inhibition,” *ACS Catal.*, vol. 10, no. 21, pp. 12943–12953, 2020, doi: 10.1021/acscatal.0c03686.

[94] M. Y. Smirnov, A. V. Kalinkin, A. V. Pashis, I. P. Prosvirin, and V. I. Bukhtiyarov, “Interaction of SO2 with Pt model supported catalysts studied by XPS,” *J. Phys. Chem. C*, vol. 118, no. 38, pp. 22120–22135, Sep. 2014, doi: 10.1021/jp5069126.

[95] R. M. Ferrizz, R. J. Gorte, and J. M. Vohs, “TPD and XPS investigation of the interaction of SO2 with model ceria catalysts,” *Catal. Letters*, vol. 82, no. 1–2, pp. 123–129, 2002, doi: 10.1023/A:1020512713021.

[96] C. C. Chang, “Infrared studies of SO2 on γ-alumina,” *J. Catal.*, vol. 53, no. 3, pp. 374–385, 1978, doi: 10.1016/0021-9517(78)90109-4.

[97] M. Y. Smirnov *et al.*, “Interaction of Al2O3 and CeO2 Surfaces with SO2 and SO2 + O2 studied by X-ray Photoelectron Spectroscopy,” *J. Phys. Chem. B*, vol. 109, no. 23, pp. 11712–11719, 2005, doi: 10.1021/jp0508249.

[98] L. S. Escandón, S. Ordóñez, A. Vega, and F. V. Díez, “Sulphur poisoning of palladium catalysts used for methane combustion: Effect of the support,” *J. Hazard. Mater.*, vol. 153, no. 1–2, pp. 742–750, 2008, doi: 10.1016/j.jhazmat.2007.09.017.

[99] M. S. Wilburn and W. S. Epling, “SO2 adsorption and desorption characteristics of Pd and Pt catalysts: Precious metal crystallite size dependence,” *Appl. Catal. A Gen.*, vol. 534, pp. 85–93, 2017, doi: 10.1016/j.apcata.2017.01.015.

[100] M. S. Wilburn and W. S. Epling, “Sulfur deactivation and regeneration of mono- and bimetallic Pd-Pt methane oxidation catalysts,” *Appl. Catal. B Environ.*, vol. 206, pp. 589–598, 2017, doi: 10.1016/j.apcatb.2017.01.050.

[101] M. S. Wilburn and W. S. Epling, “A Summary of Sulfur Deactivation , Desorption , and Regeneration Characteristics of Mono- and Bimetallic Pd-Pt Methane Oxidation Catalysts : Pd : Pt Mole Ratio and Particle Size Dependency,” *Emiss. Control Sci. Technol.*, vol. 4, pp. 78–89, 2018.

[102] G. Corro, C. Cano, and J. L. G. Fierro, “A study of Pt-Pd/γ-Al2O3 catalysts for methane oxidation resistant to deactivation by sulfur poisoning,” *J. Mol. Catal. A Chem.*, vol. 315, no. 1, pp. 35–42, Jan. 2010, doi: 10.1016/j.molcata.2009.08.023.

[103] N. Sadokhina, G. Smedler, U. Nylén, M. Olofsson, and L. Olsson, “Deceleration of SO2 poisoning on PtPd/Al2O3 catalyst during complete methane oxidation,” *Appl. Catal. B Environ.*, vol. 236, no. April, pp. 384–395, 2018, doi: 10.1016/j.apcatb.2018.05.018.

[104] P. Lott *et al.*, “Understanding sulfur poisoning of bimetallic Pd-Pt methane oxidation catalysts and their regeneration,” *Appl. Catal. B Environ.*, vol. 278, Dec. 2020, doi: 10.1016/j.apcatb.2020.119244.

[105] M. Tepluchin, S. Kureti, M. Casapu, E. Ogel, S. Mangold, and J. D. Grunwaldt, “Study on the hydrothermal and SO2 stability of Al2O3-supported manganese and iron oxide catalysts for lean CO oxidation,” *Catal. Today*, vol. 258, pp. 498–506, 2015, doi: 10.1016/j.cattod.2015.01.010.

[106] F. Lin *et al.*, “Catalytic oxidation of NO by O2 over CeO2-MnOx: SO2 poisoning mechanism,” *RSC Adv.*, vol. 6, no. 37, pp. 31422–31430, 2016, doi: 10.1039/c6ra03818b.

[107] N. Ottinger, R. Veele, Y. Xi, and Z. G. Liu, “Desulfation of Pd-based Oxidation Catalysts for Lean-burn Natural Gas and Dual-fuel Applications,” *SAE Int. J. Engines*, vol. 8, no. 4, pp. 1472–1477, 2015, doi: 10.4271/2015-01-0991.

[108] F. Arosio, S. Colussi, A. Trovarelli, and G. Groppi, “Effect of alternate CH4-reducing/lean combustion treatments on the reactivity of fresh and S-poisoned Pd/CeO2/Al2O3 catalysts,” *Appl. Catal. B Environ.*, vol. 80, no. 3–4, pp. 335–342, 2008, doi: 10.1016/j.apcatb.2007.11.030.

[109] F. Arosio, S. Colussi, G. Groppi, and A. Trovarelli, “Regeneration of S-poisoned Pd/Al2O3 catalysts for the combustion of methane,” *Catal. Today*, vol. 117, no. 4, pp. 569–576, 2006, doi: 10.1016/j.cattod.2006.06.006.

[110] N. M. Kinnunen *et al.*, “Decomposition of Al2O3-supported PdSO4 and Al2(SO4)3 in the regeneration of methane combustion catalyst: A model catalyst study,” *Catalysts*, vol. 9, no. 5, 2019, doi: 10.3390/catal9050427.

[111] S. Ordóñez, P. Hurtado, and F. V. Díez, “Methane catalytic combustion over Pd/Al2O3 in presence of sulphur dioxide: Development of a regeneration procedure,” *Catal. Letters*, vol. 100, no. 1–2, pp. 27–34, 2005, doi: 10.1007/s10562-004-3081-1.

[112] A. Gremminger, P. Lott, M. Merts, M. Casapu, J. D. Grunwaldt, and O. Deutschmann, “Sulfur poisoning and regeneration of bimetallic Pd-Pt methane oxidation catalysts,” *Appl. Catal. B Environ.*, vol. 218, pp. 833–843, 2017, doi: 10.1016/j.apcatb.2017.06.048.

[113] D. . Fullerton *et al.*, “Sulphur poisoning and regeneration of precious metal catalysed methane combustion,” *Catal. Today*, vol. 81, no. 4, pp. 589–601, 2003, doi: 10.1016/s0920-5861(03)00157-3.

[114] Y. Zhang *et al.*, “Sulfur poisoning and regeneration of Rh-ZSM-5 catalysts for total oxidation of methane,” *Appl. Catal. B Environ.*, vol. 277, Nov. 2020, doi:

10.1016/j.apcatb.2020.119176.

[115] J. Y. Luo, D. Kisinger, A. Abedi, and W. S. Epling, “Sulfur release from a model Pt/Al2O3 diesel oxidation catalyst: Temperature-programmed and step-response techniques characterization,” *Appl. Catal. A Gen.*, vol. 383, no. 1–2, pp. 182–191, 2010, doi: 10.1016/j.apcata.2010.05.049.

[116] P. Bazin *et al.*, “On the reducibility of sulfated Pt/CeXZr1-XO2 solids: A coupled thermogravimetric FT-IR study using CO as the reducing agent,” *Appl. Catal. B Environ.*, vol. 119–120, pp. 207–216, May 2012, doi: 10.1016/j.apcatb.2012.02.037.

[117] T. Luo and R. J. Gorte, “Characterization of SO2-poisoned ceria-zirconia mixed oxides,” *Appl. Catal. B Environ.*, vol. 53, no. 2, pp. 77–85, 2004, doi: 10.1016/j.apcatb.2004.04.020.

[118] F. Cabello Galisteo *et al.*, “Reactivation of sulphated Pt/Al2O3 catalysts by reductive treatment in the simultaneous oxidation of CO and C3H6,” *Appl. Catal. B Environ.*, vol. 72, no. 3–4, pp. 272–281, Mar. 2007, doi: 10.1016/j.apcatb.2006.11.004.

[119] P. Bazin *et al.*, “A thermogravimetric and FT-IR study of the reduction by H2 of sulfated Pt/CexZr1-xO2 solids,” *Appl. Catal. B Environ.*, vol. 90, no. 3–4, pp. 368–379, Aug. 2009, doi: 10.1016/j.apcatb.2009.03.016.

[120] V. H. Nissinen, N. M. Kinnunen, and M. Suvanto, “Regeneration of a sulfur-poisoned methane combustion catalyst: Structural evidence of Pd4S formation,” *Appl. Catal. B Environ.*, vol. 237, pp. 110–115, Dec. 2018, doi: 10.1016/j.apcatb.2018.05.057.

[121] N. M. Kinnunen, J. T. Hirvi, K. Kallinen, T. Maunula, M. Keenan, and M. Suvanto, “Case study of a modern lean-burn methane combustion catalyst for automotive applications: What are the deactivation and regeneration mechanisms?,” *Appl. Catal. B Environ.*, vol. 207, pp. 114–119, 2017, doi: 10.1016/j.apcatb.2017.02.018.

[122] P. W. Chen, D. Maiti, R. F. Liu, L. C. Grabow, and M. P. Harold, “CH4 steam reforming on Pt + Pd/Al2O3 monolith: Impact of Mn0.5Fe2.5O4 spinel addition,” *Catal. Sci. Technol.*, pp. 2618–2633, 2022, doi: 10.1039/d2cy00270a.

[123] Z. Zhou, M. P. Harold, and D. Luss, “Dynamic Oxygen Storage Capacity of Ceria-Zirconia and Mn 0.5 Fe 2.5 O 4 Spinel: Experiments and Modeling,” *Ind. Eng. Chem. Res.*, 2021, doi: 10.1021/acs.iecr.0c05187.

[124] P. L. Silveston, “Automotive exhaust catalysis under periodic operation,” *Catal. Today*, vol. 25, no. 2, pp. 175–195, 1995, doi: 10.1016/0920-5861(95)00107-Q.

[125] E. Becker, P. A. Carlsson, H. Grönbeck, and M. Skoglundh, “Methane oxidation over alumina supported platinum investigated by time-resolved in situ XANES spectroscopy,” *J. Catal.*, vol. 252, no. 1, pp. 11–17, 2007, doi: 10.1016/j.jcat.2007.09.004.

[126] E. Becker, P. A. Carlsson, L. Kylhammar, M. A. Newton, and M. Skoglundh, “In situ

spectroscopic investigation of low-temperature oxidation of methane over alumina-supported platinum during periodic operation," *J. Phys. Chem. C*, vol. 115, no. 4, pp. 944–951, 2011, doi: 10.1021/jp103609n.

[127] R. Burch and P. K. Loader, "Investigation of Pt/Al2O3 , and Pd/Al2O3 catalysts for the combustion of methane at low concentrations," *Appl. Catal. B, Environ.*, vol. 5, pp. 149–164, 1994.

[128] A. Hinz, A. Andersson, M. Skoglundh, and E. Fridell, "An investigation of the reaction mechanism for the promotion of propane oxidation over Pt/Al2O3 by SO2," *J. Catal.*, vol. 201, no. 2, pp. 247–257, 2001, doi: 10.1006/jcat.2001.3248.

[129] R. Burch, E. Halpin, M. Hayes, K. Ruth, and J. A. Sullivan, "The nature of activity enhancement for propane oxidation over supported Pt catalysts exposed to sulphur dioxide," *Appl. Catal. B Environ.*, vol. 19, no. 3–4, pp. 199–207, 1998, doi: 10.1016/S0926-3373(98)00079-4.

[130] A. F. Lee *et al.*, "The origin of SO2 promotion of propane oxidation over Pt/Al2O3 catalysts," *J. Catal.*, vol. 184, no. 2, pp. 491–498, 1999, doi: 10.1006/jcat.1999.2454.

[131] D. Bounechada *et al.*, "Mechanisms behind sulfur promoted oxidation of methane," *Phys. Chem. Chem. Phys.*, vol. 15, no. 22, pp. 8648–8661, 2013, doi: 10.1039/c3cp44289f.

[132] A. Melchor, E. Garbowski, M. V Mathieu, and M. Primet, "Sulfur Poisoning of Pt/Al203 Catalysts, I. Determination of Sulfur Coverage by Infrared Spectroscopy," 1985.

[133] S. Hilaire, S. Sharma, R. J. Gorte, J. M. Vohs, and H. W. Jen, "Effect of SO2 on the oxygen storage capacity of ceria-based catalysts," *Catal. Letters*, vol. 70, no. 3–4, pp. 131–135, 2000, doi: 10.1023/A:1018885201072.

[134] O. Saur, M. Bensitel, A. B. M. Saad, J. C. Lavalley, C. P. Tripp, and B. A. Morrow, "The structure and stability of sulfated alumina and titania," *J. Catal.*, vol. 99, no. 1, pp. 104–110, 1986, doi: 10.1016/0021-9517(86)90203-4.

[135] F. Ullmann, W. Gerhartz, Y. S. Yamamoto, F. T. Campbell, R. Pfefferkorn, and J. F. Rounsaville, *Ullmann's Encyclopedia of Industrial Chemistry*. VCH, 1985.

[136] S. C. Davis and R. G. Boundy, "Transportation Energy Data Book (Edition 40)," Oak Ridge National Laboratory, 2022. doi: 10.2172/1878695.

[137] J. L. Sullivan *et al.*, "Policy Analysis CO_2 Emission Benefit of Diesel (versus Gasoline) Powered Vehicles," *Environ. Sci. Technol.*, vol. 38, no. 12, pp. 3217–3223, 2004.

[138] H. Xiong, A. K. Datye, and Y. Wang, "Thermally Stable Single-Atom Heterogeneous Catalysts," *Adv. Mater.*, vol. 33, no. 50, pp. 1–19, 2021, doi: 10.1002/adma.202004319.

[139] H. Zhang, S. Fang, and Y. H. Hu, "Recent advances in single-atom catalysts for

CO oxidation," *Catal. Rev. - Sci. Eng.*, vol. 00, no. 00, pp. 1–42, 2020, doi: 10.1080/01614940.2020.1821443.

[140] P. Kumar, T. A. Al-Attas, J. Hu, and M. G. Kibria, "Single Atom Catalysts for Selective Methane Oxidation to Oxygenates," *ACS Nano*, vol. 16, no. 6, pp. 8557–8618, 2022, doi: 10.1021/acsnano.2c02464.

[141] J. J. H. B. Sattler *et al.*, "Platinum-promoted Ga/Al2O3 as highly active, selective, and stable catalyst for the dehydrogenation of propane," *Angew. Chemie - Int. Ed.*, vol. 53, no. 35, pp. 9251–9256, 2014, doi: 10.1002/anie.201404460.

[142] N. Kong *et al.*, "Single Vanadium Atoms Anchored on Graphitic Carbon Nitride as a High-Performance Catalyst for Non-oxidative Propane Dehydrogenation," *ACS Nano*, vol. 14, no. 5, pp. 5772–5779, 2020, doi: 10.1021/acsnano.0c00659.

[143] Q. Y. Chang *et al.*, "Dual-function catalysis in propane dehydrogenation over Pt1–Ga2O3 catalyst: Insights from a microkinetic analysis," *AIChE J.*, vol. 66, no. 7, pp. 10–12, 2020, doi: 10.1002/aic.16232.

[144] L. Liu, D. M. Meira, R. Arenal, P. Concepcion, A. V. Puga, and A. Corma, "Determination of the Evolution of Heterogeneous Single Metal Atoms and Nanoclusters under Reaction Conditions: Which Are the Working Catalytic Sites?," *ACS Catal.*, vol. 9, no. 12, pp. 10626–10639, 2019, doi: 10.1021/acscatal.9b04214.

[145] S. Feng *et al.*, "Sulfur Poisoning and Self-Recovery of Single-Site Rh1/Porous Organic Polymer Catalysts for Olefin Hydroformylation," *Angew. Chemie - Int. Ed.*, vol. 62, no. 30, 2023, doi: 10.1002/anie.202304282.

[146] M. Kaneeda, H. Iizuka, T. Hiratsuka, N. Shinotsuka, and M. Arai, "Improvement of thermal stability of NO oxidation Pt/Al2O3 catalyst by addition of Pd," *Appl. Catal. B Environ.*, vol. 90, no. 3–4, pp. 564–569, 2009, doi: 10.1016/j.apcatb.2009.04.011.

[147] A. Morlang *et al.*, "Bimetallic Pt/Pd diesel oxidation catalysts: Structural characterisation and catalytic behaviour," *Appl. Catal. B Environ.*, vol. 60, no. 3–4, pp. 191–199, 2005, doi: 10.1016/j.apcatb.2005.03.007.

[148] P. H. Ho, J. W. Woo, R. F. Ilmasani, J. Han, and L. Olsson, "The role of Pd-Pt interactions in the oxidation and sulfur resistance of bimetallic Pd-Pt/γ-Al2O3diesel oxidation catalysts," *Ind. Eng. Chem. Res.*, vol. 60, no. 18, pp. 6596–6612, 2021, doi: 10.1021/acs.iecr.0c05622.

[149] M. J. Hazlett and W. S. Epling, "Spatially resolving CO and C3H6 oxidation reactions in a Pt/Al2O3 model oxidation catalyst," *Catal. Today*, vol. 267, pp. 157–166, 2016, doi: 10.1016/j.cattod.2015.11.033.

[150] M. Al-Harbi, R. Hayes, M. Votsmeier, and W. S. Epling, "Competitive NO, CO and hydrocarbon oxidation reactions over a diesel oxidation catalyst," *Can. J. Chem. Eng.*, vol. 90, no. 6, pp. 1527–1538, 2012, doi: 10.1002/cjce.20659.

[151] S. E. Voltz, C. R. Morgan, D. Liederman, and S. M. Jacob, "Kinetic Study of Carbon Monoxide and Propylene Oxidation on Platinum Catalysts," *Ind. Eng. Chem. Prod. Res. Dev.*, vol. 12, no. 4, pp. 294–301, 1973, doi: 10.1021/i360048a006.

[152] R. Raj, M. P. Harold, and V. Balakotaiah, “Steady-state and dynamic hysteresis effects during lean co-oxidation of CO and C3H6 over Pt/Al2O3 monolithic catalyst,” *Chem. Eng. J.*, vol. 281, pp. 322–333, 2015, doi: 10.1016/j.cej.2015.06.057.

[153] K. Irani, W. S. Epling, and R. Blint, “Spatial resolution of reactant species consumption in diesel oxidation catalysts,” *Top. Catal.*, vol. 52, no. 13–20, pp. 1856–1859, 2009, doi: 10.1007/s11244-009-9349-3.

[154] K. I. Choi and M. A. Vannice, “CO oxidation over Pd and Cu catalysts V. Al2O3-supported bimetallic PdCu particles,” *J. Catal.*, vol. 131, no. 1, pp. 36–50, 1991, doi: 10.1016/0021-9517(91)90321-T.

[155] Y. Li, J. Hu, M. Chen, and H. Wan, “Promotion Effect of Cu for CO Oxidation on Ceria Supported PdxCuy Bimetallic Catalysts,” *J. Phys. Chem. C*, vol. 126, no. 3, pp. 1420–1425, 2022, doi: 10.1021/acs.jpcc.1c10078.

[156] E. S. Bickford, S. Velu, and C. Song, “Nano-structured CeO2 supported Cu-Pd bimetallic catalysts for the oxygen-assisted water-gas-shift reaction,” *Catal. Today*, vol. 99, no. 3–4, pp. 347–357, 2005, doi: 10.1016/j.cattod.2004.10.010.

[157] J. Kugai, J. T. Miller, N. Guo, and C. Song, “Oxygen-enhanced water gas shift on ceria-supported Pd-Cu and Pt-Cu bimetallic catalysts,” *J. Catal.*, vol. 277, no. 1, pp. 46–53, 2011, doi: 10.1016/j.jcat.2010.10.014.

[158] S. Yun and V. Guliants, “Novel Bimetallic Cu-Pd Nanoparticles as Highly Active Low-Temperature WGS Catalysts,” *Ind. Eng. Chem. Res.*, vol. 59, no. 5, pp. 1789–1799, 2020, doi: 10.1021/acs.iecr.9b03978.

[159] L. Guczi, Z. Schay, G. Stefler, L. F. Liotta, G. Deganello, and A. M. Venezia, “Pumice-supported Cu-Pd catalysts: Influence of copper on the activity and selectivity of palladium in the hydrogenation of phenylacetylene and but-1-ene,” *J. Catal.*, vol. 182, no. 2, pp. 456–462, 1999, doi: 10.1006/jcat.1998.2344.

[160] B. K. Furlong, J. W. Hightower, T. Y. L. Chan, A. Sarkany, and L. Guczi, “1,3-Butadiene Selective Hydrogenation Over Pd/Alumina and Cupd/Alumina Catalysts,” *Appl. Catal. A, Gen.*, vol. 117, no. 1, pp. 41–51, 1994, doi: 10.1016/0926-860X(94)80157-6.

[161] T. Bathena, T. Phung, S. R. Svadlenak, Y. Liu, L. C. Grabow, and K. A. Goulas, “Oxygenate Reactions over PdCu and PdAg Catalysts: Distinguishing Electronic and Geometric Effects on Reactivity and Selectivity,” *ACS Catal.*, pp. 5766–5775, 2022, doi: 10.1021/acscatal.2c00561.

[162] Y. Song and L. C. Grabow, “Activity Trends for Catalytic CO and NO Co-Oxidation at Low Temperature Diesel Emission Conditions,” *Ind. Eng. Chem. Res.*, vol. 57, no. 38, pp. 12715–12725, Sep. 2018, doi: 10.1021/acs.iecr.8b01905.

[163] A. Y. Song *et al.*, “PdCu Alloy Catalyst for Inhibition-free, Low-temperature CO Oxidation,” *ChemCatChem*, no. e202301024, 2023, doi: 10.1002/cctc.202301024.

[164] S. Kristy, S. Svadlenak, A. S. Hoffman, S. R. Bare, and A. Goulas, “Spectroscopic determination of metal redox and segregation effects during CO and CO / NO

oxidation over silica-supported Pd and PdCu catalysts," *Appl. Catal. B Environ.*, vol. 342, no. September 2023, p. 123329, 2024, doi: 10.1016/j.apcatb.2023.123329.

[165] D. L. Mowery, M. S. Graboski, T. R. Ohno, and R. L. McCormick, "Deactivation of PdO-Al2O3 oxidation catalyst in lean-burn natural gas engine exhaust: Aged catalyst characterization and studies of poisoning by H2O and SO2," *Appl. Catal. B Environ.*, vol. 21, no. 3, pp. 157–169, 1999, doi: 10.1016/S0926-3373(99)00017-X.

[166] R. Burch and F. J. Urbano, "Investigation of the active state of supported palladium catalysts in the combustion of methane," *Appl. Catal. A, Gen.*, vol. 124, no. 1, pp. 121–138, 1995, doi: 10.1016/0926-860X(94)00252-5.

[167] "Diesel Fuel Standards and Rulemakings," *Us Epa*, 2015. https://www.epa.gov/diesel-fuel-standards/diesel-fuel-standards-and-rulemakings (accessed Oct. 05, 2023).

[168] H. N. Sharma, S. L. Suib, and A. B. Mhadeshwar, *Interactions of sulfur oxides with diesel oxidation catalysts (DOCs)*, vol. 1132. 2013. doi: 10.1021/bk-2013-1132.ch005.

[169] G. Corro, "Sulfur Impact on Diesel Emission Control - A Review," *React. Kinet. Catal. Lett.*, vol. 75, pp. 89–106, 2002.

[170] H. N. Sharma, Y. Sun, and E. A. Glascoe, "Microkinetic modeling of H2SO4 formation on Pt based diesel oxidation catalysts," *Appl. Catal. B Environ.*, vol. 220, pp. 348–355, 2018, doi: 10.1016/j.apcatb.2017.08.025.

[171] J. Ma, S. Chang, F. Yu, H. Lai, and Y. Zhao, "Research Progress on Sulfur Deactivation and Regeneration over Cu-CHA Zeolite Catalyst," *Catalysts*, vol. 12, no. 12, 2022, doi: 10.3390/catal12121499.

[172] H. N. Sharma, V. Sharma, A. B. Mhadeshwar, and R. Ramprasad, "Why Pt survives but Pd suffers from SOx poisoning?," *J. Phys. Chem. Lett.*, vol. 6, no. 7, pp. 1140–1148, Apr. 2015, doi: 10.1021/jz5027147.

[173] P. C. Liao, T. H. Fleisch, and E. Wolf, "Activity and XPS Studies of Sulfur Poisoning Catalysts Effect on Pt-Cu/Al2O3 Oxidation Catalysis," *J. Catal.*, vol. 75, pp. 396–403, 1982.

[174] J. T. Kummer, "Laboratory experiments evaluating the effects of S and Cu on a PtAl2O3 auto exhaust oxidation catalysts," *J. Catal.*, vol. 38, no. 1–3, pp. 166–171, 1975, doi: 10.1016/0021-9517(75)90074-3.

[175] P. S. Hammershøi, P. N. R. Vennestrøm, H. Falsig, A. D. Jensen, and T. V. W. Janssens, "Importance of the Cu oxidation state for the SO2-poisoning of a Cu-SAPO-34 catalyst in the NH3-SCR reaction," *Appl. Catal. B Environ.*, vol. 236, no. February, pp. 377–383, 2018, doi: 10.1016/j.apcatb.2018.05.038.

[176] Y. Jangjou *et al.*, "Nature of Cu Active Centers in Cu-SSZ-13 and Their Responses to SO2 Exposure," *ACS Catal.*, vol. 8, no. 2, pp. 1325–1337, 2018, doi: 10.1021/acscatal.7b03095.

[177] A. Galtayries, J. Grimblot, and J. P. Bonnelle, “Interaction of SO2 with different polycrystalline Cu, Cu2O and CuO surfaces,” *Surf. Interface Anal.*, vol. 24, no. 5, pp. 345–354, 1996, doi: 10.1002/(SICI)1096-9918(199605)24:5<345::AID-SIA126>3.0.CO;2-2.

[178] W. Yang *et al.*, “Interfacial structure-governed SO2 resistance of Cu/TiO2 catalysts in the catalytic oxidation of CO,” *Catal. Sci. Technol.*, vol. 10, no. 6, pp. 1661–1674, 2020, doi: 10.1039/c9cy02405k.

[179] N. Diaz Montenegro and W. S. Epling, “Effects of SO2 poisoning and regeneration on spinel containing CH4 oxidation catalysts,” *Appl. Catal. B Environ.*, vol. 336, no. 5 November 2023, p. 122894, 2023, doi: 10.1016/j.apcatb.2023.122894.

[180] L. Jiao and J. R. Regalbuto, “The synthesis of highly dispersed noble and base metals on silica via strong electrostatic adsorption: I. Amorphous silica,” *J. Catal.*, vol. 260, no. 2, pp. 329–341, 2008, doi: 10.1016/j.jcat.2008.09.022.

[181] P. Zelenka, W. Cartellieri, and P. Herzog, “Worldwide diesel emission standards, current experiences and future needs,” *Appl. Catal. B Environ.*, vol. 10, no. 1–3, pp. 3–28, 1996, doi: 10.1016/0926-3373(96)00021-5.

[182] K. G. Rappé *et al.*, “Aftertreatment Protocols for Catalyst Characterization and Performance Evaluation: Low-Temperature Oxidation, Storage, Three-Way, and NH 3 -SCR Catalyst Test Protocols,” *Emiss. Control Sci. Technol.*, vol. 5, no. 2, pp. 183–214, 2019, doi: 10.1007/s40825-019-00120-7.

[183] A. K. Datye and M. Votsmeier, “Opportunities and challenges in the development of advanced materials for emission control catalysts,” *Nat. Mater.*, vol. 20, no. 8, pp. 1049–1059, 2021, doi: 10.1038/s41563-020-00805-3.

[184] T. W. Hansen, A. T. Delariva, S. R. Challa, and A. K. Datye, “Sintering of catalytic nanoparticles: Particle migration or ostwald ripening?,” *Acc. Chem. Res.*, vol. 46, no. 8, pp. 1720–1730, 2013, doi: 10.1021/ar3002427.

[185] R. Gholami, M. Alyani, and K. Smith, *Deactivation of Pd Catalysts by Water during Low Temperature Methane Oxidation Relevant to Natural Gas Vehicle Converters*, vol. 5, no. 2. 2015. doi: 10.3390/catal5020561.

[186] C. H. Bartholomew, “Mechanism of Catalyst Deactivation,” *Appl. Catal. A Gen.*, vol. 212, pp. 17–60, 2001, doi: 10.1016/S0926-860X(00)00843-7.

[187] S. B. Kang *et al.*, “Ostwald-ripening sintering kinetics of Pd-based three-way catalyst: Importance of initial particle size of Pd,” *Chem. Eng. J.*, vol. 316, pp. 631–644, 2017, doi: 10.1016/j.cej.2017.01.136.

[188] E. D. Goodman *et al.*, “Catalyst deactivation via decomposition into single atoms and the role of metal loading,” *Nat. Catal.*, vol. 2, no. 9, pp. 748–755, Sep. 2019, doi: 10.1038/s41929-019-0328-1.

[189] L. Liu, D. N. Zakharov, R. Arenal, P. Concepcion, E. A. Stach, and A. Corma, “Evolution and stabilization of subnanometric metal species in confined space by in situ TEM,” *Nat. Commun.*, vol. 9, no. 1, pp. 1–10, 2018, doi: 10.1038/s41467-018-

03012-6.

[190] L. S. Escandón, D. Niño, E. Díaz, S. Ordóñez, and F. V. Díez, “Effect of hydrothermal ageing on the performance of Ce-promoted PdO/ZrO2 for methane combustion,” *Catal. Commun.*, vol. 9, no. 13, pp. 2291–2296, 2008, doi: 10.1016/j.catcom.2008.05.026.

[191] A. M. Banerjee *et al.*, “A comprehensive study on Pt/Al2O3 granular catalyst used for sulfuric acid decomposition step in sulfur-iodine thermochemical cycle: Changes in catalyst structure, morphology and metal-support interaction,” *Appl. Catal. B Environ.*, vol. 162, pp. 327–337, 2015, doi: 10.1016/j.apcatb.2014.07.008.

[192] P. Bazin, O. Saur, J. C. Lavalley, G. Blanchard, V. Visciglio, and O. Touret, “Influence of platinum on ceria sulfation,” *Appl. Catal. B Environ.*, vol. 13, no. 3–4, pp. 265–274, 1997, doi: 10.1016/S0926-3373(97)00004-0.

[193] Z. Lu, C. Müller, Z. Yang, K. Hermansson, and J. Kullgren, “SOx on ceria from adsorbed SO2,” *J. Chem. Phys.*, vol. 134, no. 18, 2011, doi: 10.1063/1.3566998.

[194] J. J. Willis *et al.*, “Systematic Structure-Property Relationship Studies in Palladium-Catalyzed Methane Complete Combustion,” *ACS Catal.*, vol. 7, no. 11, pp. 7810–7821, 2017, doi: 10.1021/acscatal.7b02414.

[195] L. Wu *et al.*, “Tuning Precursor Reactivity toward Nanometer-Size Control in Palladium Nanoparticles Studied by in Situ Small Angle X-ray Scattering,” *Chem. Mater.*, vol. 30, no. 3, pp. 1127–1135, 2018, doi: 10.1021/acs.chemmater.7b05186.

[196] M. Cargnello, C. Chen, B. T. Diroll, V. V. T. Doan-Nguyen, R. J. Gorte, and C. B. Murray, “Efficient removal of organic ligands from supported nanocrystals by fast thermal annealing enables catalytic studies on well-defined active phases,” *J. Am. Chem. Soc.*, vol. 137, no. 21, pp. 6906–6911, Jun. 2015, doi: 10.1021/jacs.5b03333.

[197] J. Bergerld, B. Kasemo, and D. . Chakarov, “CO oxidation on Pt(111) promoted by coadsorbed H2O,” *Surf. Sci.*, no. 495, pp. 815–820, 2001.

[198] X. Q. Gong, P. Hu, and R. Raval, “The catalytic role of water in CO oxidation,” *J. Chem. Phys.*, vol. 119, no. 12, pp. 6324–6334, 2003, doi: 10.1063/1.1602053.

[199] R. Caporali *et al.*, “Critical role of water in the direct oxidation of CO and hydrocarbons in diesel exhaust after treatment catalysis,” *Appl. Catal. B Environ.*, vol. 147, pp. 764–769, 2014, doi: 10.1016/j.apcatb.2013.10.004.

[200] D. R. Rainer, M. Koranne, S. M. Vesecky, and D. W. Goodman, “CO + O2 and CO + NO reactions over Pd/Al2O3 catalysts,” *J. Phys. Chem. B*, vol. 101, no. 50, pp. 10769–10774, 1997, doi: 10.1021/jp971262z.

[201] S. Marino, “Characterization and Kinetic Studies of Palladium and Rhodium Catalysts in the Three Way Catakyst System,” University of Virginia, 2023.

7. Appendix A – Supporting Information for Chapter 2

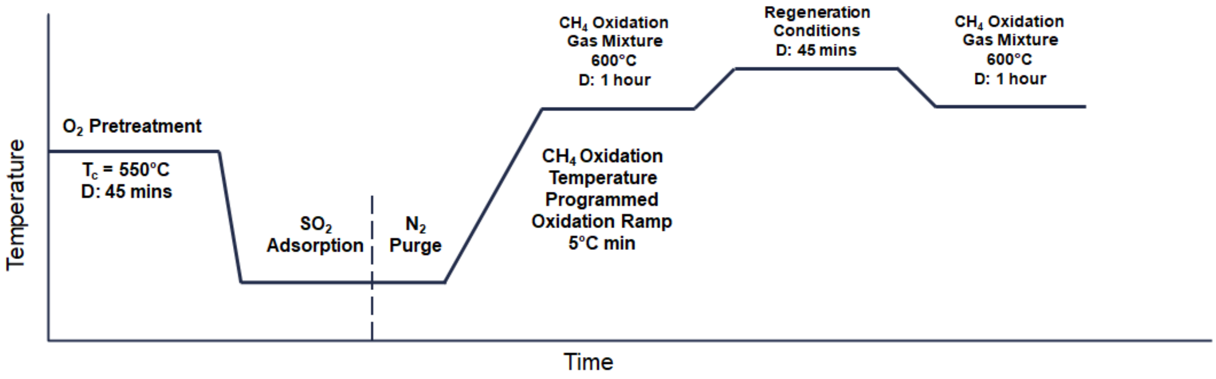

Schematic 8-1 – Regeneration protocol for CH_4 oxidation recovery on PGM + Spinel monolith samples

Table 7-1 Catalyst Composition

Monolith Catalyst	PGM Loading (g/ft^3)	Spinel Loading (g/ft^3)
PGM Only	30 (19:1 Pd:Pt)	0
PGM + spinel	30 (19:1 Pd:Pt)	2832 (25% spinel/75wt% Al_2O_3)

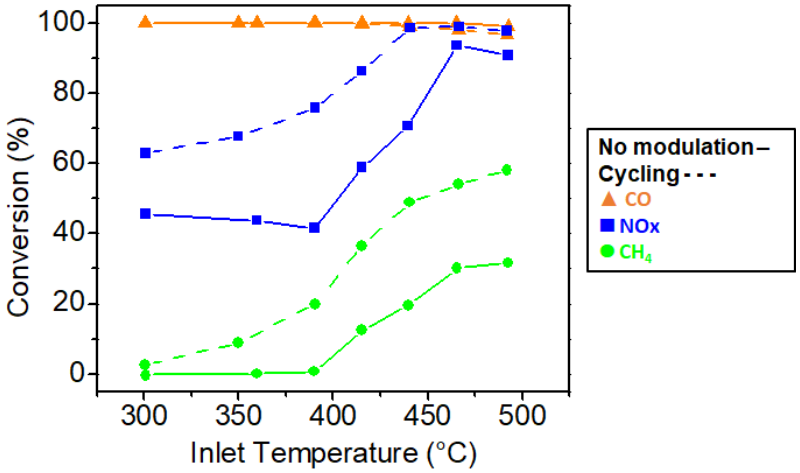

Figure 7-1 CH_4, NO_x, and CO conversion over the PGM + spinel sample under simulated exhaust feed with no modulation (solid lines) and periodic modulation (dashed lines) as a function of temperature.

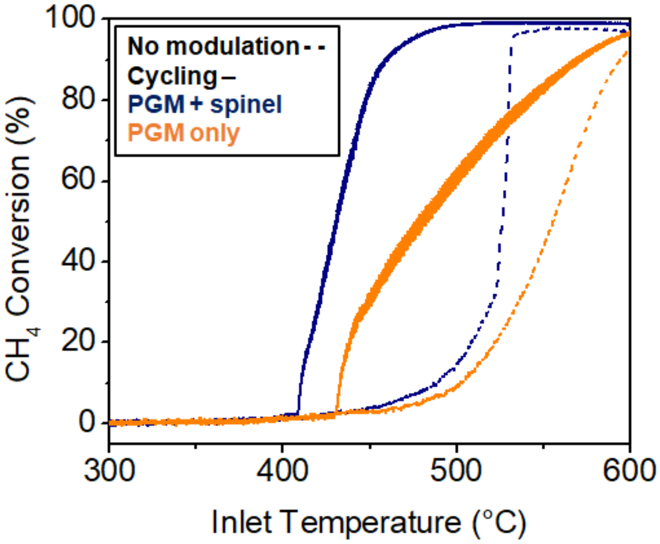

Figure 7-2 CH_4 conversion under no modulation (dashed lines) and with periodic conditions (solid lines) during CH_4 temperature programmed reaction on PGM + spinel and PGM only catalysts.

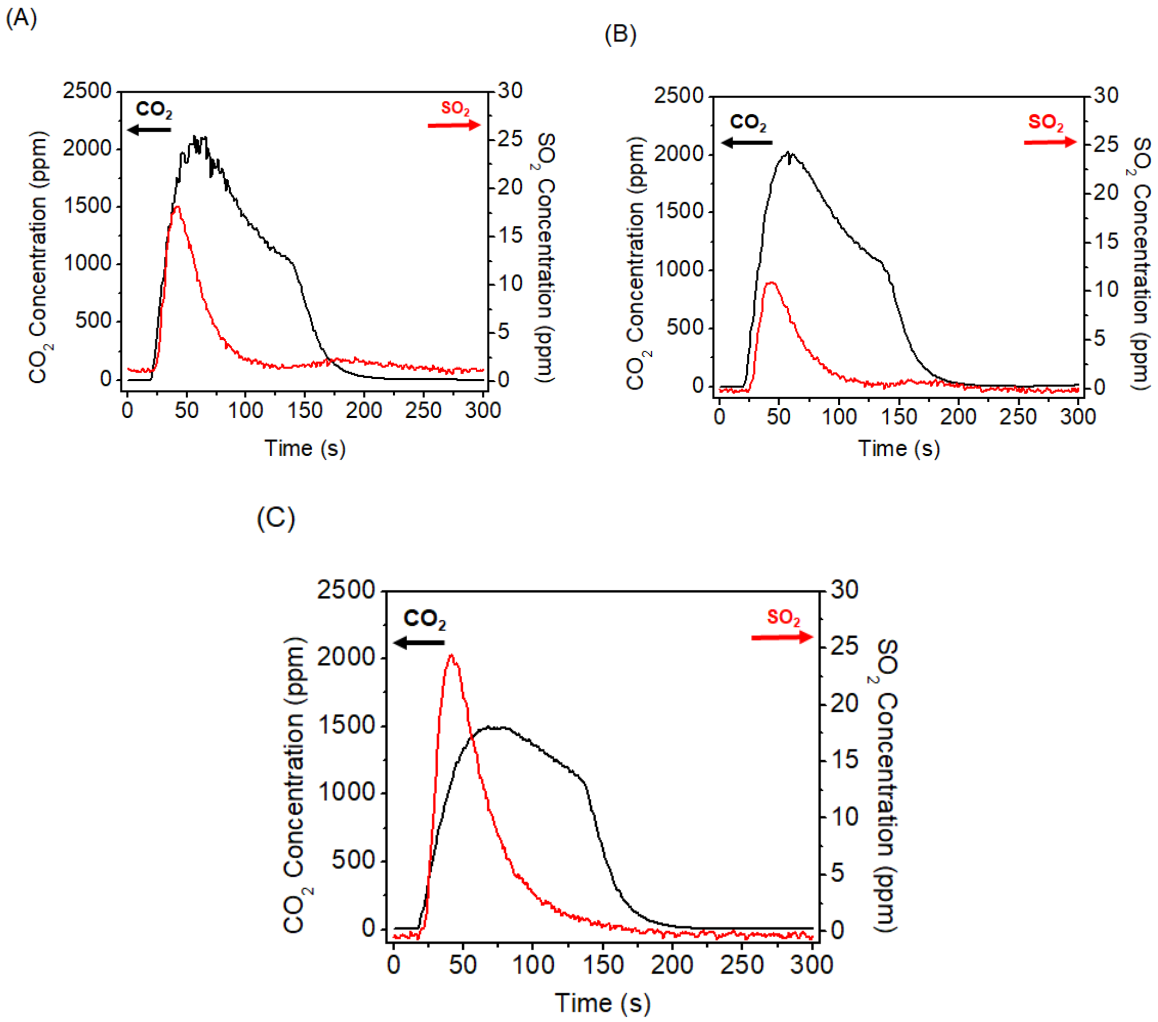

Figure 7-3 CO_2 and SO_2 concentration profiles during the CO pulse at 600 °C with the Mn-Fe spinel material after (A) CO regeneration (0.8% CO in N_2), (B) H_2 regeneration (3% H_2 in N_2), and (C) O_2 regeneration (10% O_2 in N_2) at 600 °C.

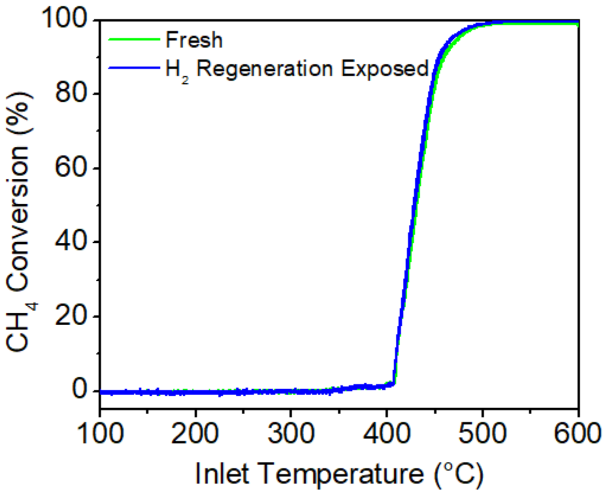

Figure 7-4 CH_4 conversion of fresh (green) and H_2-regenerated (blue) PGM + spinel monolith sample.

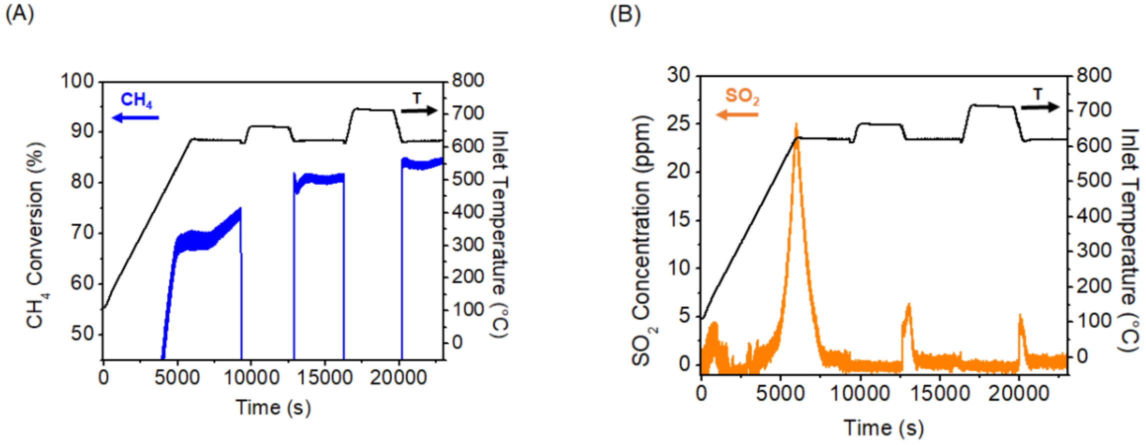

Figure 7-5 (A) CH_4 conversion and (B) SO_2 profile during O_2 regeneration (10% O_2 in N_2) steps at 650 and 700 °C on PGM + spinel monolith sample. After SO_2 exposure at 100 °C, the CH_4 oxidation recovery was assessed using Schematic 8-1.

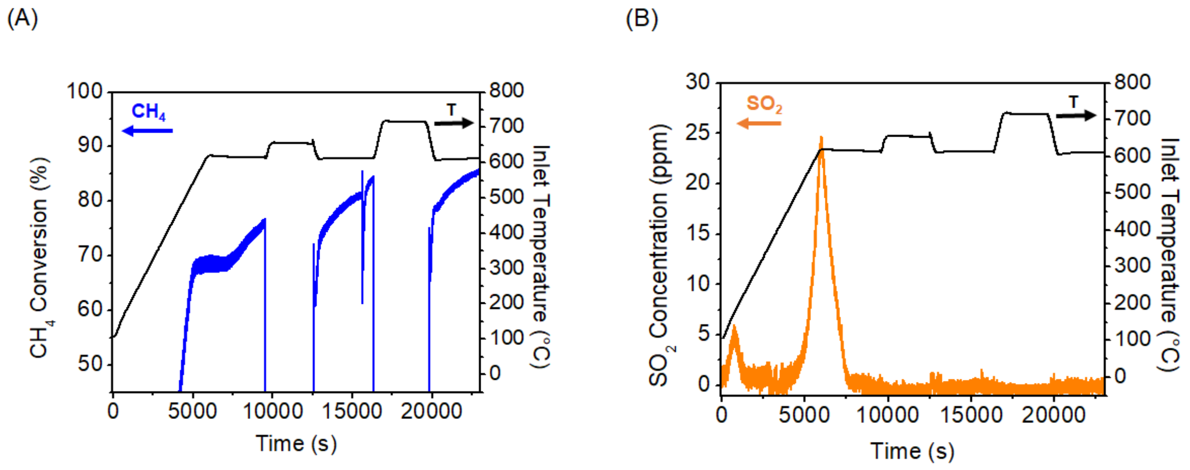

Figure 7-6 (A) CH$_4$ conversion and (B) SO$_2$ profile during H$_2$ regeneration (3% H$_2$ in N$_2$) steps at 650 and 700 °C on PGM + spinel monolith sample. After SO$_2$ exposure at 100 °C, the CH$_4$ oxidation recovery was assessed using Schematic 8-1.

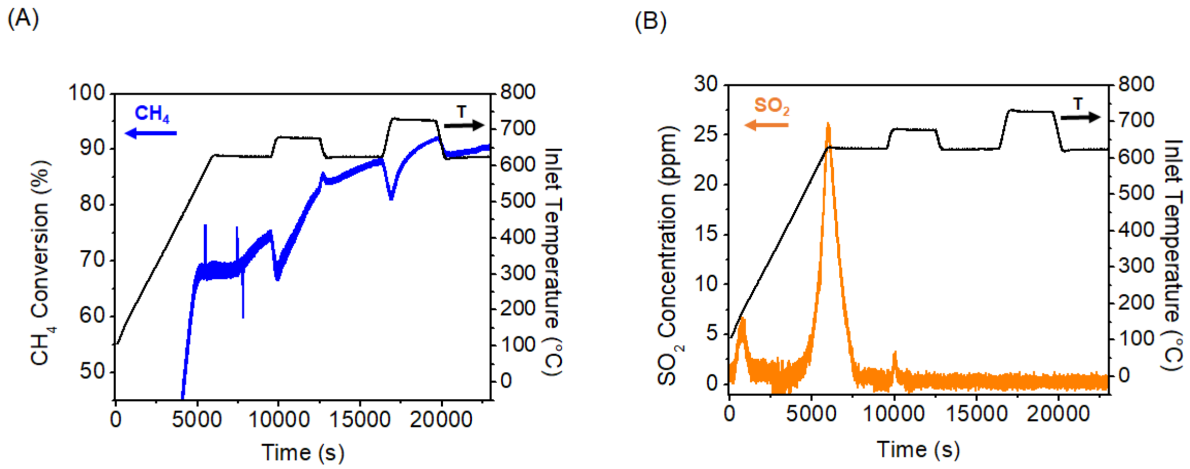

Figure 7-7 (A) CH$_4$ conversion and (B) SO$_2$ profile during CH$_4$ + cycling O$_2$ between 0 and 5500 ppm at 0.25 Hz at 650 and 700 °C on PGM + spinel monolith sample. After SO$_2$ exposure at 100 °C, the CH$_4$ oxidation recovery was assessed using Schematic S1.

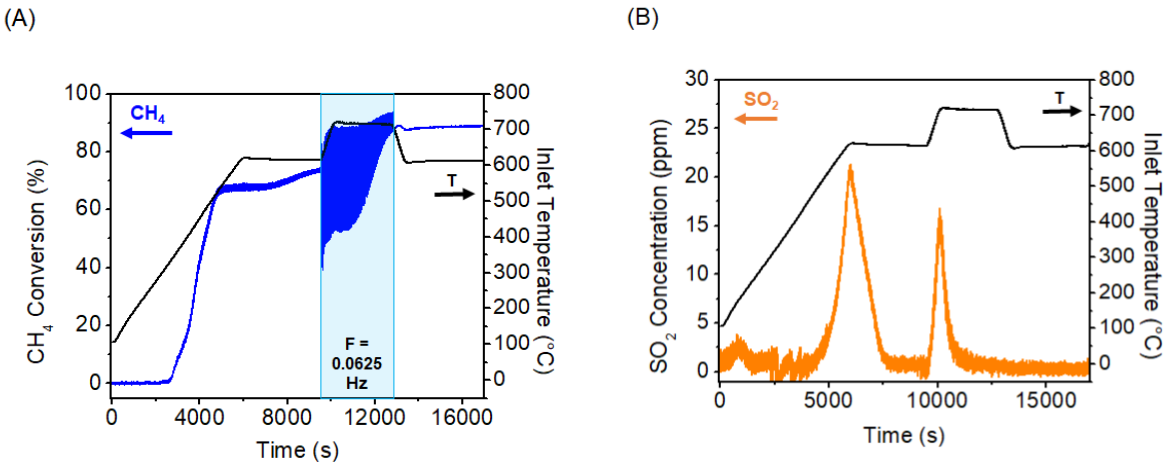

Figure 7-8 (A) CH_4 conversion and (B) SO_2 profile after CH_4 + cycling O_2 between 0 and 5500 ppm at 0.0625 Hz regeneration at 700 °C on PGM + spinel monolith sample. After SO_2 exposure at 100 °C, the CH_4 oxidation recovery was assessed using Schematic S1.

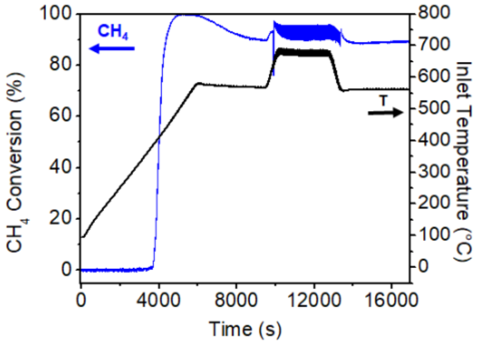

Figure 7-9 CH_4 conversion after CH_4 + [O_2] – 0/5500 ppm + frequency = 0.0625 Hz regeneration steps at 700 °C without sulfur exposure on PGM + spinel monolith sample.

8. Appendix B – Supporting Information for Chapter 3

Table 8-1 Feed (bottle) reagent composition, subsequent reactor composition, and reduction conditions during catalyst activity tests (TPOs).

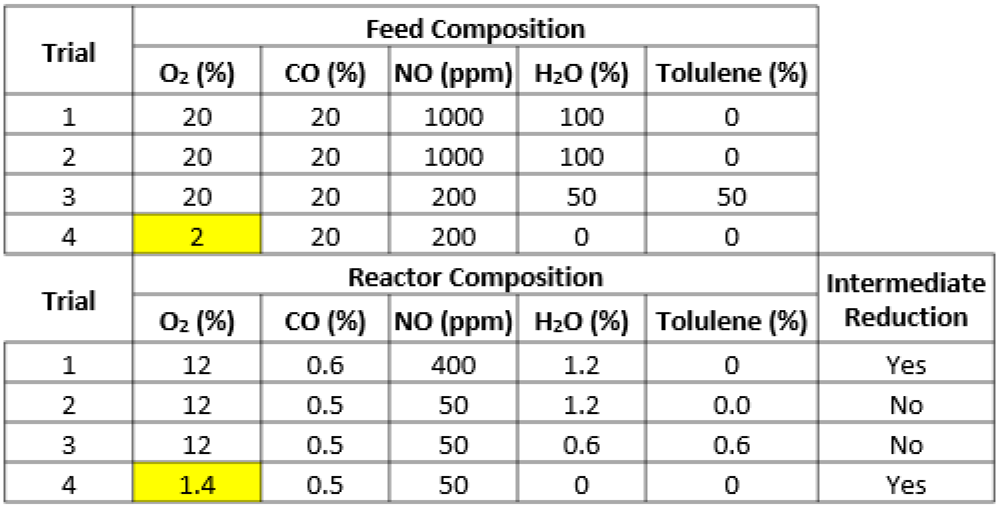

Trial	Feed Composition					
	O_2 (%)	CO (%)	NO (ppm)	H_2O (%)	Toluene (%)	
1	20	20	1000	100	0	
2	20	20	1000	100	0	
3	20	20	200	50	50	
4	2	20	200	0	0	
Trial	**Reactor Composition**					**Intermediate Reduction**
	O_2 (%)	CO (%)	NO (ppm)	H_2O (%)	Toluene (%)	
1	12	0.6	400	1.2	0	Yes
2	12	0.5	50	1.2	0.0	No
3	12	0.5	50	0.6	0.6	No
4	1.4	0.5	50	0	0	Yes

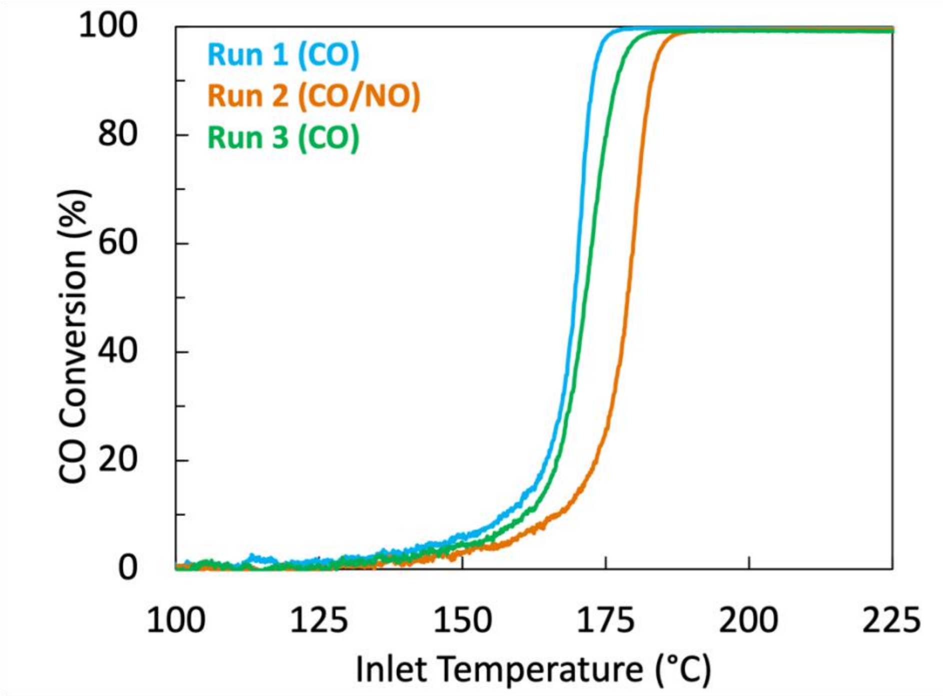

Figure 8-1 CO conversion using 3:1PdCu/SiO_2 Runs 1 and 3 are under CO oxidation baseline conditions, 0.5% CO and 10% O_2 in N_2, while Run 2 includes 200 ppm NO with the CO oxidation baseline conditions.

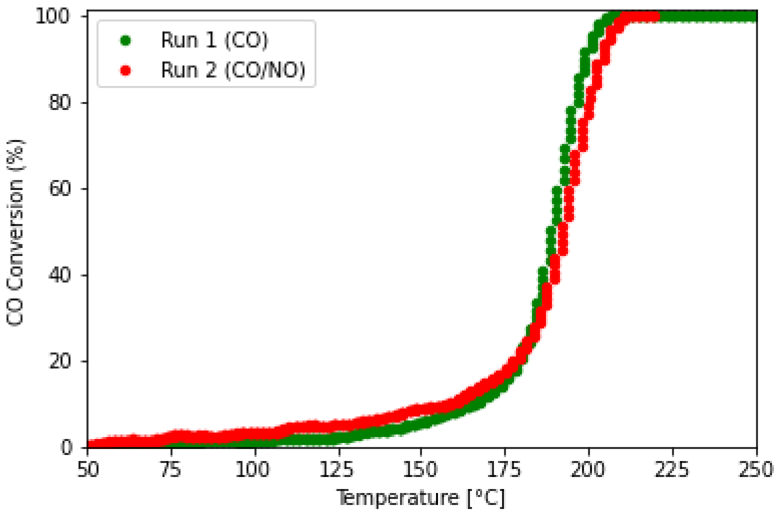

Figure 8-2 3:1 PdCu/SiO_2 light off curves under Trial 4 conditions. Run 1 (green) contains only CO and O_2. Run 2 (red) contains NO.

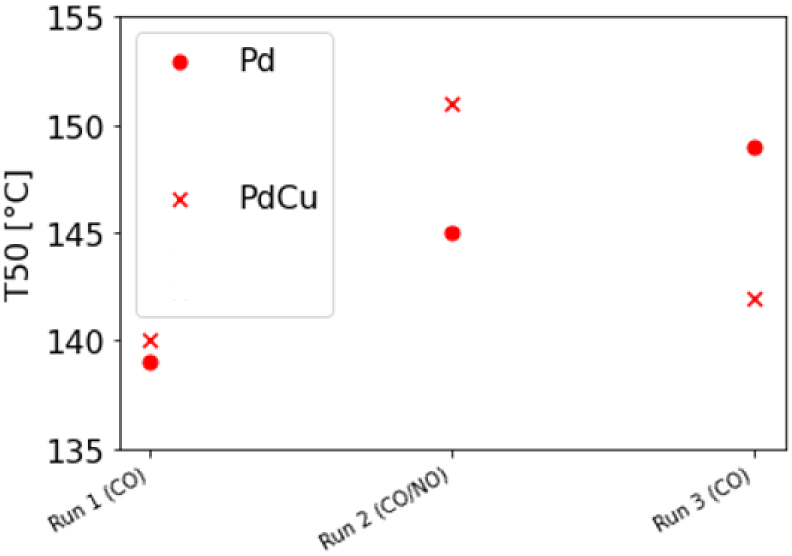

Figure 8-3 Temperature at 50% conversion acquired for Pd/SiO_2 (●) and 3:1 PdCu/SiO_2 (x) under Trial 1 conditions. Run 1 (green) and 3 (blue) contain only CO and O_2. Run 2 (red) contains NO.

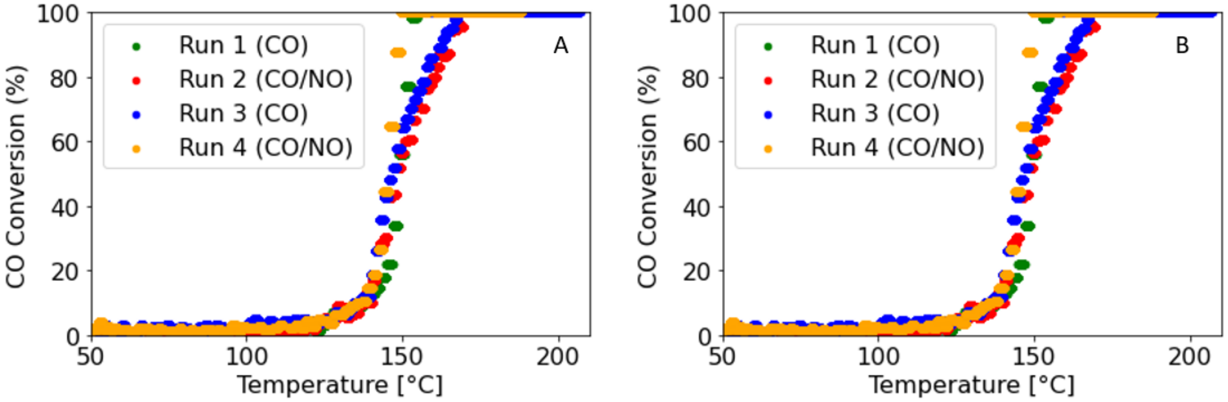

Figure 8-4 Conversion versus temperature for Pd/SiO$_2$ (A) and 3:1 PdCu/SiO$_2$ (B) under Trial 2 conditions. Run 1 (green) and 3 (blue) contain only CO and O$_2$. Run 2 (red) contains NO.

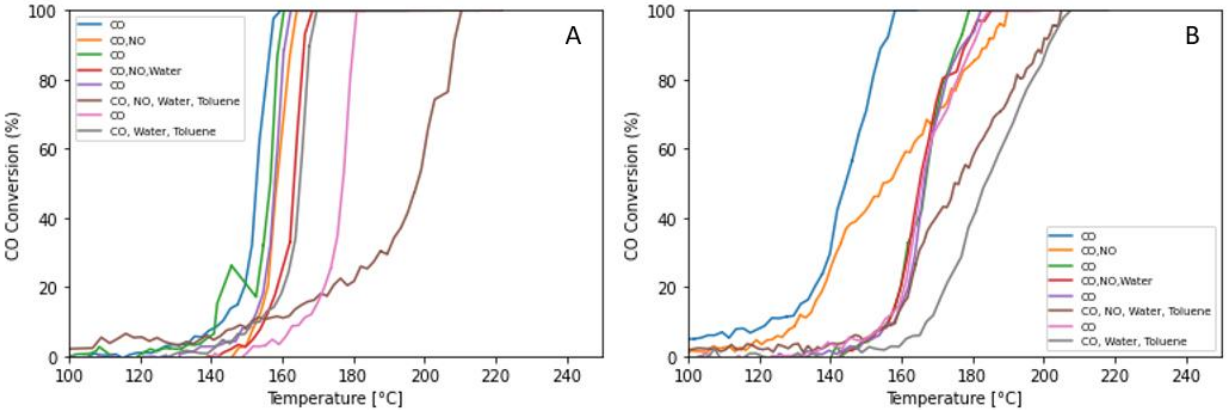

Figure 8-5 Conversion versus temperature for Pd/SiO$_2$ (A) and 3:1 PdCu/SiO$_2$ (B) under Trial 3 conditions. Run 1 (green) and 3 (blue) contain only CO and O$_2$. Run 2 (red) contains NO.

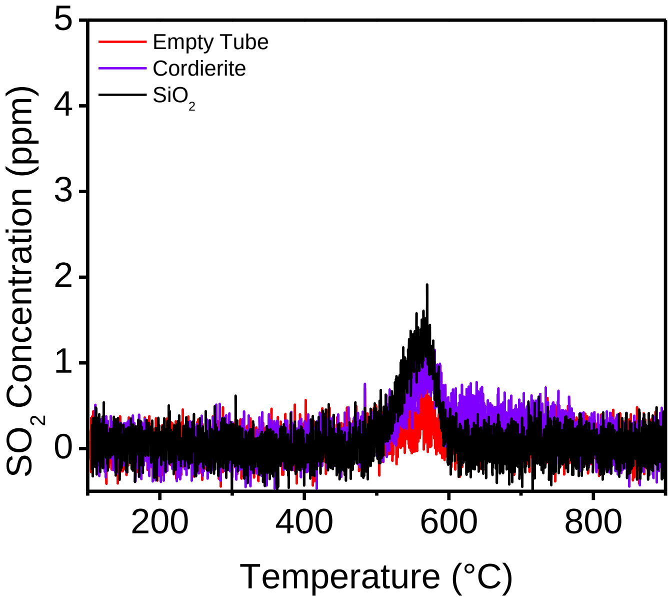

Figure 8-6 SO_2 desorption profiles during temperature program desorption study under N_2 flow for control experiments: empty tube (red), cordierite (purple) and SiO_2 (black).

Table 8-2 Sulfur mass balance for control experiments after SO_2 adsorption at 100 °C

Catalyst	**SO_2 Adsorbed (µmol)**	**SO_2 Desorbed (µmol)**	**% Desorbed**
Empty Tube	0.1	0.1	100
Cordierite	0.1	0.2	> 100
SiO_2 Support	0.1	0.2	> 100

9. Appendix C – Additional Work for Slashing PGM in Catalytic Converters: An Atoms-to-Autos Approach Project

Catalyst Information and Aging Conditions

All fresh and lean-rich aged powder and monolith catalysts were provided by General Motors and the University of Central Florida. Lean-rich aging was performed following aging guidelines found in Ref [182] and using a cycle period of 10 minutes. Unless stated otherwise, the aging temperature of the protocol was performed at 950 °C.

Three-way Catalyst Performance

To assess the TWC performance of the newly synthesized samples, we performed light-off experiments following the Low-Temperature Three-Way Catalyst Test Protocol [182]. All experiments used a total flow rate of 500 sccm and gas hourly space velocity of 200 L/g·hr. Powder catalysts were pretreated at 600°C for 20 minutes in the simulated exhaust shown in Table 9-1. Catalysts were then cooled in N_2 to 100°C. A simulated exhaust gas mixture at λ=0.995 was introduced at 100°C and a temperature ramp to 550°C was performed at 5°C/min.

Table 9-1 Concentrations of the simulated gas mixture, with a $\lambda = 0.995$

[C_3H_6]	**[C_3H_8]**	**[CO]**	**[H_2]**	**[NO]**	**[O_2]**	**[CO_2]**	**[H_2O]**
666 ppm	333 ppm	5000 ppm	1700 ppm	1000 ppm	6400 ppm	13%	13%

0.8 wt% Pd/Al_2O_3

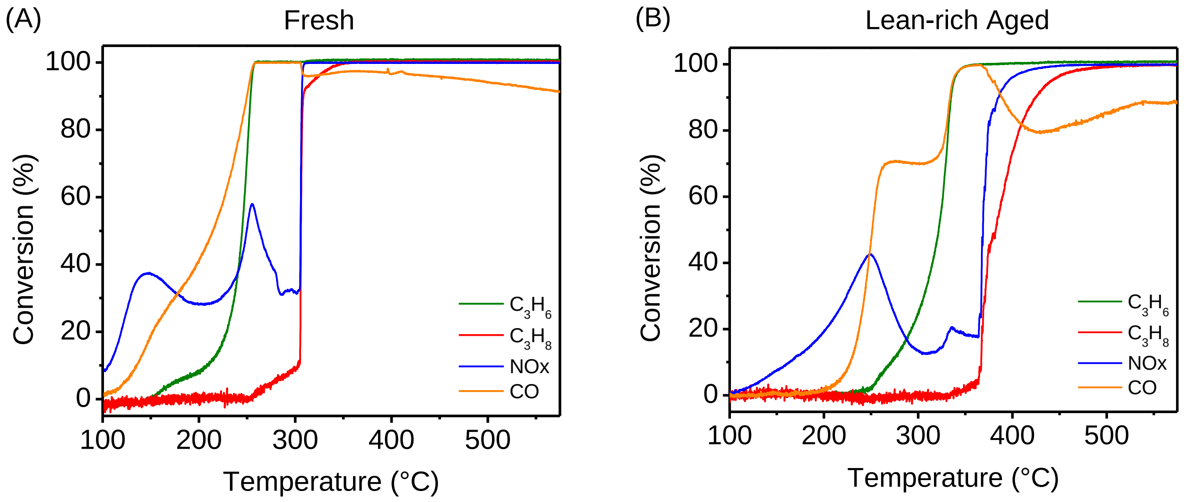

0.8 wt% Pd/20%$Ce_{0.9}Pr_{0.1}$/10%CeO_2/Al_2O_3

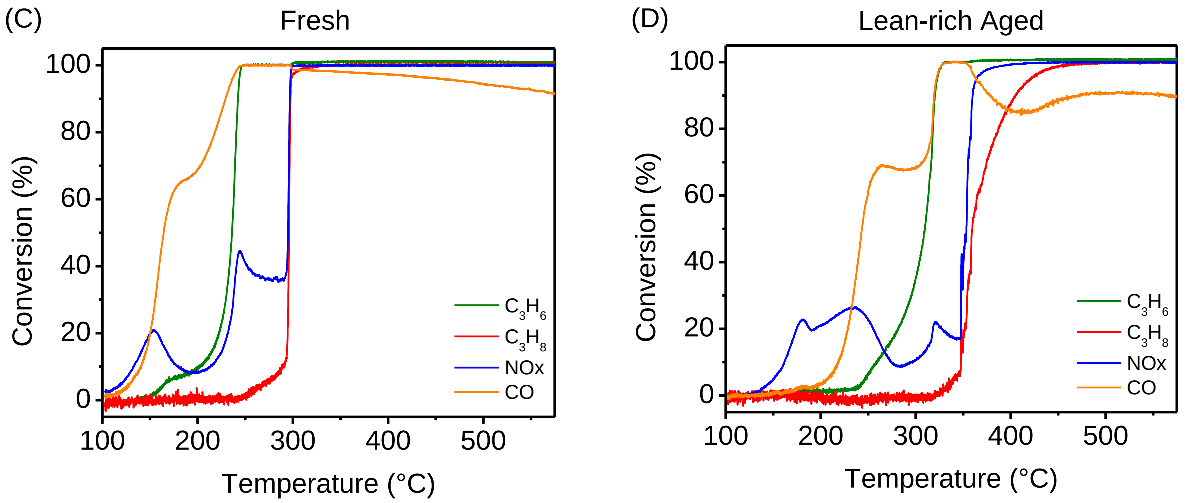

0.8 wt% Pd/20%$Ce_{0.5}Zr_{0.5}$/10%CeO_2/Al_2O_3

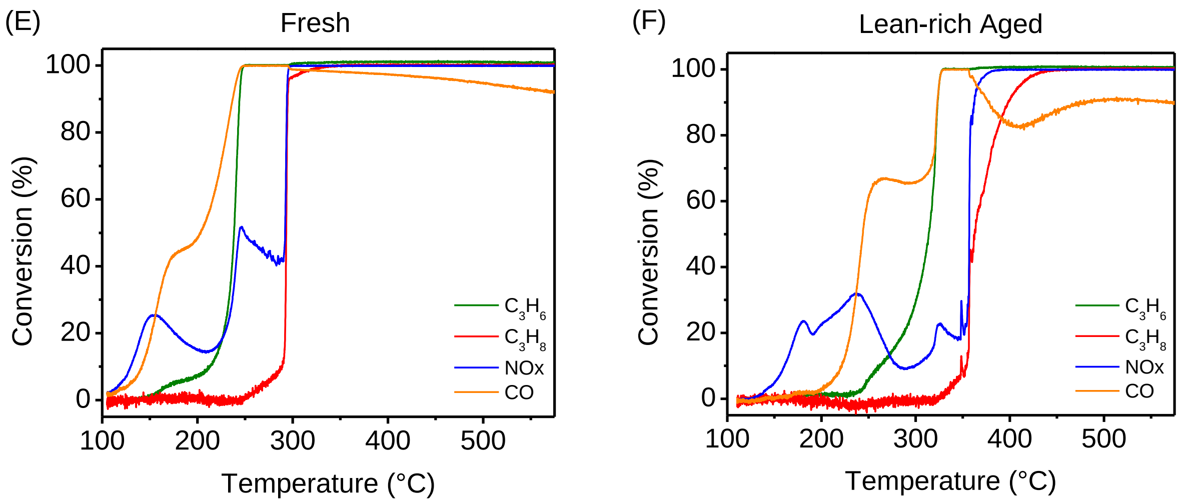

Figure 9-1 CO, NO_x, C_3H_6 and C_3H_8 conversion profiles over fresh and lean/rich aged (A)-(B) 0.8 wt% Pd/Al_2O_3, (C)-(D) 0.8 wt% Pd/20%$Ce_{0.9}Pr_{0.1}$/10%CeO_2/Al_2O_3, and (E)-(F) 0.8 wt% Pd/20%$Ce_{0.5}Zr_{0.5}$/10%CeO_2/Al_2O_3.

Table 9-2 Temperatures at 50% and 90% conversion on the samples tested.

	Conversion	Pd Degreened	Pd Aged	0.8 Pd/Al_2O_3 Fresh	0.8 Pd/Al_2O_3 Lean-Rich Aged	0.8 Pd/20%$Ce_{0.9}Pr_{0.1}$/10%CeO_2/Al_2O_3 Fresh	0.8 Pd/20%$Ce_{0.9}Pr_{0.1}$/10%CeO_2/Al_2O_3 Lean-Rich Aged	0.8 Pd/20%$Ce_{0.5}Zr_{0.5}$/10%CeO_2/Al_2O_3 Fresh	0.8 Pd/20%$Ce_{0.5}Zr_{0.5}$/ 10%CeO_2/ Al_2O_3 Lean-Rich Aged
CO	50	161	231	214	251	164	243	203	244
	90	223	319	250	334	229	319	237	323
NOx	50	229	368	306	369	295	353	292	357
	90	328	378	307	385	297	360	294	362
C_3H_6	50	225	307	245	382	236	310	238	314
	90	238	318	254	425	242	320	244	323
C_3H_8	50	327	369	306	322	296	360	293	363
	90	331	381	308	335	297	405	295	398

X-ray diffraction

Powder X-ray diffraction (XRD) was performed to assess the crystallinity of the fresh and lean-rich aged 0.8wt% Pd/Al_2O_3 and 0.8wt% Pd/20%$Ce_{0.9}Pr_{0.1}$/10%CeO_2/Al_2O_3 samples. XRD patterns were obtained on a PANalytical Empyrean X-ray Diffractometer using Cu Kα radiation and scanned between 2θ values of 15° and 80° under ambient conditions.

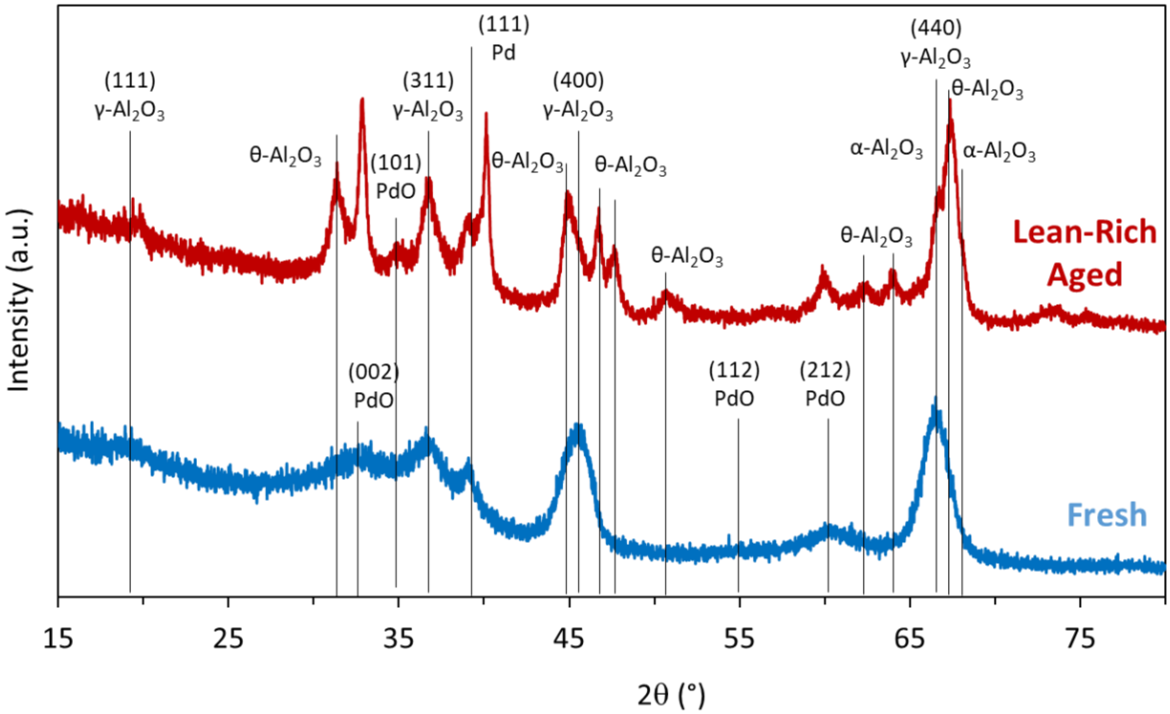

Figure 9-2– XRD profiles of fresh and lean/rich aged 0.8wt% Pd/Al_2O_3.

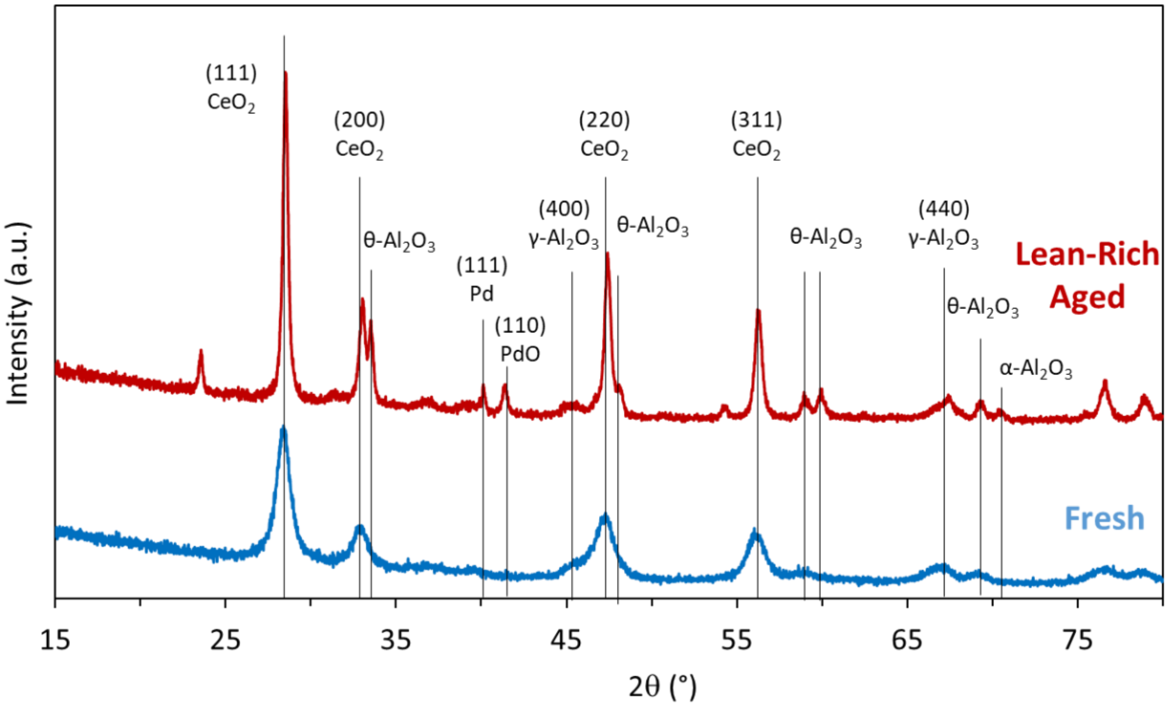

Figure 9-3– XRD profiles of fresh and lean-rich aged 0.8wt% Pd/20%$Ce_{0.9}Pr_{0.1}$/10%CeO_2/Al_2O_3.

Catalytic Activity Evaluation

To assess the effect of Pd loading of the lean-rich aged 0.2wt%, 0.8wt%, and 1.2wt% Pd/20%$Ce_{0.9}Pr_{0.1}$/10%CeO_2/Al_2O_3 samples on TWC performance, we conducted steady-state experiments using gas compositions in accordance with the Low-Temperature Three-Way Catalyst Test Protocol [182]. Reaction rates were calculated by varying the space velocity and catalyst weight (0.2wt% - 333 sccm and 100 mg, 0.8wt% - 600 sccm and 150 mg, 1.2wt% - 600 sccm and 100 mg), and conversions were kept below 15% such that rates were collected in the kinetic regime. Reaction rates were normalized by the nominal amount of Pd in the catalyst. For all experiments, powder catalysts were pretreated at 600°C for 20 minutes in the simulated exhaust described in Table 9-1.

Catalysts were then cooled in N_2, then the simulated exhaust gas mixture was introduced above 100 °C. Kinetic measurements for CO and C_3H_6 oxidation were taken by increasing the temperature stepwise from 200°C to 325°C.

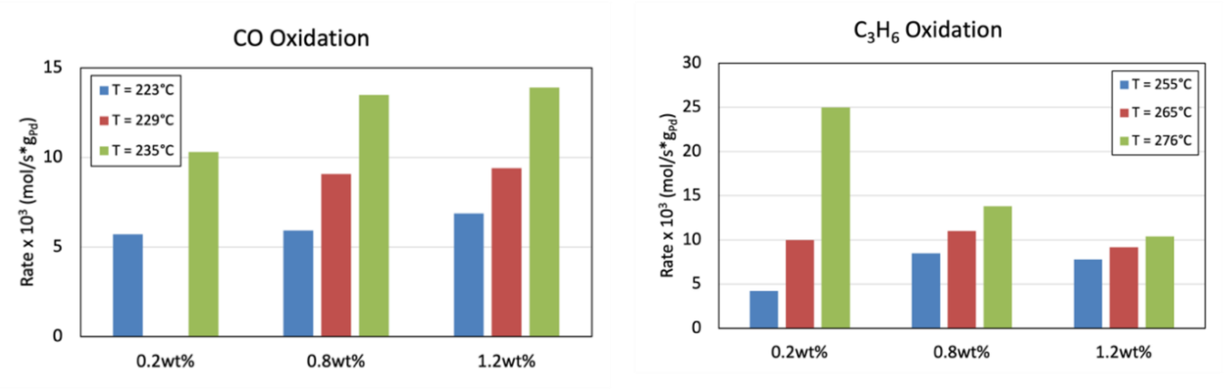

Figure 9-4 (A) CO oxidation rates and (B) C_3H_6 oxidation rates for lean-rich aged 0.2 wt%, 0.8 wt%, and 1.2 wt% Pd/20%$Ce_{0.9}Pr_{0.1}$/10%CeO_2/Al_2O_3 samples under simulated exhaust conditions.

Core Sample Catalytic Activity Evaluation

Powder TWC formulations were tested above, we have also tested monolith core samples. Reference core samples (2wt% Pd/Al_2O_3) were also synthesized to compare the TWC performance with the performance of the new TWC core samples. For the new samples, two supports (Al_2O_3 and CeO_2-modified Al_2O_3) were used. To assess the TWC performance of these newly synthesized and lean-rich aged core samples, we performed light-off experiments following the Low-Temperature Three-Way Catalyst Test Protocol [182]. For all experiments, a total flow rate of 1 L/min and gas hourly space velocity of 60,000 hr^{-1} were used. Monolith core catalysts (catalyst loading 28 g/ft^3) were pretreated at 600°C for 20 minutes in the simulated exhaust shown in Table 9-1. Catalysts were then cooled in N_2 to 100°C. The simulated exhaust gas mixture was introduced at 100°C and a temperature ramp to 550°C was performed at 5°C/min.

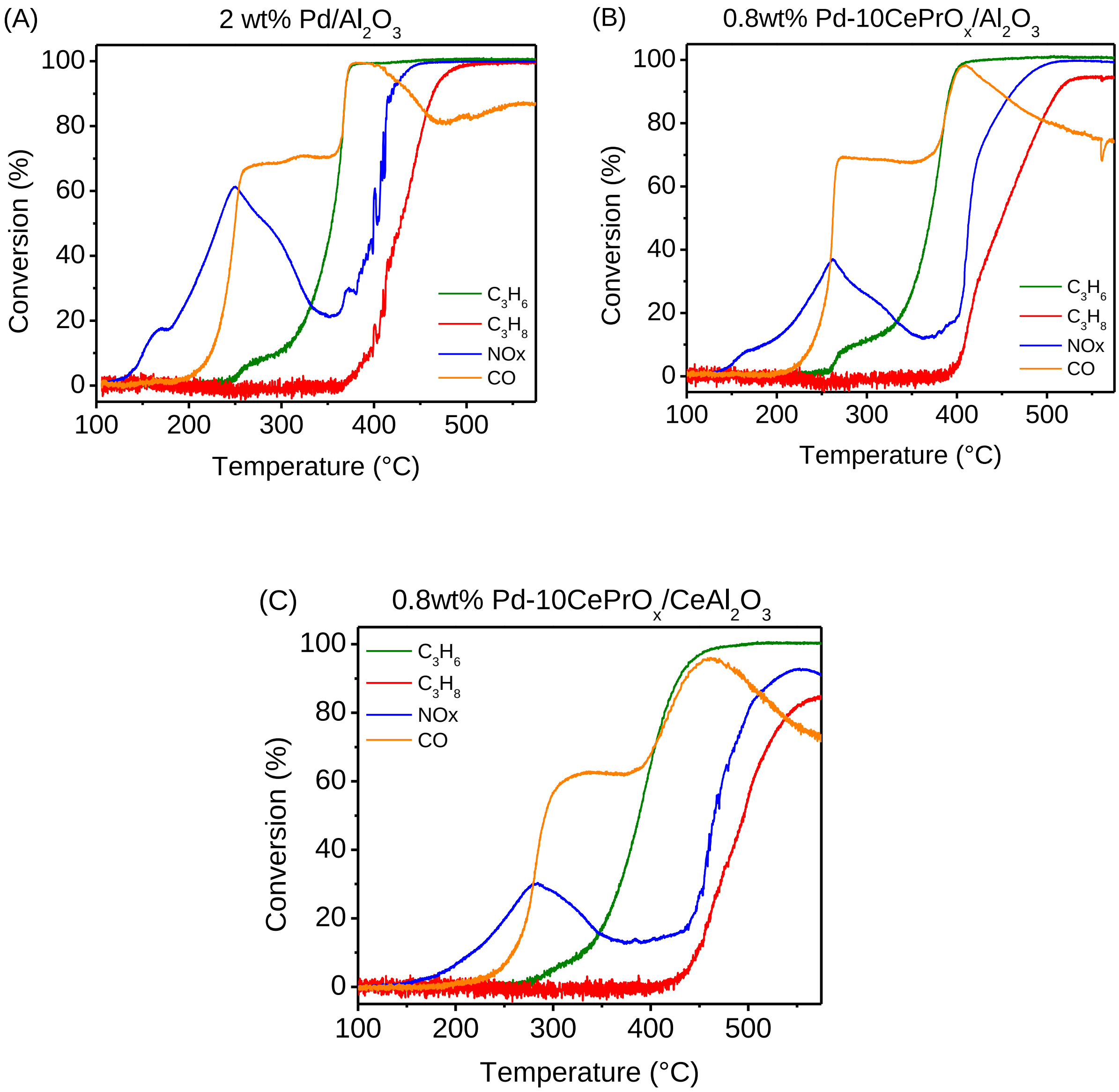

Figure 9-5 TWC performance of lean rich aged (A) 2wt%Pd/Al_2O_3, (B) 0.8wt%Pd-10CePrOx/Al_2O_3, and (C) 0.8wt%Pd-10CePrOx/CeAl_2O_3 core samples.

Table 9-3 Summary of temperature at 50% and 90% conversions on the core samples tested.

	Conversion	2wt% Pd/Al_2O_3 Lean Rich Aged	0.8wt%Pd/CePr/ Al_2O_3 Lean Rich Aged	0.8wt%Pd/CePr/ $CeAl_2O_3$ Lean Rich Aged
CO	50	250	262	292
	90	369	393	436
NOx	50	399	414	465
	90	419	462	530
C_3H_6	50	354	370	287
	90	369	391	388
C_3H_8	50	429	450	429
	90	464	512	-

X-ray Diffraction

Powder X-ray diffraction (XRD) was performed to assess the crystallinity of the fresh, 750 and 950°C lean-rich aged 0.8wt% Pd/ $Ce_{0.9}Pr_{0.1}/Ce_2O_3$-Al_2O_3 samples. XRD patterns were obtained on a PANalytical Empyrean X-ray Diffractometer using Cu $K\alpha$ radiation and scanned between 2θ values of 15° and 80° under ambient conditions. Crystalline size was calculated using Scherrer Equation.

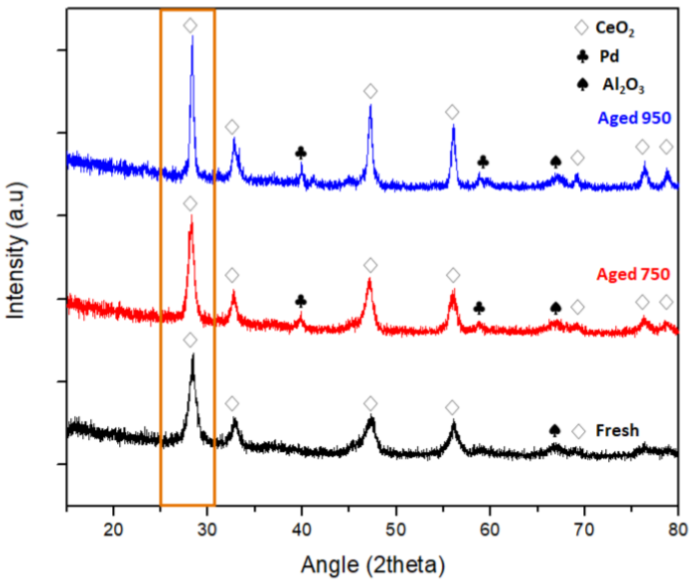

Catalyst	CeO_2(111) Crystalline Size (nm)
Fresh	**70**
Aged 750	**97**
Aged 950	**163**

Figure 9-6 XRD patterns of the fresh, 750 and 950 °C lean-rich aged 0.8%Pd/$Ce_{0.9}Pr_{0.1}/Ce_2O_3$-Al_2O_3 samples (left), and the crystalline size of the CeO_2 using the CeO_2(111) peak (right).

Kinetic Experiments

Steady-state CO and C_3H_6 oxidation in the presence of water were performed to calculate the activation energies for these simpler conditions. The reactions were performed on 0.8%Pd/$Ce_{0.9}Pr_{0.1}$/Ce_2O_3-Al_2O_3 fresh, 750 and 950°C lean-rich aged catalysts, to study the particle size effect. The amount of catalyst used and flowrate were varied to compare the catalysts' activities around the same temperature range. The catalyst was diluted with cordierite to avoid heat transfer limitations. The Pd samples and the diluent were pelletized and sieved to obtain 40-60 mesh (0.42-0.25 mm). Prior to the steady-state experiments, the catalysts were pretreated in 5% H_2 at 500°C for 30 minutes. CO oxidation was performed using 5000 ppm CO, 2500 ppm O_2 and 6% H_2O, while the C_3H_6 oxidation reaction mixture contained 750 ppm C_3H_6, 3375 ppm O_2 and 6% H_2O. To study the reaction within the kinetic regime, only conversions below 20% were considered. The turnover frequencies (TOF) for CO and C_3H_6 oxidation were calculated by normalizing the reaction rates by the surface Pd moles calculated via total chemisorption obtained after saturating the catalysts with CO_2 [201].

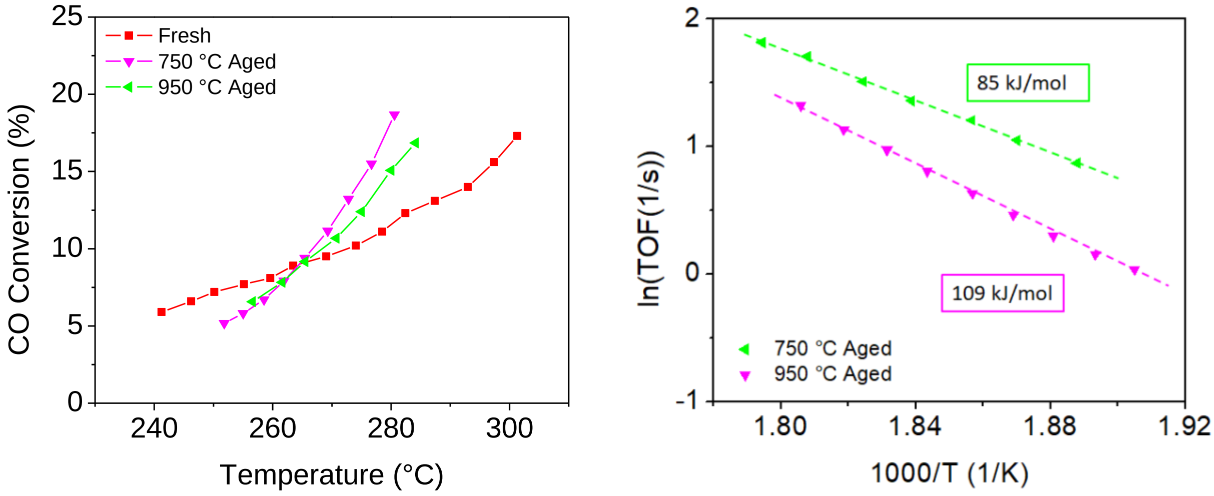

Figure 9-7 CO oxidation conversion (left) and Arrhenius plots (right) on fresh, 750 and 950°C lean-rich aged 0.8%Pd/$Ce_{0.9}Pr_{0.1}/Ce_2O_3$-Al_2O_3. CO = 5000 ppm, O_2 = 2500 ppm, H_2O = 6%.

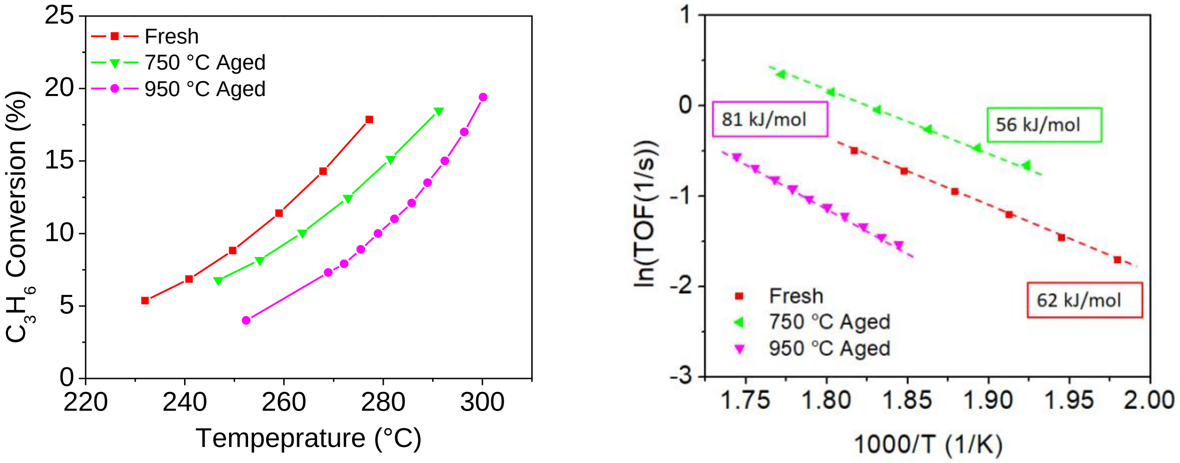

Figure 9-8 C_3H_6 oxidation conversion (left) and Arrhenius plots (right) on fresh, 750 and 950°C lean-rich aged 0.8%Pd/$Ce_{0.9}Pr_{0.1}/Ce_2O_3$-Al_2O_3. C_3H_6 = 750 ppm, O_2 = 3375 ppm, H_2O = 6%.

Kinetic Experiments

Steady-state experiments were performed on the pelletized 0.8Pd-20Ce/10CA-T-Aged and 0.8Pd-20CePr/10CA-T-Aged aged catalysts to calculate the activation energies and reaction orders. The amount of catalyst used was 50 mg. The catalyst was diluted with 150 mg of cordierite to avoid heat transfer limitations. Prior to steady-state experiments, the catalysts were pretreated in 5% H_2 at 600°C for 45 min. Table 9-4 shows the gas conditions for each reaction tested.

Table 9-4 Reaction conditions for kinetic experiments

Reaction	Gas Conditions
C_3H_6 Oxidation	1000 ppm C_3H_6 + 0.45% O_2 + 10% H_2O
C_3H_8 Steam Reforming	1000 ppm C_3H_8 + 10% H_2O
C_3H_8 + NO + O_2 Reaction	1000 ppm C_3H_8 + 1000 ppm NO + 0.42% O_2 + 10% H_2O
CO + NO Reaction	1000 ppm CO + 1000 ppm NO + 10% H_2O

Propene Oxidation

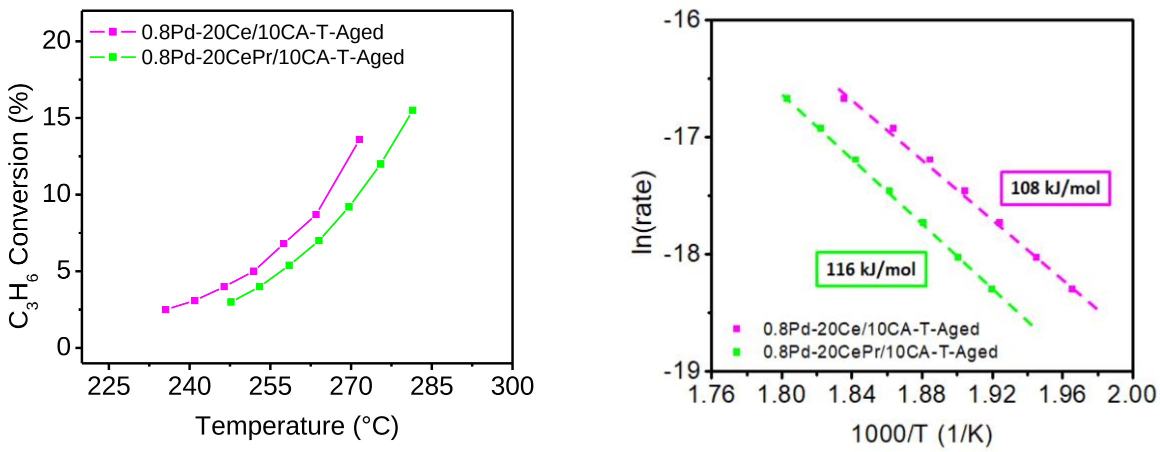

Figure 9-9 Conversion profile (left) and Arrhenius plot (right) for C_3H_6 oxidation over 0.8Pd-20Ce/10CA-T-Aged and 0.8Pd-20CePr/10CA-T-Aged catalysts.

Propane Steam Reforming

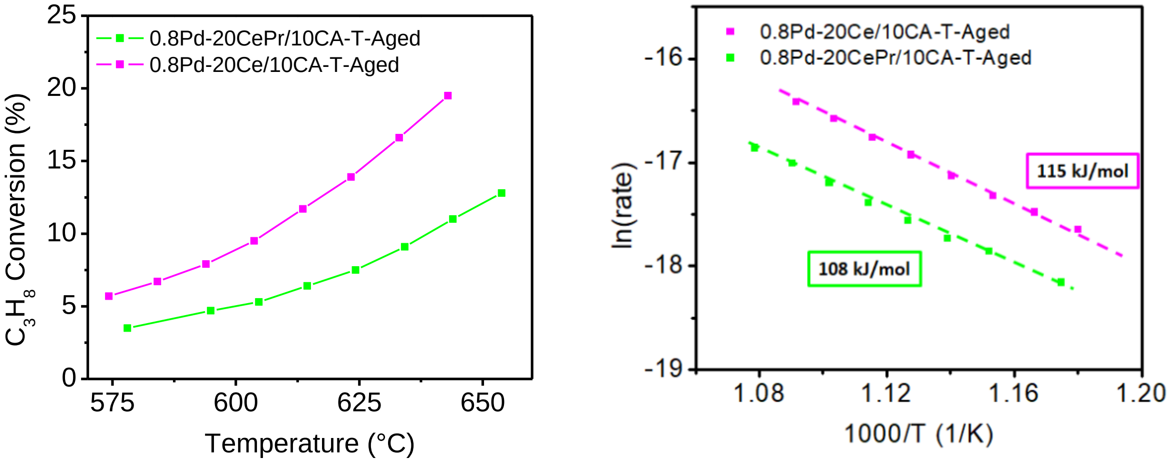

Figure 9-10 Conversion profile (left) and Arrhenius plot (right) for C_3H_8 steam reforming over 0.8Pd-20Ce/10CA-T-Aged and 0.8Pd-20CePr/10CA-T-Aged catalysts.

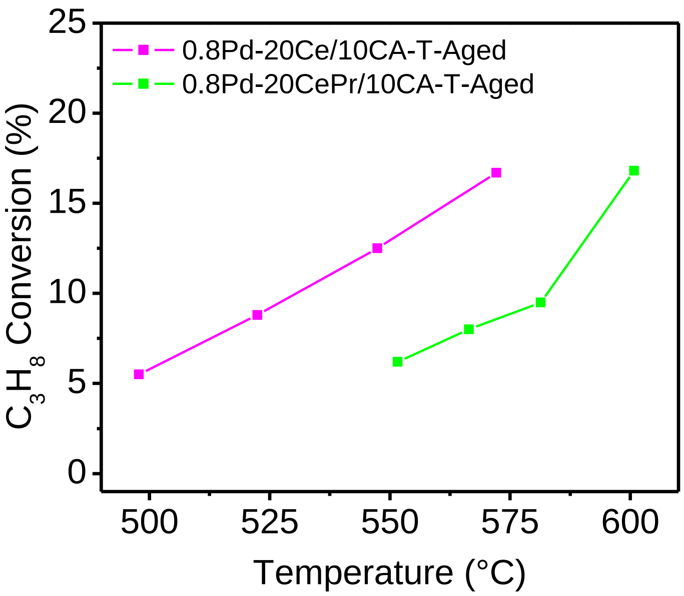

Figure 9-11 Conversion profile for C_3H_8 steam reforming over 0.8Pd-20Ce/10CA-T-Aged and 0.8Pd-20CePr/10CA-T-Aged catalysts. Samples were pretreated in reaction conditions (1000 ppm C_3H_8 + 10% H_2O) at 600 °C for 20 minutes.

C_3H_8 + NO + O_2 Reaction

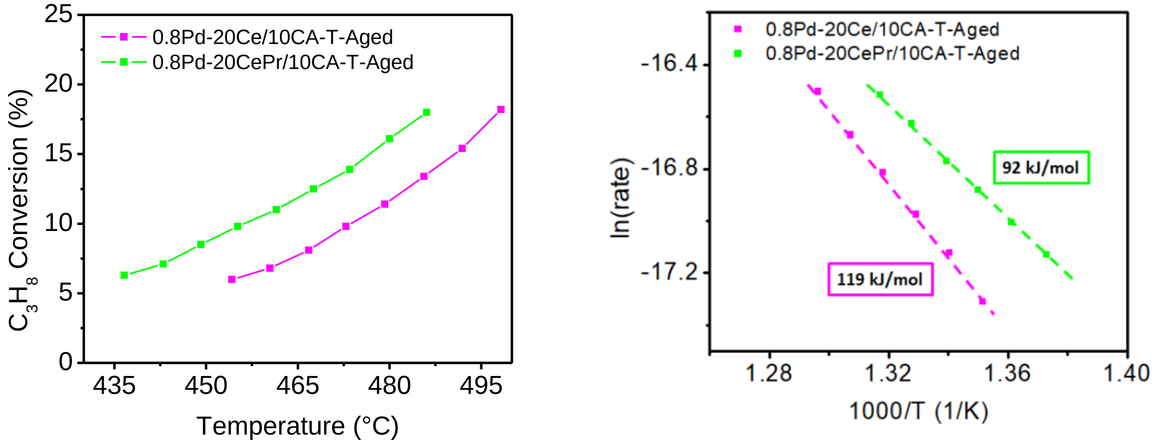

Figure 9-12 Conversion profile (left) and Arrhenius plot (right) for C_3H_8 + NO + O_2 reaction over 0.8Pd-20Ce/10CA-T-Aged and 0.8Pd-20CePr/10CA-T-Aged catalysts.

0.8Pd-20CePr Aged **0.8Pd-20Ce Aged**

C_3H_8

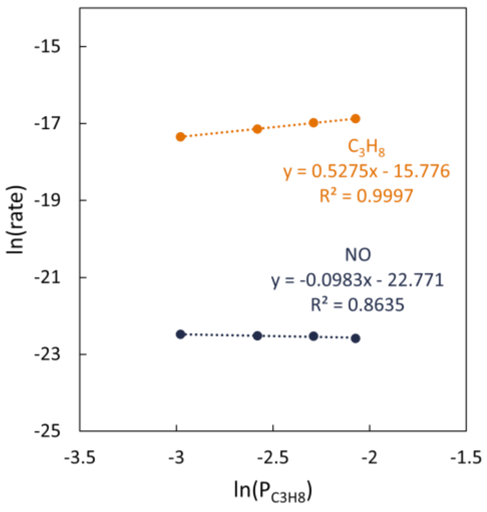

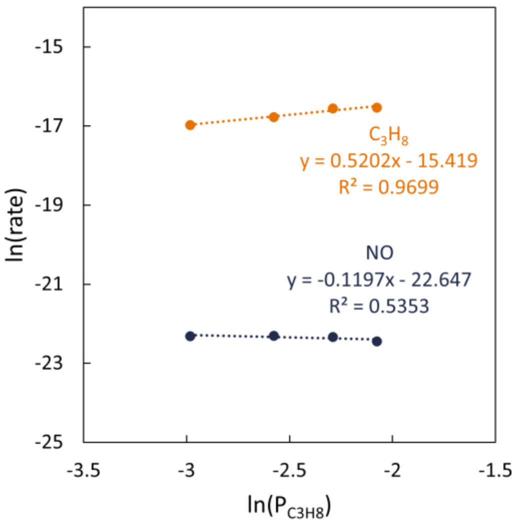

NO

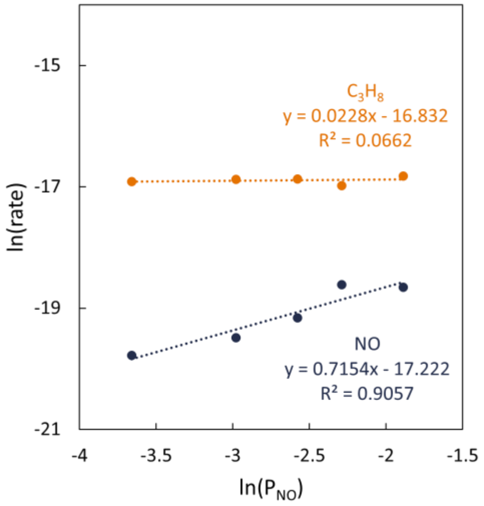

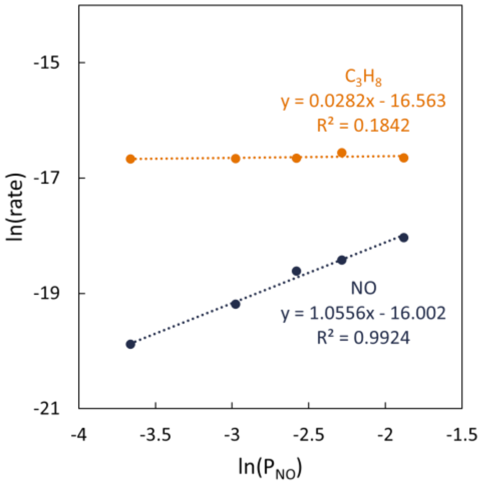

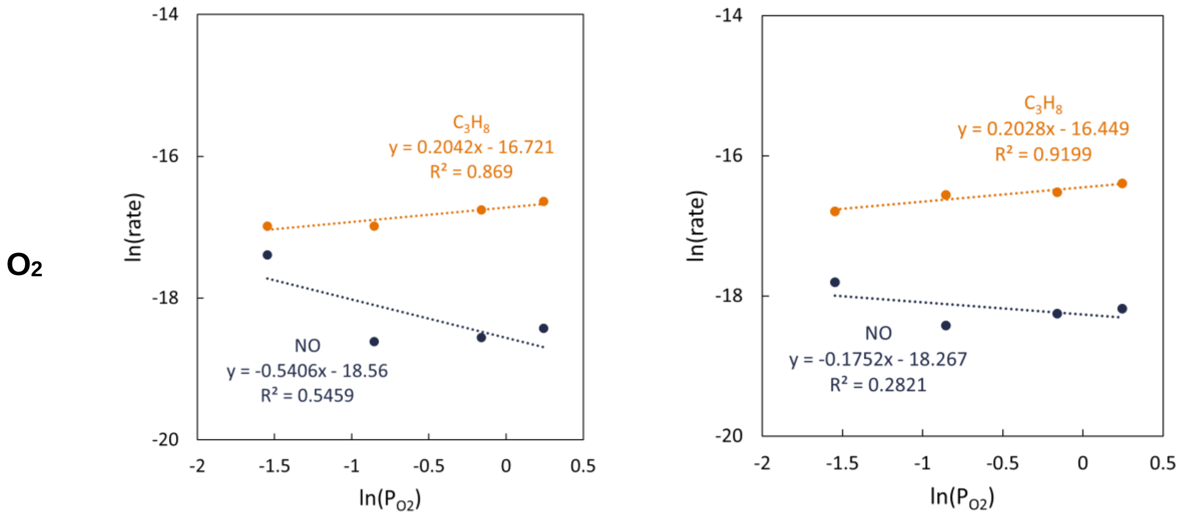

Figure 9-13 C_3H_8, NO and O_2 reaction orders for the C_3H_8 + NO + O_2 reaction over 0.8Pd-20Ce/10CA-T-Aged and 0.8Pd-20CePr/10CA-T-Aged catalysts. Samples were pretreated in 5% H_2 in N_2 at 600 °C for 45 minutes. Reaction conditions: T = 455 °C, [C_3H_8] = 500-1000ppm; [NO] = 250-1000 ppm; [O_2] = 2100-12600 ppm; [H_2O] = 10%.

NO + CO Reaction

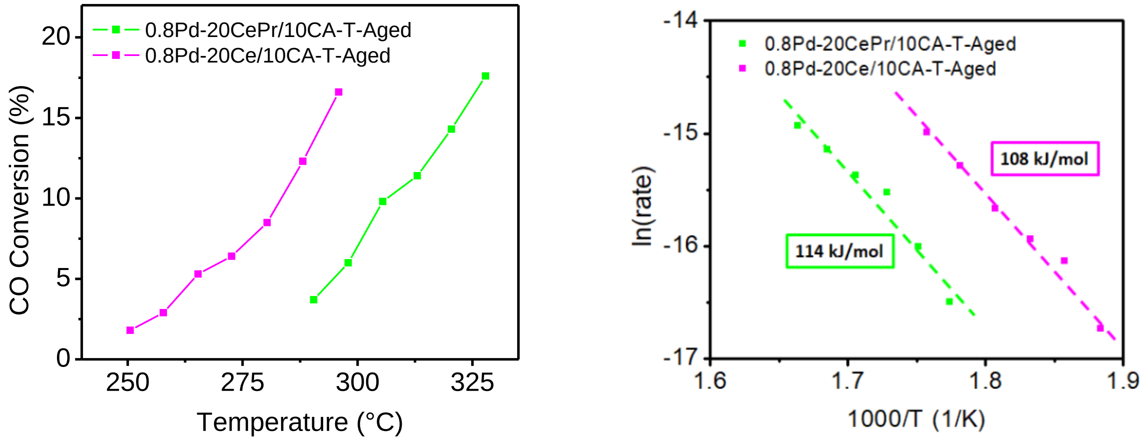

Figure 9-14 Conversion profile (left) and Arrhenius plot (right) for NO + CO reaction over 0.8Pd-20Ce/10CA-T-Aged and 0.8Pd-20CePr/10CA-T-Aged catalysts.